PEEC METHOD FOR EVALUATING MAGNETIC SHIELDING BY METAL STRUCTURES AT LOW FREQUENCY

XIA NENGHONG

Ph.D

The Hong Kong Polytechnic University

2013

The Hong Kong Polytechnic University

Department of Building Services Engineering

PEEC Method for Evaluating Magnetic Shielding by Metal Structures at Low Frequency

XIA NENGHONG

A thesis submitted in partial fulfillment of the requirements

for the degree of Doctor of Philosophy

July, 2013

Certificate of Originality

I hereby declare that this thesis is my own work and that, to the best of my knowledge and belief, it reproduces no material previously published or written, no material that has been accepted for the award of any other degree of diploma, except where due acknowledgement has been made in the text.

Signed:

Name of student: XIA NENGHONG

Department of Building Services Engineering

The Hong Kong Polytechnic University

Hong Kong SAR, China

July, 2013

Abstract

Thesis Title: PEEC Method for Evaluating Magnetic Shielding by Metal Structures at Low Frequency

Submitted by: XIA Nenghong

For the Degree of: Doctor of Philosophy

With the proliferation of electrical and electronic systems, the electromagnetic environment in modern buildings has been increasingly concerned as the EM fields can cause interference to sensitive equipment and potential adverse health effects. The EM field is mainly contributed by power equipment including cables running at power frequency. The large-size metal plates are frequently employed as barriers to isolate the power equipment from the public area. For the power lines passed through the office space, enclosures, such as metallic trunking is applied to isolate the wires from the outside world. The amount of reduction depends very much upon shield material and, its thickness, the size of the shielded volume and the frequency of the fields of interest. It is not unusual for the performance of a shield to be found unsatisfactory after the shield has been completely installed in a building. It is then necessary to have an efficient numerical tool for evaluation of shielding performance prior to shield construction and erection. Low-frequency magnetic field issues in the presence of metal parts have been addressed extensively, but the calculation methods developed are valid only for small-scale metallic elements or those metallic parts with simple geometry. In addition, the evaluation of magnetic environments in

buildings with large metal plates, where the skin effect is significant, has received only limited attention.

In this thesis, the partial element equivalent circuit (PEEC) method is developed for modeling of large and complex metal shields used in buildings. This method has been widely employed to study EM behavior on a wire structure. It provides a full wave solution to EM problems while transforming the problem into the circuit domain where circuit analysis techniques can be used. The focus of this thesis is to provide efficient solution procedures for the evaluation of low-frequency magnetic fields in the buildings. The characteristics of distribution of induced current and magnetization excited by a source current, and the resultant magnetic fields will be investigated by using the following proposed numerical methods.

First of all, the classic PEEC method (named “M0”) based on the uniform distribution of EM components on the plates is provided. Both non-magnetic and magnetic materials have been considered for investigation. In non-magnetic plates, the solutions of both induced current and the resultant magnetic field around the plate can be obtained easily. In magnetic plates, the magnetizing current needs to be taken into account, and the skin effect becomes an important factor. Due to the significant variation of EM components inside the metal plate, the dense grid is required and the method is hard to model large structures. However, the high accurate results can be obtained when there is a high density of grid.

Secondly, the analytical expression of double exponential function arising from the skin effects is applied to describe the variation of both induced current and magnetization. With this approximation the discretization over the cross section of the plate is avoided and a new method (named “M1”) is proposed, where the number of unknowns is reduced greatly and the accuracy is retained. Due to the irregular distribution of EM components is existed when magnetic material is involved, the non-uniform meshing is assigned for the plate corresponding to the location of external current sources. The refinement is particularly done in the edge area to improve the accuracy of solutions.

Especially, an improved method (named “IM1”) is also presented for the non-magnetic thin plate. In this method, the electric field integral equation is established on the middle plane of the plate. There is only one unknown for each cell. The total number of unknowns is then reduced. It is efficient to solve the eddy-current or shielding problems containing non-magnetic plates.

Thirdly, after investigation of the irregular distribution of EM components on the edge region of the plate, a hybrid method (named “M3”) using both M0 and M1 is proposed. This method is particularly for magnetic material. The distribution of EM components on the majority area is determined by an analytical expression. On the edge region, the mesh refinement is assigned where the EM components are assumed to be constant in each cell. This method reduces the number of unknowns in the central area and improves the accuracy in the edge region.

Fourthly, a new method (named “M2”) based on volume and surface cell is proposed. The contribution to the vector potential from the magnetization can be divided into two parts, one is associated with the volume current and the other is with the surface current. The former one has an algebraic relation with the induced current. Therefore, this item can be merged with the item contribution to the induced current. The EM components now become the induced current distributed in volume cell and the magnetization current on the surface cell. This method provides a new way to process the magnetization current just on the surface of the object.

M0 and M1 can be used to model both non-magnetic and magnetic structures, M2 and M3 are particular for magnetic material. M0 is available to simulate small shielding structures and validate the other numerical models. M1 is convenient for modeling and easy to understand. This procedure is simple and suitable for practical engineering problems. M2 processes the magnetization on the outer surface and is meaningful when the thickness is comparable to the other characteristic dimensions of the plate. M3 is a hybrid method and has more accuracy compared to other methods although there is a considerable amount of unknowns. It is suitable for investigation the characteristics of distribution of induced current and magnetization.

To solve the shield problem efficiently use the proposed methods, the techniques for reduction the number of unknowns, such as loop method and the symmetrical modeling technique have also been proposed. All the above

methods and techniques have been validated by numerical approaches and experiments.

Finally, the proposed PEEC modeling methods and techniques have been applied to establish complex computation models for actual shielding structures, such as large shielding plates and “U-shape” shields.

The main contributions of this thesis are listed as follows:

1. Different numerical methods (M0, M1, M2 and M3) have been proposed and discussed. The corresponding solution packages have been developed.
2. Every solver based on the method (M0, M1, M2 and M3) contains 2D and 3D modules, which can be used to deal with different cases.
3. The non-uniform meshing techniques for PEEC models have been proposed.
4. The techniques, such as loop method and the symmetrical modeling technique have been proposed for reduction of the number of unknowns.
5. Application of the proposed PEEC numerical methods for evaluating the shielding characteristics and performance in the presence of metal shields, including different structures, materials, frequencies, etc.

Publications

I. Papers in Journals

- Nenghong Xia; Du, Y., "Reduction of PEEC Unknowns for 3D Metallic Plates in Magnetic Shielding," *Magnetics, IEEE Transactions on* , vol.49, no.5, pp.2001,2004, May 2013.
- Du, Y.; Nenghong Xia; Mingli Chen, "Joint Modeling for Conductive Plates in Low-Frequency Magnetic Shielding," *Magnetics, IEEE Transactions on*, vol.49, no.5, pp.2005, 2008, May 2013.
- Du, Y. and N. Xia, *Principles of power-frequency magnetic shielding with finite-width plates.* International Transactions on Electrical Energy Systems, 2013: p. n/a-n/a.

II. Papers in Conferences

- Du Ya Ping, Xia Nenghong, "An Improved Method for Evaluating Low-frequency Shielding Performance of 3D Conductive Plate," *Electromagnetic Compatibility (APEMC), 2011 Asia-Pacific Symposium*, 16-19 May 2011.
- Xia Nenghong, Du Ya Ping, "Volume and Surface Elements-Based PEEC for Magnetic Plate Shielding at Low Frequency," *EMC Europe 2012 Rome*, 17-21 Sept. 2012.
- Xia Nenghong, Du Ya Ping, "An Efficient 3D Numerical Method for Modeling Large Ferromagnetic Plate Used in Magnetic Shielding at Power Frequency," *Electromagnetic Field Computation (CEFC), 2012 15th Biennial IEEE Conference.*

- Xia Nenghong, Du Ya Ping, "Modeling Techniques for Symmetrical 3D Metal Plates in Magnetic Shielding," *Electromagnetic Field Computation (CEFC), 2012 15th Biennial IEEE Conference.*
- Du Ya Ping, Xia Nenghong, "Modeling for the Joints of Conductive Plates in Magnetic Shielding," *Electromagnetic Field Computation (CEFC), 2012 15th Biennial IEEE Conference.*

III. Papers Accepted

- Xia Nenghong, Du Ya Ping, "An Efficient Modeling Method for 3D Magnetic Plates in Magnetic Shielding," *IEEE Transactions on Electromagnetic Compatibility.*

Acknowledgements

First and foremost, I would like to thank to my supervisor, Prof. Du Yaping, from Department of Building Services Engineering, the Hong Kong Polytechnic University, for the valuable guidance and advice and readily supervision. Then, I would like to express my thanks to Dr. Chen Mingli, for his kindly encouragement during this research.

In addition, I would also like to thank senior instructor Mr. Leung Chun-sing, and technical officer Mr. Fung Wing-kwong in the department for their help in the laboratory work in Hong Kong.

I also highly appreciate Dr. Zhou Qi-bin, Mr. Wang Xinghua and Mr. Chen Hongcai for their great help.

Finally, the deepest appreciation goes to my family and friends for their understandings and supports on me in completing my study.

Contents

List of Figures

1. Introduction

1.1. Magnetic Shielding at Low Frequency

As business demands on electric power in modern buildings continue to grow, more and more power equipment and cable networks are being installed. The electromagnetic environment in the buildings is becoming worse.

In one hand, the EM fields are inevitably the disturbance to electric and electronic devices (e.g. TV and computer monitors, oscilloscopes, electron microscopes and hospital imaging equipment). This disturbance may interrupt, obstruct, or otherwise degrade or limit the effective performance of the circuit. The effects can range from a simple degradation of data to a total loss of data [92]. Most countries have legal requirements that mandate electromagnetic compatibility: electronic and electrical hardware must work correctly when subjected to certain amounts of EMI, and should not emit EMI, which could interfere with other equipment (such as radios) [1-8]. In Switzerland and Italy, there have existed regulations related to the permitted values of the magnetic field induction in new public constructions.

On the other hand, the concerns about the potential adverse health effects due to magnetic field exposure, in some way confirmed by the International Agency for Research on Cancer (IARC) [9], have been increasing. In recent years, many research programs on the environmental impact of EM fields have been running with the aim to avoid or reduce potential health risks. Topics of these programs are focused on the characterization of EM environments critical for the human

exposure, the estimation of biological effects, the techniques of measurement and control of the EM fields. Some research shows that EM fields have a significant disruptive effect on the body's natural energy levels, alter how cells communicate, and magnify the “fight or flight” response. There are some publications which support the existence of complex biological effects of weaker non-thermal electromagnetic fields (see Bio-electromagnetics), including weak ELF magnetic fields [10, 29] and modulated RF and microwave fields [19]. Furthermore, due to EM fields are invisible and insensible, it seems mystic and brings human more apprehension.

In modern buildings, the low frequency EM fields are mainly the magnetic field arose from power equipment and cables running at power frequency. Electromagnetic compatibility (EMC) has become an important part of electrical engineering in modern building design and has been taken into consideration in the electrical installation process. To avoid the potential EM interference and health problems, EM field assessment and its mitigation have been requested continuously by building tenants and even developers in the building design stage. With the study on the exposure to low frequency AC magnetic fields over the past several years, the knowledge of field characterization and effective control strategies has grown concurrently. It is now possible, through a comprehensive application of this knowledge, to create living and working environments that are essentially free of magnetic fields of the magnitudes that are sometimes associated with adverse health effects, or with

disruption to sensitive equipment.

EM shielding is one of measures for reducing the EM field in a space. It is achieved by blocking the field with barriers made of conductive or magnetic materials. Shielding is typically applied to enclosures to isolate electrical devices from the ‘outside world’, and to cables to isolate wires from the environment through which the cable runs. The shielding can reduce the coupling of radio waves, EM fields and electrostatic fields. The amount of field reduction depends very much upon the material used, its thickness, the size of the shielded volume and the frequency of the fields of interest, and the size, shape and orientation of apertures in a shield to an incident electromagnetic field.

The standard methods of designing shielding structures by numerical methods are usually fail when the large structures are exposed to the low frequency (LF) magnetic fields (such as the one generated by power lines). It can be explained by the difficulty posed in the computing process by the large aspect ratios involved due to thin layers of metal (a few millimetres or centimetres) in contrast to the large dimensions of the affected structure (several tens of meters). In some cases one has to utilize special approximations such as surface conductivity, which are not easy to handle when the designed shielding structure is clearly three -dimensional. Other alternatives such as experimentation in situ are very costly.

EM shielding using metal plates is one of the practical ways of achieving compatible EM environments in buildings, and is often adopted when other

measures are not allowed or are difficult to apply in the buildings context. Such shields can be made using building structural components, such as metal decking and raised floor panels, or using additional metal plates installed on floors, ceilings and walls. It is not unusual for the performance of a shield to be found unsatisfactory after the shield has been completely installed in a building. An efficient design of these shielding systems requires computational techniques capable of modeling accurately the shape and geometry of the ELF sources and of computing the currents induced in conductive plates.

As a result, there is an increasing demand for effective and low-cost mitigation of low-intensity power-frequency magnetic fields. This yields to the conclusion that a reduction of the magnetic field due to power lines has to be pursued, especially if costs can be minimized at the design stage or low-cost remedies can be applied in existing installations. From the design point of view, it is useful and necessary to have at disposal an efficient numerical tool able to predict the magnetic field reduction prior to shield construction and erection, in a given region of space, as a function of the shield characteristics (geometry, material) and source characteristics (conductors disposition, distance from the shield).

1.2. Computation Methods

The low-frequency magnetic field in the presence of metal parts has received much attention in the study of magnetic shielding, eddy current and others [23, 36, 38, 54, 57, 88, 101]. Most of the research work has focused on problems involving the structures of wires, plates or cylindrical shells. These problems

have usually been solved using analytical approaches, "field" approaches or "circuit" approaches.

Analytical approaches are only applicable to metal parts possessing a simple geometry [50, 51]. Using the methods of separation of variables and conformal transformation, closed-form formulas applicable to electric and magnetic fields have been derived for 2D cylindrical or similar structures [99], and for simple planar structures [59, 97]. The shielding formulas for multiple-layer shields at low frequency have been addressed as well [58, 98]. These formulas are very useful in addressing general principles of magnetic shielding and general characteristics of magnetic fields around metal structures. However, they cannot be applied to complex structures or imperfect structures, such as shields of finite size or containing joints and seams, etc.

In field approaches a field problem is represented by a mathematical formulation derived from Maxwell equation and solved numerically. In general, the problem domain is discretized into small elements, and the field variable in the domain is substituted with an unknown vector. A matrix equation is then established in accordance with the formulation adopted, and solved numerically. The numerical modeling is a very efficient and cost-effective way to simulate the real-world electromagnetic compatibility (EMC) problems, which can provide insight into the problems and prediction for the engineering design. The recent decades have seen an impressive increase in the capabilities of numerical simulation tools and methods for the solution of EMC problems. Tremendous

progress in computing power has also taken place. In order to satisfy the increasing demands of industrial practice concerning EMC analysis, it was not sufficient to utilize only the improved computer equipment, rather new computational methods and variants had to be developed.

It is now feasible to solve many complex circuit analysis and electromagnetic problems. Thousands of unknowns can be solved in minutes. However, the focus remains on how to solve very large and complex problems more quickly. Model reduction research is a very active area focusing on minimizing model complexity in order to reduce solution time. Moreover, most of these numerical methods are based on two-dimensional (2-D) electromagnetic field analysis, which provides useful results for some preliminary evaluations. For instance, analytical techniques such as the variable separation method (VSM) or the conformal mapping (CTM) have been used to get closed-form solutions [12]. However, the 2-D assumption strongly limits the applicability of these methods in practical cases. Thus a three-dimensional (3-D) approach is needed to perform a reliable field analysis at the design stage.

On the other hand, the common 3-D commercial codes do not seem to be particularly suited to treat these kinds of problems. In fact, they are usually based on differential formulations, such as the finite-element method (FEM) or the finite-volume method (FVM), which can easily take into account all the geometrical parameters and material characteristics but are not particularly suited to manage the far-field boundary conditions. Moreover, several numerical

problems arise when very thin domains, such as conductive plates, have to be discretized, because of the great number of variables required. Instead, hybrid and integral formulations have peculiar advantages since only the active parts of the model have to be discretized, thus reducing the amount of allocated memory and computing time [13, 17].

In the following, a brief introduction of the most important numerical methods, such as the method of moments (MoM) [78], the finite element methods (FEM) [71,75], the finite differences in time domain (FDTD) [56], the boundary element method (BEM), and the method of partial element equivalent circuits (PEEC) [82], will be characterized firstly, and then the discussion of application of these numerical methods to metal shield structures. Generally these numerical methods can take into account all the geometrical parameters and material characteristics of conductive bodies. For any of these methods there exist quite powerful implementations. Any of these methods has its own advantages and disadvantages for specific problems [26, 37, 55, 61, 63, 64, 89].

The MoM was introduced into computational electromagnetics by Harrington in the 1960s, and it was possible to treat problems in the frequency range up to the first resonances. In the MoM, integral based equations, describing as an example the current distribution on a wire or a surface, are transformed into matrix equations which are easily solved using matrix inversion. When using the MoM for surfaces a wire-grid approximation of the surface can be utilized as described in [20]. Since the memory size required increases with number of

unknown current amplitudes N according to N^2 and the computation time as N^3, the applicability of the MoM was limited to relatively small structures, measured in wavelengths. However, by using bright matrix reduction techniques the computational costs could be reduced to $logN$.

The FDTD method was introduced in a seminal paper by Yee in 1966 [56]. Its broad application to open-space problems was only possible once the perfectly matched layer (PML) technique had been developed by Berenger [49]. A third example is the TLM, where Johns [70] developed the symmetrically condensed node (SCN) and made TLM an efficient alternative. The FDTD method has a natural advantage in the treatment of time dependent, broadband, nonlinear phenomena and complex inhomogeneous materials. The method is widely used within EM modeling mainly due to its simplicity. The FDTD method can be used to model arbitrary heterogeneous structures, for instance, PCBs and the human body [45]. In the FDTD method finite difference equations are used to solve Maxwell's equations for a restricted computational domain. The method requires the whole computational domain to be divided, or discretized, into volume elements (cells) for which Maxwell's equations have to be solved. The volume element sizes are determined by considering two main factors:

1. Frequency. The cell size should not exceed $\lambda/10$, where λ is the wavelength corresponding to the highest frequency in the excitation.

2. Structure. The cell sizes must allow the discretization of thin structures.

The finite element method (FEM) [48] is a powerful numerical technique for

handling problems involving complex geometries and heterogeneous media. The method is more complicated than the previously mentioned FDTD method but also applicable to a wider range of problems. FEM is based on the differential formulation of Maxwell's equations in which the complete field space is discretized. The method has advanced rapidly in areas such as waveguide problems, microstrips, semiconductor devices, and absorption of electromagnetic radiation in biological bodies. Good introductions to FEM can be found in [60] and [72]. An important feature of the FEM is that it includes the ability to describe the geometry or the media of a given problem with great flexibility. The reason for this is that the geometrical domain of a boundary value problem can be discretized using flexible nonuniform subdomain elements, which is necessary to describe complex geometries. The subdomain elements are called finite elements. The FEM has a strong resemblance to the MoM because both methods convert either a differential or an integral equation into a matrix equation. As a distinct variation from the MoM, the FEM is based on the physical principle of minimizing the energy of a system [20]. The problem of integrating the partial differential equations (PDE) is replaced by the equivalent problem of seeking a function that gives a minimum value of a particular integral. Problems of this type are called variational problems. Although both timeand frequency-domain formulations of FEM are known, most implementations have been in the frequency domain.

These methods have been successfully applied to small-scale 3D problems at

low frequency. In the presence of thin metal plates the EM field has been solved with FEM in [11, 65], BEM [18] and hybrid FEM-BEM [43, 66]. It is, however, noted that both variational-based FEM and differential-based FDM find it difficult to handle an open-boundary problem, such as the large plate problem. It was also noted that the matrix equation developed in BEM could be singular or nearly singular when plate thickness is much less than its width and length. All these methods need a large number of discretizing elements in the volume of concern or on the surface of conductors, especially in the problem concerning multiple conductors. This requires much computer memory and costs a significant amount of CPU time. Furthermore, it is difficult to integral external circuit components (e.g., wire-grid building structure) into these formulations unless they become a part of the problem to be solved. It is also difficult to handle a problem with seams and joints on the plates using these methods. Moreover, these approaches yield inaccurate results if the eddy current in the plate is significant and the current density is unevenly distributed across its thickness. In addition, they are not applicable to ferrous plates.

In circuit approaches the metal part of concern is divided into a number of small elements. Each element is represented by circuit components, such as a DC resistance and inductance. An equivalent electric circuit network is then formulated. A general-purpose network analysis program is used to find both voltages and currents and subsequently the magnetic fields. In these approaches a field problem is transformed into an equivalent circuit, and solved using circuit

analysis techniques. Such approaches are generally applicable to problems at extremely low frequency.

These numerical methods have been applied to address low frequency magnetic field issues, but there are several limitations or weakness:

1) The calculation methods developed are usually valid only for small scale metallic elements or those metallic parts with simple geometry;
2) Both FEM and FDM are difficult to handle an open-boundary problem, such as the large plate;
3) In BEM, the established matrix equation could be or nearly singular when plate thickness is much less than its width and length;
4) For these methods, there are heavy requirements for computer memory and CPU time due to the large number of discretized elements;
5) It is difficult to integral external circuit components (e.g., wire-grid building structure) into these formulations unless they become a part of the problem to be solved;
6) It is also difficult to handle a problem with seams and joints on the plates using these methods;
7) These approaches yield inaccurate results if the eddy current in the plate is significant and the current density is unevenly distributed across its thickness;
8) The skin effect of the plate has received only limited attention.

The partial element equivalent circuit (PEEC) approach is a full-wave circuit

modeling approach based on an electric field integral equation [16]. This approach is primarily used for circuit analysis in three-dimensional multi-conductor systems, such as integrated circuit packages and wises or conductors located on dielectric layers with ground planes. In this approach the circuit parameters of a PEEC cell, such as partial inductance, coefficient of potential and resistance are determined with the assumption of locally constant current density or surface current. When the skin effect of a conductor is significant, fine meshing of the conductor is necessary [25]. This, however, increases the number of unknowns and the complexity of solution. Moreover, there is no literature about the PEEC application to low frequency shielding in a wire-plate structure made of either magnetic or non-magnetic material. Nevertheless, for this proposed study the PEEC studies [15, 21, 41, 46, 47, 90, 100] shed insight into plate modeling, parameter calculation and solution procedures.

This method uses the Mixed Potential Integral Equation (MPIE). By employing a specialized discretization, the original structure is converted into a network of lumped inductances, capacitances and resistances, entitled partial elements. The electromagnetic coupling is modeled using partial mutual elements which results in an electromagnetic circuit model where additionally discrete components like transmission lines and voltage/current sources are easily included. The partial elements are calculated either by using numerical integration techniques or simplified closed form equations. The resultant

equivalent circuits are solved with, for example, conventional circuit solvers like SPICE [67] or ASTAP [95] where the same equivalent circuit can be used to obtain results in the time and frequency domain.

With the proposed approach, it is available to engineers for the design of large shields. General guidelines providing effective solutions can be available. The work outputs will enable better planning and installation of sensitive equipment in buildings, and improving the robustness of building intelligence and other electronic system.

1.3. Focus of This Work

In order to study the characteristics of the mutual coupling among the interconnect metal structures and evaluate the shielding performance contributed by the metal structures used in buildings, a series of effective numerical procedures based on the partial element equivalent circuit (PEEC) method have been developed. The corresponding numerical packages have also been developed.

The shielding structures are made of either magnetic or non-magnetic material. By using the PEEC method, both the structures and the conductive wires are modeled as a set of interconnected and coupled circuit components. The induced current and magnetization in the structures are then solved using basic circuit theory. The resultant field around the structures is computed by using the source current and the solved excited components.

In order to reduce the unknowns, the analytical expression of double

exponential function is applied to describe the distribution of electromagnetic components along the thickness of the structures.

Different numerical methods (M0, M1, M2 and M3) have been presented. M0 and M1 can be used to model both non-magnetic and magnetic structures. M2 and M3 are particular for magnetic material. M0 is available to simulate small shielding structures and validate other numerical models. M1 is convenient for modeling and easy to understand. This procedure is simple and suitable for practical engineering problems. M2 treats the magnetization on the outer surface and is meaningful when the thickness is comparable to the other characteristic dimensions of the plate. M3 is a hybrid method and has more accuracy compared to other methods although there is a considerable amount of unknowns. It is suitable for investigating the characteristics of distribution of induced current and magnetization.

To solve shielding problems efficiently with the proposed methods, the techniques for reduction the number of unknowns, such as loop method and the symmetrical modeling technique have also been proposed. All the above methods and techniques have been validated by numerical approaches and experiments.

The proposed PEEC modeling methods and techniques have been applied to simulate large, complex shielding structures, such as large shielding plates and “U-shape” shields.

The main contributions of this thesis are listed as follows:

1. Different numerical methods (M0, M1, M2 and M3) have been presented and discussed. The corresponding solution packages have been developed.
2. Every solver based on the method (M0, M1, M2 and M3) contains 2D and 3D modules, which can be used to process different cases.
3. The non-uniform meshing techniques for PEEC models have been proposed.
4. The techniques, such as loop method and the symmetrical modeling technique have been proposed for reduction of the number of unknowns.
5. Application of the proposed PEEC methods for evaluating the shielding characteristics and performance in the presence of metal shields, including different structures, materials, frequencies, etc.

1.4. Brief Outline of This Dissertation

Chapter 1 introduces the background of the research conducted in this thesis, and presents the objectives of this thesis. Brief introduction and discussion of the common numerical methods are presented.

In Chapter 2, introduction of the PEEC method is given firstly. Then the fundamentals of the basic PEEC formulation are given. A detailed derivation of the equivalent circuit is also presented. The geometrical discretization of plate in PEEC modeling is given. From this, the equivalent circuit representations are shown for a simple example.

In Chapter 3, the classic PEEC method (named “M0”) based on the uniform distribution of EM components in any cell is provided. Both non-magnetic and

magnetic materials are considered for investigation. In non-magnetic plates, the solutions of both induced current and the resultant magnetic field around the plate can be obtained easily. In magnetic plates, the magnetizing current needs to be taken into account, and the skin effect becomes an important factor. Due to the significant variation of EM components inside the metal plate, the dense grid is required and the method is hard to model large structures. However, the accurate results can be obtained when there is a high density of grid. M0 is available to simulate small structures and to validate other numerical models.

In Chapter 4, the analytical expression of double exponential function based on the skin effect is applied to describe the variation of both induced current and magnetization. With this approximation the discretization over the cross section of the plate is avoided and a new modeling method (named “M1”) is proposed, where the number of unknowns is reduced greatly and the accuracy retains. Due to the irregular distribution of EM components in magnetic plates, non-uniform meshing is adopted in the area of plate close to the external current sources. Refinement is done as well in the edge area to improve the accuracy of solutions. In addition, an improved method (named “IM1”) is presented for the non-magnetic thin plate. In this method, the electric field integral equation is established on the middle plane of the plate. There is only one unknown for each cell. The total number of unknowns is then reduced. It is efficient to solve the eddy-current or shielding problems containing non-magnetic plates.

In Chapter 5, a new method (named “M2”) based on volume and surface

element is given. The contribution to the vector potential from the magnetization can be divided into two parts, one is associated with the volume current and the other is with the surface current. The volume current has a simple relation with the induced current. Its contribution can be merged with the item of the induced current. The EM components to be solved for now become the induced current distributed in volume cell and the magnetization current on the surface cell. This method provides a new way to simulate the magnetization current just on the surface of the geometry.

In Chapter 6, the techniques for reducing the number of unknowns, such as loop method and the symmetrical modeling technique are presented.

In Chapter 7, the proposed different PEEC modeling methods are compared. The suitable method with the meshing and reduction techniques is applied for the large metal plate and U-shape structure used in buildings. The numerical application is validated by experiments as well.

In Chapter 8, the conclusion of this thesis is presented. A series of meaningful works are listed for further developing.

2. The Method of PEEC

The partial element equivalent circuit (PEEC) method is derived from the Maxwell equations and can be used to model the electromagnetic behavior of arbitrary three-dimensional electrical interconnection structures [69]. In this chapter, a review of the PEEC method is presented firstly. Then, in view of the sinusoidal steady state circumstances at low frequency in this study, the PEEC equation system in frequency domain is derived in a general form based on the electric field integral equation (EFIE). The orthogonal rectilinear meshing is adopted for discretization of thin, finite plates. Both the brick-shaped cells in three dimensional (3D) cases and the orthogonal rectangular grid in two dimensional (2D) cases are presented. Different ways for establishing the EFIE are presented and discussed. A simple 3 cell conductor example is used to interpret the PEEC model. Finally, the implementation of PEEC method has been presented, including the 3D model and 2D model for both non-magnetic and magnetic structures.

2.1. Introduction to PEEC

The PEEC method was proposed initially by Albert Ruehli at IBM Thomas J. Watson Research Center in 1972, when he published a very detailed and thorough paper on inductance calculations [80]. The major motivation for this work was the quasi-static analysis of inductive voltage drops and inductively coupled voltages for a large number of arbitrary loops of complex geometry. In which he introduced a circuit analysis theory of partial inductances based on the

inductance of pieces of wire. With this partial inductance concept, the complicated geometry could be thought of in terms of the partial inductance of many small touching segments. This provided the foundation for computing inductances for complicated structures through the use of generalized building blocks.

Also in 1972, Ruehli introduced the concept of partial element equivalent circuit (PEEC) models using both partial inductances and partial coefficients of potential in his Ph.D. dissertation [79]. With this concept, a comprehensive understanding of the relationship between circuit and field theory was provided.

On the way to improve the analysis and design of integrated circuits, the calculation on capacitance using a Galerkin technique was developed by Ruehli and Brennan in 1973 [81]. In which, an efficient method of computing partial coefficients of potential was introduced for arbitrary three dimensional geometries. The derived expressions for the self and mutual potential coefficients of and between closely spaced conductor pieces both provided a high precision of calculation and minimized the computer storage without excessive computation times by complex capacitance calculations. This generalized building block approach was introduced in a generalized algorithm which provided a method of efficient computation for arbitrary structures.

In 1974, Ruehli published a paper on the concept of partial element equivalent circuit (PEEC) [82], which was developed as a numerical method for circuit-oriented modeling of the electromagnetic behavior of electric

interconnection structures. This paper provided a comprehensive interpretation of the circuit and field relationship using an integral equation approach. By taking into account retardation this approach provided full-wave models in the time and frequency domains and allowed conductor losses to be considered. The corresponding models lead to a flexible computer solution technique for the calculation of partial elements and for circuit analysis. Models of different complexity could be constructed to suit the application at hand.

In 1989, a PEEC formulation using nonorthogonal structures was extended for electrical simulation of printed circuit boards [62]. In 1990, Heeb and Ruehli [40] introduced a coefficient of potential model which included a controlled voltage source representing the retarded partial mutual couplings between cells.

An important extension of the PEEC formulation to include arbitrary, finite, homogeneous dielectric regions was given by Ruehli and Heeb in 1992 [84]. The extended PEEC formulation was derived for the case of lossless dielectrics. In 1993, the PEEC formulation for dielectrics was further extended to include lossy inhomogeneous dielectric materials by the combination of a new term for lossless dielectrics and a term for finite conductivity that was already included in the PEEC concept [32].

In the early 1990s, the PEEC formulation was being used to analyze radiated emissions from circuit structures for EMC applications. In addition, another area of interest for EMC analysis is scattering by an arbitrary field for noise immunity. In 1993, the PEEC formulation was extended to three-dimensional structures that

were illuminated by a nonhomogeneous incident electric field [85]. Within a circuit interpretation, incident fields were represented as independent voltage sources. This enabled the PEEC method to model scattering problems in an adequate form.

Another EMC application for the PEEC formulation is cable analysis. In 1994, a hybrid PEEC formulation was introduced to efficiently analyze cable structures [93]. In which, a multiconductor transmission line method was combined with a PEEC formulation. With this combination, both common mode and differential currents were computed.

Despite the fact that interconnection structures are passive, physically stable systems, time domain solutions of their models that are derived from integral equations such as PEEC, may show instabilities. As a general rule, the instability may be for two reasons: the numerical technique that is used for the time integration and the geometrical discretization that is required to obtain PEEC models. In [87] the discretization issue was addressed and a circuit motivated technique to stabilize the time domain solution was suggested for the eigenvalues of a very small problem. The proposed stabilization scheme consisted in breaking the partial self inductances into two equal parts along the length with a delay between the two partial mutual inductances where the delay was used as a tuning parameter. Using the insight of this work, a stabilization scheme was provided to enhance the stability of the PEEC formulation [34]. The numerical efficiency of this stabilization scheme was further improved in [35]. Additionally, a further

stabilization measure was proposed: introducing a damping resistor in parallel to each self-inductance of the PEEC model. In [74] the proposed stabilization scheme was investigated for a rectangular patch geometry in the time domain.

An important concern for improving the versatility of the PEEC method in analyzing interconnection structures was the consideration of the skin effect. Although the concept of partial inductances provided the possibility of considering the skin and proximity effects by partitioning an arbitrary conductor cross section into filaments, the high number of filaments and of magnetic couplings between them made an analysis of real interconnection structures practically impossible with PEEC modeling. In [25], an enhanced skin effect modeling for PEEC models was proposed. The method was based on the introduction of a global surface impedance (GSI) that accurately and efficiently modeled the quasi-static electromagnetic behavior of a two-dimensional lossy conductor (interior problem). Since the interior of the conductor cross section was discretized and incorporated into the formulation of the GSI model, it eliminated the need for a high-frequency volume filament approach. The GSI representation was to be integrated in the EFIE and, finally, in the PEEC model for solving the exterior problem.

With the PEEC formulation, an electric field integral equation is interpreted as equivalent circuits in order to accurately describe a given geometry providing a full wave solution to Maxwell's equations. The first step in obtaining a solution using the PEEC formulation is to divide the geometry into cells and compute the

equivalent circuit elements. With this, a systematic approach to forming circuit equations which enforces the continuity equation is used to form a system of linear equations.

Due to the size and complexity of modern computer packages model reduction and fast solutions are very desirable. Various modeling schemes can be used to reduce model complexity and increase the solution speed. In the last few years, a variety of PEEC model reduction techniques have been proposed by many researchers [28, 31, 42, 73, 76, 91]. Another approach for increasing the solution speed is to use a fast multipole technique which has gained importance for EM calculations. An example of this acceleration is given in [52] for a PEEC formulation.

Concerning the efforts for a systematic approach to form circuit equations for PEEC models, there are two well-known approaches that are modified nodal analysis (MNA) and modified loop analysis (MLA). The MNA approach was introduced in 1975 [24]. This approach is widely used for circuit simulation programs such as SPICE [14, 67]. The second approach is to write only loop currents and is called modified loop analysis (MLA) in 1974 [30], and further developed in 1978 [83]. The MLA approach is not widely used in circuit simulation due to the limitation of not having node voltages as observables.

Early PEEC formulations utilized general purpose circuit solver approaches for forming circuit equations and then for solving the resulting system of linear equations. Although these solvers are very general, they are not the most efficient

for the PEEC formulation. In particular, as the PEEC formulation is being used on a wide variety of applications, it is necessary to introduce modifications to both the MNA and MLA formulations to provide more efficient PEEC solutions. In 1993, the first application of a new condensed MNA method for the PEEC formulation was introduced. This condensed MNA method utilized a new coefficient of potential model which is more suitable for nodal analysis. As a result, the condensed MNA method provides a more efficient solution for the PEEC formulation with fewer unknowns.

In addition, in order to make the PEEC formulation as efficient as other method of moment formulations, a loop method was introduced in 1995 [33]. This loop method is based on the MLA approach and leads to a very efficient system of linear equations. Generalized stamps were also introduced specific to the PEEC implementation. In addition, this PEEC MLA formulation provides the ability to easily add arbitrary additional circuit elements.

A system of linear equations is formed using either a MNA, condensed MNA or MLA approach. The size of the system of equations can vary depending on which approach is used and on whether model reduction techniques are used. Once the system of equations is formed, a variety of solvers may be used.

The PEEC formulation is a full wave solution to Maxwell's equations in the circuit domain. With the extensions of the last decade, the PEEC formulation is being used as a design tool for a wide variety of applications including circuit design, EIP and EMC. By exploiting circuit analysis techniques, the PEEC

formulation can also be used to analyze and design various complex circuit or numerical issues. Due to the basic mathematical formulation, PEEC is fundamentally more suited to classes of problems identified as dense and electrically large [16]. For the future applications with combined wave problems will be of very high interest.

2.2. Fundamental Equations

From Maxwell's Equations, the electric field due to charges and currents within a system under consideration can be derived directly or indirectly through the use of vector and scalar potentials. The details are given in [22]. According to electric field integral equation (EFIE), the electric field $\boldsymbol{E}$ at a point $\boldsymbol{r}$ can be given by the terms of vector and scalar potentials as follow:

$$\boldsymbol{E}(\boldsymbol{r}) = -j\omega\boldsymbol{A}(\boldsymbol{r}) - \nabla\varphi(\boldsymbol{r}) \tag{2.1}$$

where $\boldsymbol{A}$ is the vector potential term, φ is the scalar potential term, in the free space they are given by:

$$\boldsymbol{A}(\boldsymbol{r}) = \mu_0 \int_{v'} G(\boldsymbol{r}, \boldsymbol{r}')\boldsymbol{J}(\boldsymbol{r}')dv' \tag{2.2}$$

$$\varphi(\boldsymbol{r}) = \frac{1}{\varepsilon_0}\int_{v'} G(\boldsymbol{r}, \boldsymbol{r}')\rho(\boldsymbol{r}')dv' \tag{2.3}$$

where $\boldsymbol{J}$ is the current density and ρ is the charge density in the source volume v', G is the free space Green's function, which is a response function relating the field point ($\boldsymbol{r}$) and the source point ($\boldsymbol{r}'$), and is given by:

$$G(\boldsymbol{r}, \boldsymbol{r}') = \frac{1}{4\pi}\frac{e^{-jk|\boldsymbol{r}-\boldsymbol{r}'|}}{|\boldsymbol{r}-\boldsymbol{r}'|} \tag{2.4}$$

where k is given by $k = \frac{\omega}{c}$, and $c = \frac{1}{\sqrt{\varepsilon_0\mu_0}}$ is the speed of light in free

space. μ_0 and ε_0 are the permeability and permittivity in vacuum, respectively.

The method of Green's functions is a general method for the calculation of electromagnetic fields for given sources and boundary conditions. The phase term $e^{-jk|\boldsymbol{r}-\boldsymbol{r}'|}$ which is called retardation, in the time domain, it results in a delay called retarded time. In view of the sinusoidal steady state circumstances at low frequency in this study, the retarded time is neglected and $k \approx 0$. Therefore, the Green's function in a 3D free space is given as:

$$G(\boldsymbol{r},\boldsymbol{r}') = \frac{1}{4\pi R} \tag{2.5}$$

where $R = |\boldsymbol{R}| = |\boldsymbol{r} - \boldsymbol{r}'|$.

In the absence of an impressed source, for the good conductor $\sigma \gg |\omega\varepsilon|$, electric field strength in dependence on the location of the field point is:

$$\boldsymbol{E}(\boldsymbol{r}) = \frac{\boldsymbol{J}(\boldsymbol{r})}{\sigma} \tag{2.6}$$

where $\boldsymbol{J}$ is the current density, and σ is the conductivity of the conductor.

For low frequency applications in this study, capacitive effects can be neglected and the PEEC method can be restricted to its inductive formulation. The scalar potential φ can be defined at some points of the potential cells. Then, the electric field integration between these points constitutes a potential difference. With Equations (2.2), (2.3) and replacing $\boldsymbol{E}$ by $\boldsymbol{J}$, Eq. (2.1) can be rewritten as:

$$\frac{\boldsymbol{J}(\boldsymbol{r})}{\sigma} + j\omega\mu_0 \int_{v'} G(\boldsymbol{r},\boldsymbol{r}')\boldsymbol{J}(\boldsymbol{r}')dv' = -\nabla\varphi(\boldsymbol{r}) \tag{2.7}$$

This is the mixed potential integral equation (MPIE) in good conductors. The unknowns of this equation are the current density $\boldsymbol{J}$ and the scalar potential φ.

An MPIE for arbitrary shaped scatterers in free space has been developed by numerous authors [94].

When the concerned cases only involve non-magnetic materials, and the excited field defined to be the field due to an impressed current source in the absence of the scatterer, the vector potential is generated by induced current and external current sources:

$$\boldsymbol{A}(\boldsymbol{r}) = \boldsymbol{A}_c(\boldsymbol{r}) + \boldsymbol{A}_s(\boldsymbol{r}) \tag{2.8}$$

and the two items are given as:

$$\boldsymbol{A}_c(\boldsymbol{r}) = \mu_0 \int_{v'} G(\boldsymbol{r}, \boldsymbol{r}')\boldsymbol{J}(\boldsymbol{r}')dv' \tag{2.9}$$

$$\boldsymbol{A}_s(\boldsymbol{r}) = \mu_0 \int_{l'} G(\boldsymbol{r}, \boldsymbol{r}')\boldsymbol{I}_s(\boldsymbol{r}')dl' \tag{2.10}$$

where $\boldsymbol{A}_c$, $\boldsymbol{A}_s$ are the vector potentials produced by induced current and external current sources, respectively. $\boldsymbol{J}$ represents the induced current density in volume v' and $\boldsymbol{I}_s$ is the current of external source on the segment l'.

Then, Eq. (2.7) can be rewritten as follow:

$$\frac{\boldsymbol{J}_c(\boldsymbol{r})}{\sigma} + \frac{j\omega\mu_0}{4\pi}\int_{v'} \frac{\boldsymbol{J}_c(\boldsymbol{r}')}{R}dv' + \frac{j\omega\mu_0}{4\pi}\int_{l'} \frac{\boldsymbol{I}_s(\boldsymbol{r}')}{R}dl' = -\nabla\varphi(\boldsymbol{r}) \tag{2.11}$$

When the magnetic material is involved, the contribution to the magnetic vector from magnetic polarization needs to be added, and (2.8) can be rewritten as:

$$\boldsymbol{A}(\boldsymbol{r}) = \boldsymbol{A}_c(\boldsymbol{r}) + \boldsymbol{A}_s(\boldsymbol{r}) + \boldsymbol{A}_m(\boldsymbol{r}) \tag{2.12}$$

and the new item can be defined as:

$$\boldsymbol{A}_m(\boldsymbol{r}) = \frac{\mu_0}{4\pi}\int_{v'} \boldsymbol{M}(\boldsymbol{r}') \times \nabla' \left(\frac{1}{R}\right) dv' \tag{2.13}$$

where $\boldsymbol{A}_m$ is the vector potentials produced by magnetic polarization, and $\boldsymbol{M}$

is the magnetization density.

Then, the EFIE (2.7) will be rewritten as follow:

$$\frac{\boldsymbol{J}_c(\boldsymbol{r})}{\sigma}+\frac{j\omega\mu_0}{4\pi}\int_{v'}\frac{\boldsymbol{J}_c(\boldsymbol{r}')}{R}dv'+\frac{j\omega\mu_0}{4\pi}\int_{l'}\frac{\boldsymbol{I}_s(\boldsymbol{r}')}{R}dl' +\frac{j\omega\mu_0}{4\pi}\int_{v'}\boldsymbol{M}(\boldsymbol{r}')\times\nabla'\left(\frac{1}{R}\right)dv'=-\nabla\varphi(\boldsymbol{r}) \tag{2.14}$$

When the magnetization $\boldsymbol{M}$ is introduced as additional unknowns in modeling magnetic plates, additional equations are needed to make the problem well posed. Assume that the plate material is linear and is characterized by relative permeability μ_r. According to the constitution law:

$$\boldsymbol{B}(\boldsymbol{r})=\frac{\mu_0\bullet\mu_r}{\mu_r-1}\boldsymbol{M}(\boldsymbol{r}) \tag{2.15}$$

Note that magnetic flux density $\boldsymbol{B}$ is related to vector potential $\boldsymbol{A}$ by:

$$\boldsymbol{B}(\boldsymbol{r})=\nabla\times\boldsymbol{A}(\boldsymbol{r}) \tag{2.16}$$

The following equation then yields:

$$\frac{\mu_0\bullet\mu_r}{\mu_r-1}\boldsymbol{M}(\boldsymbol{r})=\nabla\times\boldsymbol{A}(\boldsymbol{r}) \tag{2.17}$$

2.3. Interpretation of the PEEC Model

For an explanation of the equivalent circuit in PEEC models, as an example, consider the conductor shown in Fig. 2.1 which has been discretized into 3 volume potential cells (cell i, j and k). For simplicity, assume that the induced current is only in the x direction. The scalar potential φ is defined at the center of the potential cell (φ_i, φ_j and φ_k). And this constitutes two current cells (cell m and n), which is defined as flowing between the middle cross section of adjacent two potential cells.

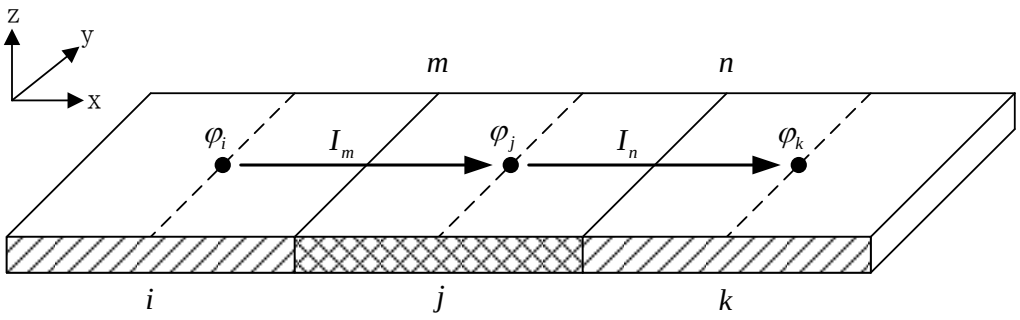

Figure 2.1 Three cells conductor example.

Figure 2.2 gives the equivalent circuit for the above example in frequency domain at low frequency. It clearly illustrates the Kirchhoff Voltage Law (KVL) on a branch in x direction. The law on the branches in y direction is the same as x direction. The application of the continuity equation to all nodes of the structure connects the nodes and delivers the node equations required for the calculation of the PEEC circuit. In Fig. 2.2, U_n^s represents the impressed voltage due to an external current source, and the mutual coupling arises from the current cells and magnetization cells are equivalent to the CCVS.

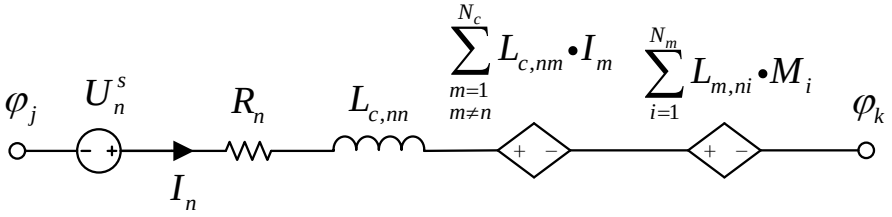

Figure 2.2 Equivalent circuit for PEEC models in frequency domain.

The branch voltage equation could be obtained as follow:

$$\begin{aligned} V_n &= \varphi_j - \varphi_k \\ &= -U_n^s + R_n I_n + j\omega\mu_0 \sum_{m=1}^{N_c} L_{c,nm} I_m + j\omega\mu_0 \sum_{i=1}^{N_m} L_{m,ni} M_i \end{aligned} \tag{2.18}$$

V_n is the branch voltage on cell n. The other equivalent partial components are given as:

$$U_n^s = j\omega \frac{\mu_0}{4\pi} \sum_{j=1}^{N_s} \int_{l_n} \int_{l_j'} \frac{\boldsymbol{I}_{s,j}(\boldsymbol{r}')}{|\boldsymbol{r}-\boldsymbol{r}'|} dl'dl \tag{2.19a}$$

$$R_n = \frac{l_n}{\sigma} \tag{2.19b}$$

$$L_{c,nm} = \frac{\mu_0}{4\pi} \int_{v_m'} \frac{\boldsymbol{J}_j(\boldsymbol{r}')}{|\boldsymbol{r}-\boldsymbol{r}'|} dv' \tag{2.19c}$$

$$L_{m,ni} = \frac{\mu_0}{4\pi} \int_{v_i'} \frac{\boldsymbol{M}_i(\boldsymbol{r}')}{|\boldsymbol{r}-\boldsymbol{r}'|} dv' \tag{2.19d}$$

$L_{c,nn}$ is the partial self inductance of cell n.

$L_{c,nm}$ represents the inductive coupling from cell m to cell n, i.e. the partial mutual inductance.

2.4. Orthogonal Cells

The rectangular cells, which conform to Cartesian coordinates, are the most widespread shapes in the PEEC literature. There are several main reasons for this are:

a) There are analytical solutions for calculating the double integrals in the expressions of the partial inductances and potential coefficients for cells oriented parallel to the coordinate axes, which enormously reduces the calculation expense (e.g. [44, 77]).

b) In practice, many interconnects, for example PCB traces, traces on VLSI and MMIC, but also busbars in power electronics, can be dissected in brick-shaped elements.

c) Besides a good suitability for a one-dimensional discretization of wire-like structures, brick-shaped cells or an orthogonal rectilinear meshing are very well suited for a two-dimensional discretization of thin,

finite plates and a three-dimensional discretization of finite volumes, for example if dielectrics have to be considered.

In this thesis, the structures under investigation are rectangular plates or configuration, therefore the rectangular cell is very suitable. A typical shielding structure, involved a regular metal plate, is presented to study the geometrical discretization. As seen in Fig. 2.3, the plate is placed horizontally, as the response to the current carried in the wires, the excited eddy current circulates in the plate.

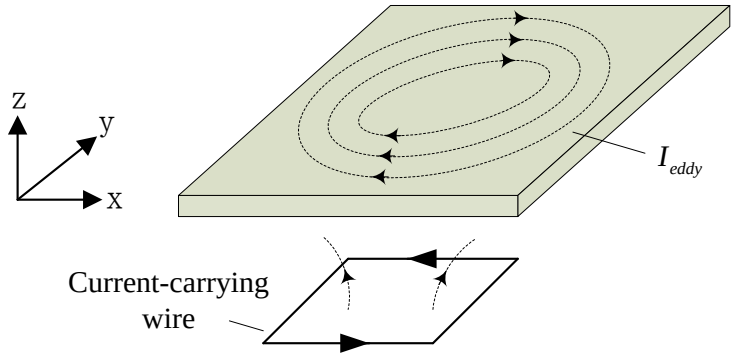

Figure 2.3 A typical shielding structure involved a regular metal plate.

1) Brick-shaped cells

In order to solve the eddy current numerically as a 3D model, the plate is divided into a number of potential cells with brick-shape. Figure 2.4(a) shows the discretization in potential and current cells for three-dimensional problems. As the eddy current flows between adjacent potential cells, current cells are formed by taking the volume between the centers of these adjacent potential cells, as seen in Figure 2.4 (b). If the plate is placed parallel to the x-y plane, the current cells are classified to two types, one is along x-direction and the other is

in y-direction.

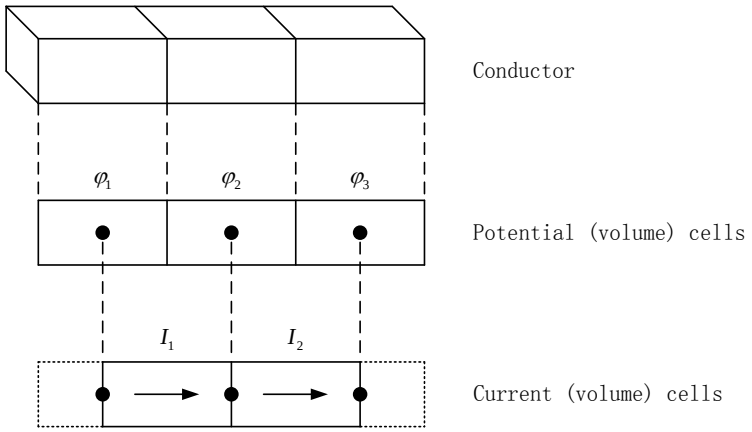

(a) Discretization of a rectilinear structure

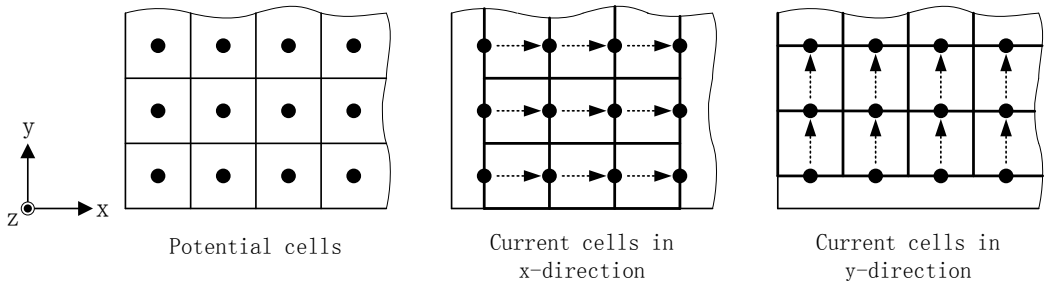

(b) Discretization of a thin finite plate

Figure 2.4 Discretization in potential and current cells for three-dimensional problems.

2) Rectangular cells

In some special cases, the geometry can be simplified as a two-dimensional model. For the plate with long length, as seen in Figure 2.5, and the concerned domain is on the cross section which is perpendicular to the direction of length, the plate can be modeled in the 2D region.

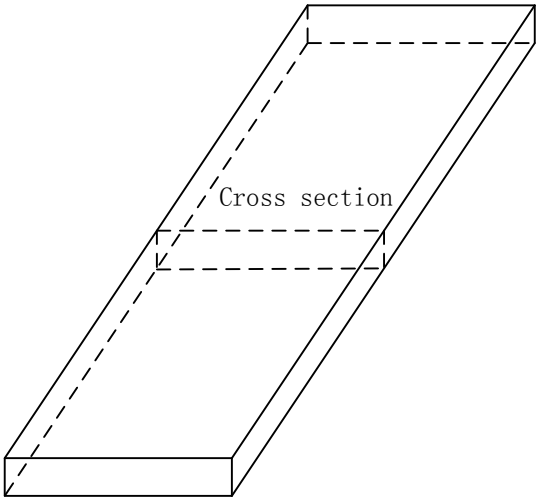

Figure 2.5 The special case can be modeled in 2D domain.

As seen in Fig. 2.6, the cross section of the plate has been discretized into some rectangular cells. The electromagnetic components in any a cell is constant. If the distribution is uniform over the thickness, the discretization along the thickness can be avoided (as seen in Figure 2.6(a)). Otherwise the cross section needs to be discretized as in Figure 2.6(b).

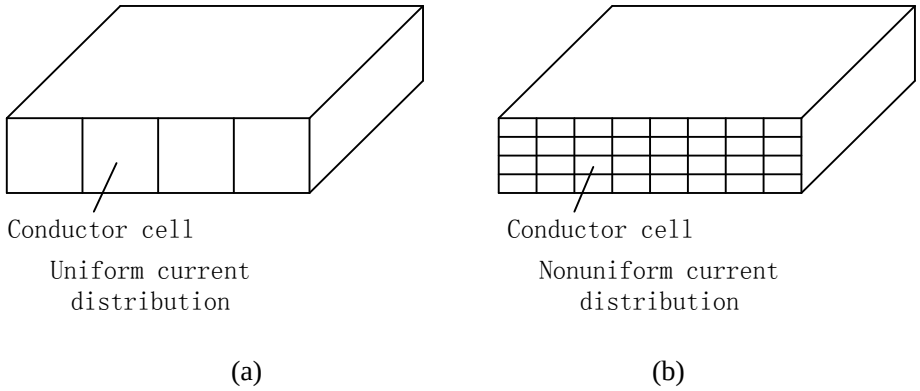

Figure 2.6 The segmentation of the cross section for two-dimensional problems.

2.5. Implementation of PEEC Model

2.5.1. Establishing the EFIE

The electric field integral equation (EFIE) should be established on a path and a potential difference will be generated. In the 3D PEEC model, the flat metal

plate is discretized into volume cells. Based on the volume cells, there are three ways to set up the integral equation, such as 1) integrated on a line segment, 2) set up on the surface, and 3) built in volume. They will be discussed in the following.

A) Based on the segment

In order to establish the EFIE, an integral path is required. As seen in Figure 2.7 (a), when volume cell *i* is treated as the observation object and another cell *j* is the source, the middle line l_i inside cell *i* is naturally selected as the integral segment. The equivalent partial elements are different on different segments inside the volume cell *i*. The middle line is the most appropriate choice. The EFIE on l_i can be expressed as:

$$v_i = \frac{1}{\sigma}\int_{l_i} \boldsymbol{J_i}(\boldsymbol{r})\bullet d\boldsymbol{l} + j\omega\int_{l_i} \boldsymbol{A}(\boldsymbol{r})\bullet d\boldsymbol{l} \tag{2.20}$$

where v_i is the potential difference on segment l_i. Equation (2.20) is the branch voltage equation.

When the induced current density distribution is constant on the segment, Eq. (2.20) can be rewritten as:

$$v_i = \frac{l_i}{\sigma} J_{c,i} + j\omega\int_{l_i} \boldsymbol{A}(\boldsymbol{r})\bullet d\boldsymbol{l} \tag{2.21}$$

B) Based on the surface

With a assumption that the induced current distribution only varies along the thickness, as seen in Figure 2.7 (b), the current distribution remains uniform on any a layer S_i. On different paths (such as l_m and l_n) inside the plane S_i, the equivalent local resistant is the same, but the equivalent local and mutual

inductances are different. For mitigating this difference caused by different locations, the coupling over the whole plane is taken into account. Then, the total coupling will be averaged to a segment which is parallel to the direction of current, such as the middle line of the plane is preferred. The EFIE on an average value can be expressed as:

$$v_i = \frac{l_i}{\sigma} J_{c,i} + \frac{j\omega}{w_i} \int_{S_i} \boldsymbol{A}(\boldsymbol{r}) d\boldsymbol{S} \tag{2.22}$$

where w_i is the width of cell *i*, and is perpendicular to the direction of current.

C) Based on the volume

When the induced current distribution is uniform over the total volume cell, the equivalent local impedance on any a segment (such as l_m and l_n) is the same. However, the couplings on different segments arose from the same source are different. In order to mitigate the coupling difference caused by location of integral segment, the accumulative mutual coupling on the whole observation volume cell has been calculated. Then the coupling will be averaged to segment, similarly, the middle line l_i of the volume cell *i* is preferred. And the EFIE on can be expressed as:

$$v_i = \frac{l_i}{\sigma} J_{c,i} + \frac{j\omega}{S_{i,yz}} \int_{V_i} \boldsymbol{A}(\boldsymbol{r}) dV \tag{2.23}$$

where $S_{i,yz}$ is the cross-sectional area of cell *i*, and is perpendicular to the direction of current.

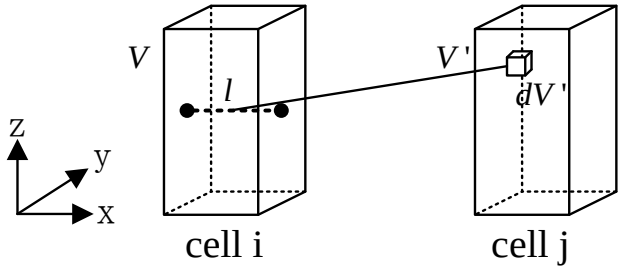

(a) Calculate the mutual coupling on the segment.

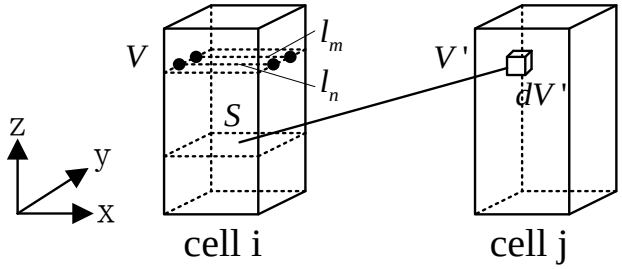

(b) Calculate the mutual coupling on the plane.

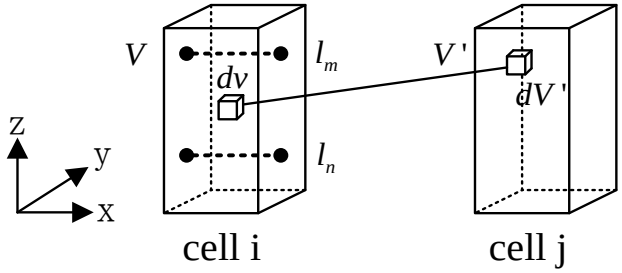

(c) Calculate the mutual coupling on the volume.

Figure 2.7 Three ways to set up the electric field integral equation.

It is clearly that the third way has the highest accuracy and the first one is at the lowest. However, the integral equations are mostly related to multiple integrals in practical problems, it is hard to analytically calculate and is a heavy burden for computer. By comparing the results from these three approaches, the difference is not significant when there is an adequate segmentation. Therefore, the first approach with minimal computational effort is selected to establish the EFIE.

In the 2D PEEC modeling, the computational region is a plane which involves

the cross section of the objective structure. Generally, the structure should be of sufficient length relative to the finite width, and the selected cross section is perpendicular to the length. Then, the induced current can be seemed as flowing perpendicularly into or out of the cross section, as seen in Figure 2.8. Thus, the EFIE can be established at the points distributed on the cross section, and the direction is perpendicular to the plane. It means that the potential difference arose by the EFIE is identical zero and the integral path is omitted. The EFIE is expressed as follow:

$$\frac{J_{c,i}}{\sigma} + j\omega \boldsymbol{A}(\boldsymbol{r}) = 0 \tag{2.24}$$

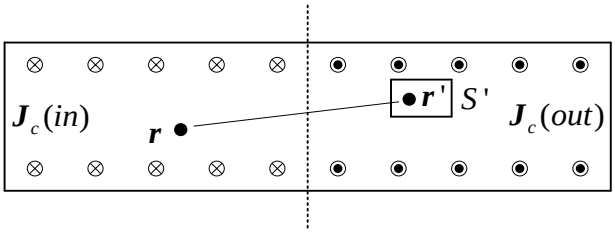

Figure 2.8 The 2D PEEC model on the cross-section.

2.5.2. Current balance

As the plate which is employed for investigation in this thesis is very thin, the normal component of the eddy current is negligible. The eddy current therefore circulates within the layers of the plate and does not go to other layers. As shown in Fig. 2.9, for any a layer of the plate, the induced current circulates within the layer along the tangential direction. There must be a relationship between the currents which are along the two orthogonal directions.

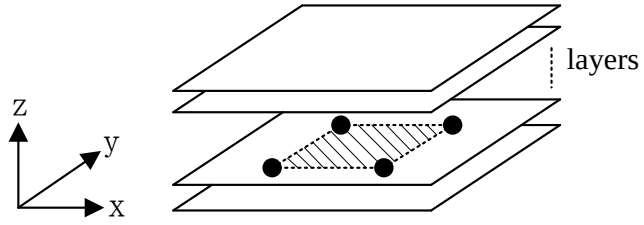

Figure 2.9 The layers of a plate.

As the discretization process has generated circuit topological entities as branches and nodes, in the PEEC method the continuity equation is enforced in terms of Kirchhoff's Current Law (KCL) to each node. Considering the eddy current circulates in the object, the corresponding matrix equation is:

$$\boldsymbol{A}_I I = 0 \tag{2.25}$$

where $\boldsymbol{A}$ is the connectivity matrix for induced eddy current.

2.5.3. PEEC Model

In order to solve the unknowns in Eq. (2.11), a system of equations needs to be generated. Following the usual discretization procedure, Eq. (2.11) can be enforced on a point $\boldsymbol{r}$ as:

$$\begin{aligned} -\nabla\varphi_i = \frac{\boldsymbol{J}_c(\boldsymbol{r})}{\sigma} + j\omega\mu_0 \sum_{j=1}^{N_C} \int_{V'} G(\boldsymbol{r},\boldsymbol{r}')\boldsymbol{J}_{c,j}(\boldsymbol{r}')dV' \\ + j\omega\mu_0 \sum_{j=1}^{N_S} \int_{l'} G(\boldsymbol{r},\boldsymbol{r}')\boldsymbol{I}_{s,j}(\boldsymbol{r}')dl' \end{aligned} \tag{2.26}$$

where N_c and N_s represent the number of elementary volumes for induced current and the source wires, respectively. The unknowns here are the current density $\boldsymbol{J}_c$ and the scalar potential φ.

Then, the complete solution matrix for non-magnetic object is established:

$$\begin{bmatrix} \mathrm{R}+j\omega\mathrm{L} & \mathrm{A_V} \\ \mathrm{A_I} & 0 \end{bmatrix} \begin{bmatrix} \mathrm{I} \\ \Phi \end{bmatrix} = \begin{bmatrix} \mathrm{U^S} \\ 0 \end{bmatrix} \tag{2.27}$$

R : diagonal matrix of local impedances;

L : matrix of generalized partial inductances, include local and mutual inductance;

A_V : connectivity matrix of scalar potentials;

A_I : connectivity matrix of currents;

I : vector of induced currents;

Φ : vector of scalar potentials distributes in the object;

U^S : vector of voltages arise from the external source.

In a similar manner, a system of equations of Eq. (2.14) for the magnetic material has the following form:

$$\begin{bmatrix} R+j\omega L & A_V & Q \\ A_I & 0 & 0 \\ B & 0 & P \end{bmatrix} \begin{bmatrix} I \\ \Phi \\ M \end{bmatrix} = \begin{bmatrix} U^S \\ 0 \\ B^S \end{bmatrix} \tag{2.28}$$

Q : matrix of mutual coupling from the magnetization to current cells;

B : matrix of mutual coupling from current cells to the magnetization;

P : matrix of mutual coupling among the magnetization;

M : vector of magnetization;

B^S : vector of magnetization arise from the external source.

3. General PEEC Solution

In traditional electromagnetic modeling methods, the problem domain is discretized into a series of volume or surface cells. An adequate possibility for taking into account the distributions of electromagnetic field variations inside the involved geometry is to choose a finer cross-sectional segmentation, so that in each of the segments the current distribution remains uniform. In each of these cells, the density of electromagnetic quantities are considered to be constant everywhere.

When the PEEC modeling method is applied to solve a shielding problem, uniform distribution of electromagnetic components in each cell is assumed. A traditional PEEC model for a shielding problem can be set up. This modeling technique is named ‘Method 0’ (M0) in this thesis. In this chapter both three-dimensional and two-dimensional PEEC models for flat metal plates made of non-magnetic or magnetic material are established and discussed. The numerical validation is carried out. The advantages and the limitations of this method are presented finally.

3.1. Segmentation of the Cross Section

As illustrated in section 2.4, it is necessary to take into account the variation of electromagnetic components when a discritization scheme is applied. For a thin flat metal plate, as seen in Fig. 2.6 (a), the discritization scheme using uniform current distribution in cells is normally accepted if the skin effect of the plate is not critical. Roughly speaking, the skin depth $\delta = \sqrt{2/\omega\mu_0\sigma}$ should be

greater than half of the cross-sectional dimensions. However, electric and magnetic couplings via mutual partial inductances of the cells lead to a non-uniform distribution of EM components over the whole cross section of the plate. The non-uniform distribution across plate thickness should be taken into account when the PEEC modeling method is applied, so that in each of the segments the distribution varies little. Figure 2.6 (b) shows the PEEC adequate solution: the segmentation of the cross section in current cells so that the current is uniformly distributed in each of them.

As seen in Fig. 3.1, a magnetic plate is uniformly discretized into a number of brick shaped cells. Both electric and/or magnetic currents are uniformly distributed in each volume cell.

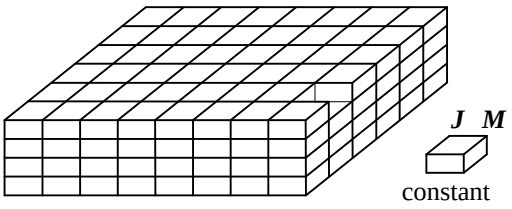

Figure 3.1 The electric and magnetic currents are uniformly distributed in each cell.

With this assumption, the unknowns in each cell are constant. As a result, the electric field integral equation (2.14) can be rewritten as follow:

$$
\begin{aligned}
-\nabla\varphi(\boldsymbol{r}) = \frac{\boldsymbol{J}(\boldsymbol{r})}{\sigma} &+ \frac{j\omega\mu_0}{4\pi}\sum_{j=1}^{N_c}\left(\int_{v_{c,j}'}\frac{1}{R}dv'\right)\bullet\boldsymbol{J}_j \\
&+ \frac{j\omega\mu_0}{4\pi}\sum_{j=1}^{N_m}\left(\int_{v_{m,j}'}\boldsymbol{b}_j(\boldsymbol{r}')\times\nabla'\left(\frac{1}{R}\right)dv'\right)\bullet M_j \\
&+ \frac{j\omega\mu_0}{4\pi}\sum_{j=1}^{N_s}\left(\int_{l_{s,j}'}\frac{1}{R}dl'\right)\bullet\boldsymbol{I}_{s,j}
\end{aligned}
$$

where $\boldsymbol{b}_j$ is the basis function of magnetization density M_j.

This is the PEEC equation for conducting magnetic material. When the non-magnetic material is presented, the item related to magnetization $\boldsymbol{M}$ will be cancelled.

3.2. 3D PEEC Model for Metal Plate

In practical problems, shielding structures are normally three dimensional (3D) as the structures irregular. Three-dimensional PEEC models are necessary to be developed for modeling practical shields. Large metal plates are frequently employed as the electromagnetic barriers to isolate power equipment from public areas. It is very useful and meaningful to understand shielding characteristics of large metal plates. An efficient numerical procedure for shielding evaluation is necessary. In this section, the 3D PEEC models for non-magnetic and magnetic metal plates at low frequency will be established.

3.2.1. Discretization of Metal Plate

The problem under investigation in this section consists of a metal plate excited by an external current source, as shown in Fig. 3.2. The plate is made from linear material, and is characterized with conductivity σ and permeability μ_0. The external source is set as a filamentary conductor wire carrying a a.c. loop current at low frequency, as seen in Fig. 3.3. The plate and conductive loop wire are modeled as a set of interconnected and coupled circuit components. The eddy current in the plate is solved using an equivalent circuit approach. The resultant field around the plates is then determined by both the current source and eddy current in the plates.

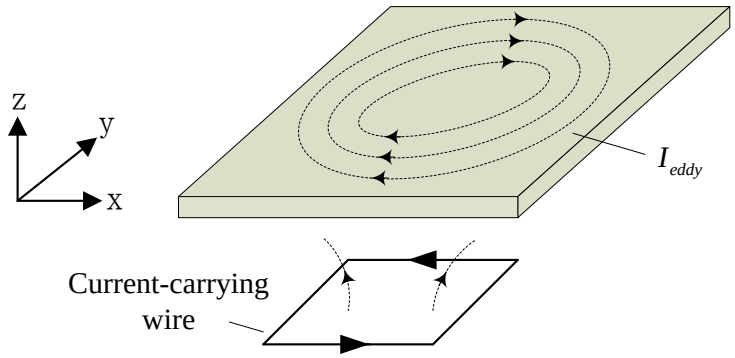

Figure 3.2 The wire plate structure under investigation.

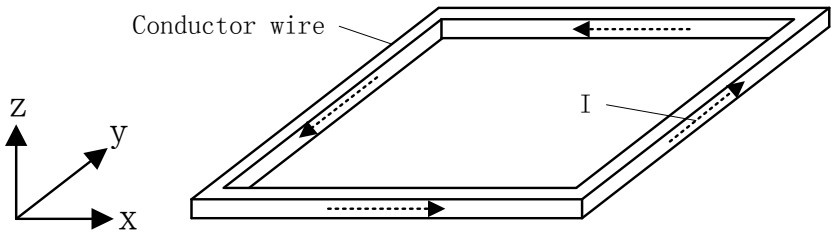

Figure 3.3 The filamentary conductor carrying a current ***I*** at a frequency *f*.

Shown in Fig. 3.4(a) is the discretization scheme for a rectangular metal plate placed horizontally. The plate is segmentalized into a number of brick-shaped volume cells, called potential cells. With the cell numbers of N_x, N_y, N_z cells in the x, y, z directions, respectively, as seen in Fig. 3.4(b). The induced current is considered to flow from the one potential cell to another adjacent potential cell, thereby a current cell is formed by taking the volume between the centers of two potential cells, as seen in Fig 3.4 (c) and (d) . As the thickness of the plate is much less than other characteristic dimensions, the normal component of the eddy current is negligible. The eddy current therefore circulates within the plate along the tangential direction. The current cells on the plate are classified into two types, which carry the currents in two orthogonal directions. These cells are named X cells and Y cells, as shown in Fig. 3.4(c)-(d). The numbers of X cells

and Y cells $N_{cx} = (N_x - 1) \times N_y$ and $N_{cy} = N_x \times (N_y - 1)$, respectively.

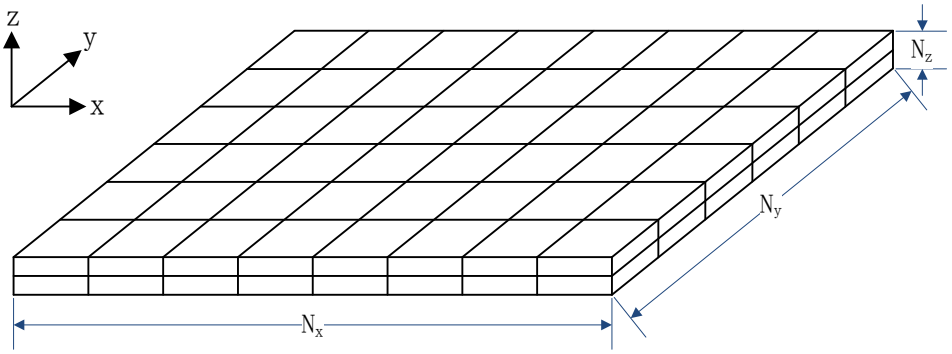

(a) The flat metal plate.

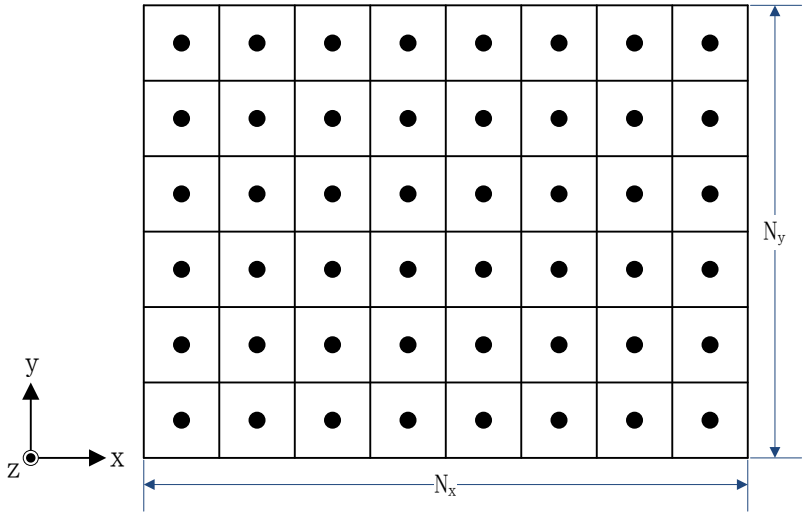

(b) The potential cells.

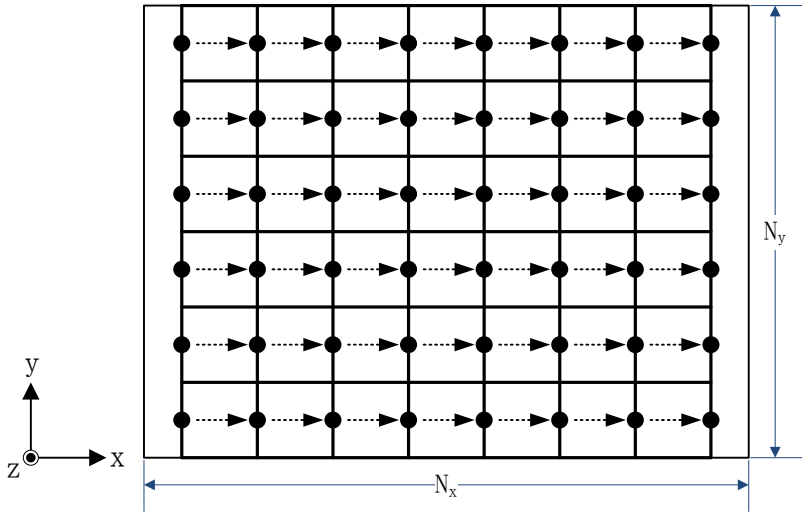

(c) The X cells.

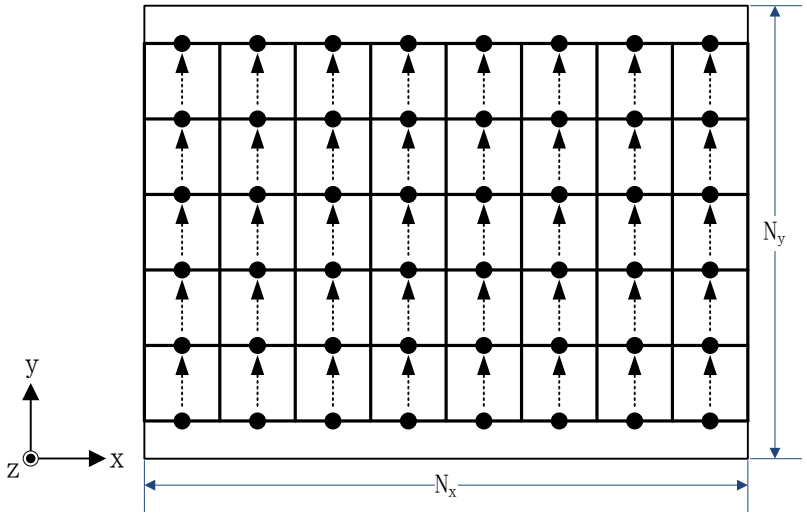

(d) The Y cells.

Figure 3.4 Discretization of the flat metal plate.

3.2.2. Non-Magnetic Plate

a) PEEC Model for Non-Magnetic Plate

Considering the normal component of the induced current on the plate is negligible and the source wires are located in a x-y plane, as shown in Fig. 3.2, the induced current density J and source current Is can be expressed, as follows:

$$\boldsymbol{J} = \boldsymbol{e}_x J_x + \boldsymbol{e}_y J_y \tag{3.2}$$

$$\boldsymbol{I}_s = \boldsymbol{e}_x I_{sx} + \boldsymbol{e}_y I_{sy} \tag{3.3}$$

The corresponding vector potentials are given by:

$$\boldsymbol{A}_c = \boldsymbol{e}_x A_{cx} + \boldsymbol{e}_y A_{cy} \tag{3.4}$$

$$\boldsymbol{A}_s = \boldsymbol{e}_x A_{sx} + \boldsymbol{e}_y A_{sy} \tag{3.5}$$

Using the discritization scheme given in Fig. 3.4, Eq. (3.4-3.5) can be rewrote as:

$$A_{cx,i} = \frac{\mu_0}{4\pi} \sum_{j=1}^{N_{cx}} \left(\int_{l_{x,i}} \int_{v_j'} \frac{1}{R} dv' dl \right) \bullet J_{x,j} \tag{3.6a}$$

$$A_{cy,i} = \frac{\mu_0}{4\pi} \sum_{j=1}^{N_{cy}} \left(\int_{l_{y,i}} \int_{v_j'} \frac{1}{R} dv' dl \right) \bullet J_{y,j} \tag{3.6b}$$

$$A_{sx,i} = \frac{\mu_0}{4\pi} \sum_{j=1}^{N_{sx}} \left(\int_{l_{x,i}} \int_{l_{sx,j}'} \frac{1}{R} dl' dl \right) \bullet I_{sx,j} \tag{3.7a}$$

$$A_{sy,i} = \frac{\mu_0}{4\pi} \sum_{j=1}^{N_{sy}} \left(\int_{l_{y,i}} \int_{l_{sy,j}'} \frac{1}{R} dl' dl \right) \bullet I_{sy,j} \tag{3.7b}$$

Therefore, the KVL equations on all the cell branches derived from Eq. 3.1 are formulated, and grouped into two different sets; one for x-direction currents and one for y-direction currents, as follows:

$$R_{x,i} J_{x,i} + j\omega \sum_{j=1}^{N_{cx}} L_{cx,ij} \bullet J_{x,j} - V_{x,i} = U_{x,i}^s \tag{3.8a}$$

$$R_{y,i} J_{y,i} + j\omega \sum_{j=1}^{N_{cy}} L_{cy,ij} \bullet J_{y,j} - V_{y,i} = U_{y,i}^s \tag{3.8b}$$

where the equivalent partial circuit components are given as:

$$R_{x,i} = \frac{l_{x,i}}{\sigma} \tag{3.9a}$$

$$R_{y,i} = \frac{l_{y,i}}{\sigma} \tag{3.9b}$$

$$L_{cx,ij} = \frac{\mu_0}{4\pi} \int_{l_{x,i}} \int_{v_{cx,j}'} \frac{1}{R} dv' dl \tag{3.9c}$$

$$L_{cy,ij} = \frac{\mu_0}{4\pi} \int_{l_{y,i}} \int_{v_{cy,j}'} \frac{1}{R} dv' dl \tag{3.9d}$$

$$U_{x,i}^s = -\frac{j\omega\mu_0}{4\pi} \sum_{j=1}^{N_{sx}} \left(\int_{l_{x,i}} \int_{l_{sx,j}'} \frac{1}{R} dl' dl \right) \bullet I_{sx,j} \tag{3.9e}$$

$$U_{y,i}^s = -\frac{j\omega\mu_0}{4\pi} \sum_{j=1}^{N_{sy}} \left(\int_{l_{y,i}} \int_{l_{sy,j}'} \frac{1}{R} dl' dl \right) \bullet I_{sy,j} \tag{3.9f}$$

$$V_{x,i} = \varphi_{x,i}^+ - \varphi_{x,i}^- \tag{3.9g}$$

$$V_{y,i} = \varphi^{+}_{y,i} - \varphi^{-}_{y,i} \tag{3.9h}$$

As illustrated in Section 2.5.2, the excited induced current circulates within the plate. For any 4 adjacent current cells, i.e. 2 X cells and 2 Y cells, the continuity of current holds at each potential cell, as shown in Fig. 3.5. The KCL equation for each potential node is expressed as:

$$-J_{x,i}w_{x,i} + J_{x,j}w_{x,j} - J_{y,p}w_{y,p} + J_{y,q}w_{y,q} = 0 \tag{3.10}$$

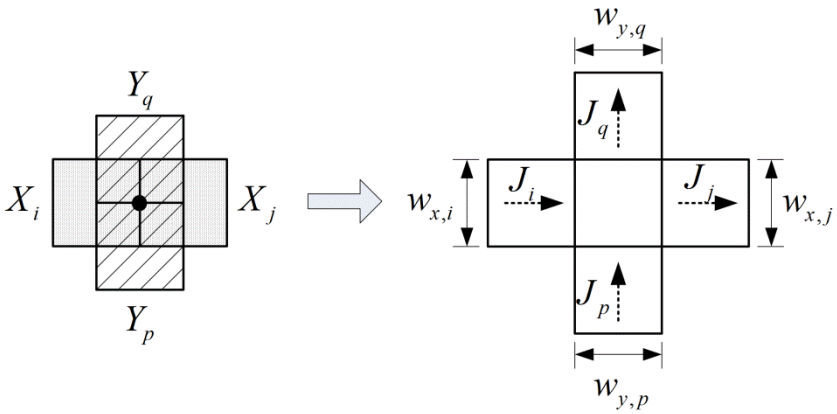

Figure 3.5 The relationship of the adjacent 4 current cells (2 X cells and 2 Y cells).

For the discretization scheme given in Figure 3.4, the incidence matrixes of current cells at the nodes are shown in Figure 3.6. And the incidence matrixes for KVL branches in both x and y direction are shown in Figure 3.7.

$$\begin{array}{r} \\ node:1 \\ 2 \\ 3 \\ \vdots \\ N_x - 1 \\ N_x \end{array} \begin{array}{c} \begin{array}{cccc} J_{x,1} & J_{x,2} & \cdots & J_{x,Nx-1} \end{array} \\ \begin{bmatrix} 1 & & & \\ -1 & 1 & & \\ & -1 & & \\ & & \ddots & \\ & & & 1 \\ & & & -1 \end{bmatrix} \end{array}$$

(a) The incidence matrix for X cells.

$$
\begin{array}{r} \\ node:1 \\ 2 \\ \vdots \\ N_x \\ N_x+1 \\ N_x+2 \\ \vdots \\ 2N_x \end{array}
\begin{array}{c}
\begin{array}{cccc} J_{y,1} & J_{y,2} & \cdots & J_{y,N_x} \end{array} \\
\begin{bmatrix} 1 & & & \\ & 1 & & \\ & & \ddots & \\ & & & 1 \end{bmatrix} \\
\begin{bmatrix} -1 & & & \\ & -1 & & \\ & & \ddots & \\ & & & -1 \end{bmatrix}
\end{array}
$$

(b) The incidence matrix for Y cells.

Figure 3.6 The incidence matrix for current cells at the nodes.

$$
\begin{array}{r} \\ branch\ x:1 \\ 2 \\ \vdots \\ N_x-1 \end{array}
\begin{array}{c}
\begin{array}{ccccc} \varphi_1 & \varphi_2 & \varphi_3 & \varphi_{N_x-1} & \varphi_{N_x} \end{array} \\
\begin{bmatrix} 1 & -1 & & & \\ & 1 & -1 & & \\ & & \ddots & & \\ & & & 1 & -1 \end{bmatrix}
\end{array}
$$

(a) The incidence matrix for branches in x direction.

$$
\begin{array}{r} \\ branch\ y:1 \\ 2 \\ \vdots \\ N_x \end{array}
\begin{array}{c}
\begin{array}{cccc} \varphi_1 & \varphi_2 & \cdots & \varphi_{N_x} \end{array} \\
\begin{bmatrix} 1 & & & \\ & 1 & & \\ & & \ddots & \\ & & & 1 \end{bmatrix}
\end{array}
\begin{array}{c}
\begin{array}{ccccc} \varphi_{N_x+1} & \varphi_{N_x+2} & \cdots & \varphi_{2N_x} \end{array} \\
\begin{bmatrix} -1 & & & \\ & -1 & & \\ & & \ddots & \\ & & & -1 \end{bmatrix}
\end{array}
$$

(b) The incidence matrix for branches in y direction.

Figure 3.7 The incidence matrix for scalar potentials on the branches.

According to the KCL, there must exist the relationship between J_x and J_y:

$$\mathbf{C_x} \bullet \mathbf{J_x} + \mathbf{C_y} \bullet \mathbf{J_y} = 0 \tag{3.11}$$

where $\mathbf{C_x}$ and $\mathbf{C_y}$ reflects the relationship among the branch currents. And the incidence equations for scalar potential are given as follow:

$$\mathbf{C}_y^t \bullet \Phi = \mathbf{V_x}, \quad \mathbf{C}_x^t \bullet \Phi = \mathbf{V_y} \tag{3.12}$$

where $\mathbf{C}_x^t$ and $\mathbf{C}_y^t$ transform the vector of electric scalar potential at nodes to

branch voltage. According to the Eq. (3.8), (3.11) and (3.12), the matrix equation for a plate is obtained as:

$$\begin{bmatrix} \mathbf{R_x} + j\omega\mathbf{L_x} & \mathbf{0} & \mathbf{C}_x^t \\ \mathbf{0} & \mathbf{R_y} + j\omega\mathbf{L_y} & \mathbf{C}_y^t \\ \mathbf{C_x} & \mathbf{C_y} & \mathbf{0} \end{bmatrix} \begin{bmatrix} \mathbf{J_x} \\ \mathbf{J_y} \\ \mathbf{\Phi} \end{bmatrix} = \begin{bmatrix} \mathbf{U_x^s} \\ \mathbf{U_y^s} \\ \mathbf{0} \end{bmatrix} \tag{3.13}$$

The matrix equation (3.13) gives a complete solution structure. Thousands of unknowns in a larger structure can be solved. Note that one potential serves as the reference point, the number of unknowns for the three variables Φ, $\mathrm{J_x}$ and $\mathrm{J_y}$ are $N_V = N_x \bullet N_y - 1$, $N_{cx} = (N_x - 1) \bullet N_y$, $N_{cy} = N_x \bullet (N_y - 1)$. The number of total unknowns in is $N_{tot} = 3N_x \bullet N_y - N_x - N_y - 1$.

b) Numerical Validation

The PEEC model of (3.13) is validated numerically. The configuration for numerical validation is as shown in Figure 3.8. A thin metal plate is investigated in this section, which is made from linear non-magnetic material (aluminum) with the characteristic of conductivity $\sigma = 3.8 \times 10^7 S/m$ and permeability $\mu_r = 1$. The size of the plate is $w = 200mm$, $d = 2mm$. The height of the plate to the current source is $h = 50mm$, and the square wire has a width is $D = 100mm$. The external source here is a filamentary conductor carrying a a.c. current of $I = 1A$. For studying the response from the magnetic field at low frequency, two frequencies ($f = 50Hz$, $1kHz$) in the range are investigated.

Using an uniform meshing scheme of $40 \times 40 \times 4$, the plate is divided into a large number of potential cells. The induced currents are decomposed into two orthogonal components: J_x and J_y, which are the unknowns to be solved. A

line ‘L’ above the plate is selected for evaluating the resultant magnetic field for comparison, as shown in Figure 3.8 (a). Another line at y=0, z=49.25mm inside the plate is selected for the comparison of induced current density J_y, as shown in Fig. 3.9.

The proposed procedure has been implemented in MATLAB. The circuit parameters as well as the resultant magnetic field were calculated. The numerical validation is conducted by comparing these results with those from the software IES-FARADAY based on boundary element method (BEM). As the test problem is small in size it can be easily handled by other methods.

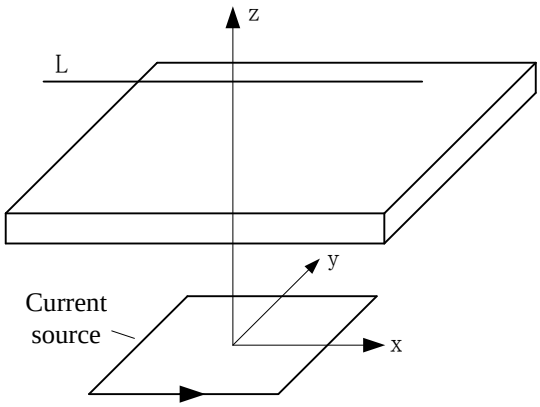

(a) Configuration of a wire-plate structure.

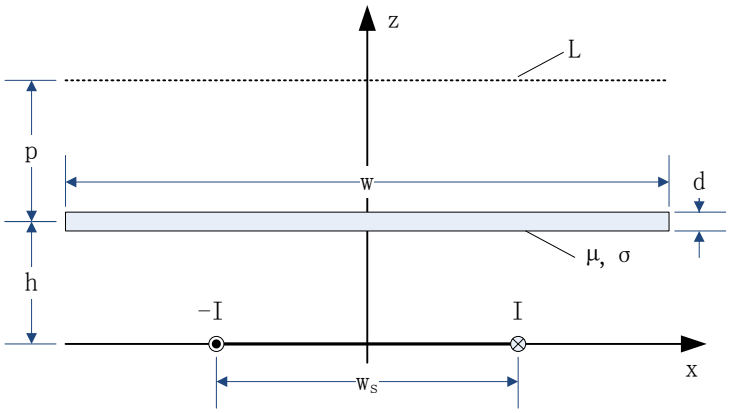

(b)

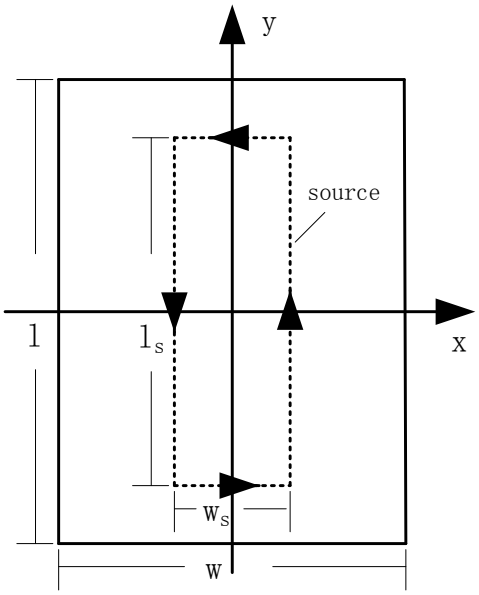

(c)

(b), (c) Section view of the plate and the filamentary conductor.

Figure 3.8 Configuration of a wire-plate structure for testing.

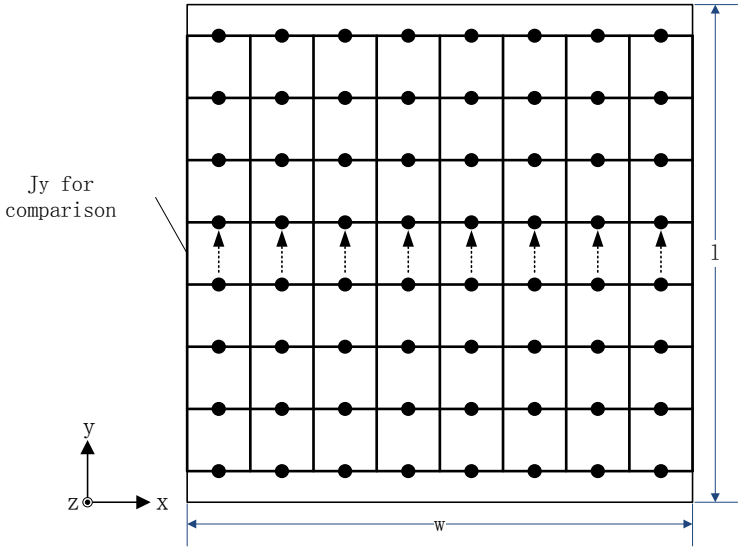

Figure 3.9 The line (y=0, z=49.25mm) on the plate for comparison.

Fig. 3.10 shows the comparison of induced current density J_y on a middle line of the plate. It is shown that the results match well. The deviation among total area is small. The largest deviation exists on the edge area and is just 1% at

50Hz and 1.9% at 1kHz. The average errors of the two frequencies are 0.3% and 0.48%, respectively.

The comparison of the resultant magnetic fields B at 50Hz and 1kHz along a diagonal line above the plate is given in Fig. 3.11. The results also match well . For the component of x direction B_x, there is almost no deviation at 50Hz and a very small deviation of 0.66% at 1kHz. The average errors of the two frequencies are 0.3% and 2%, respectively.

It can be seen that the solutions in presence of non-magnetic material, both the electromagnetic components distributed in the plate and the resultant magnetic field in the space are matched very well with the software. The deviation is very small in most area and increases at the edge area. The error at 50Hz is smaller than at the relatively larger frequency of 1kHz.

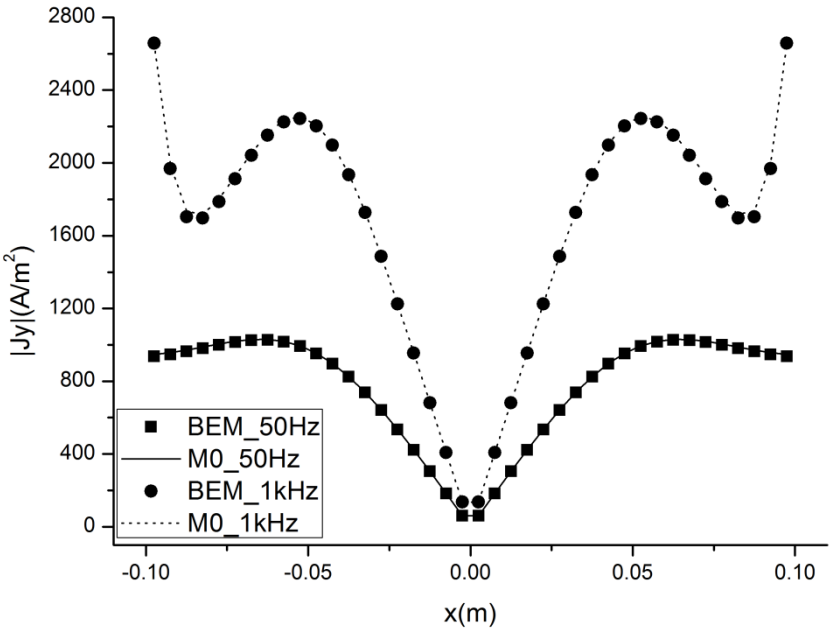

Figure 3.10 Comparison of J_y at the line inside the plate.

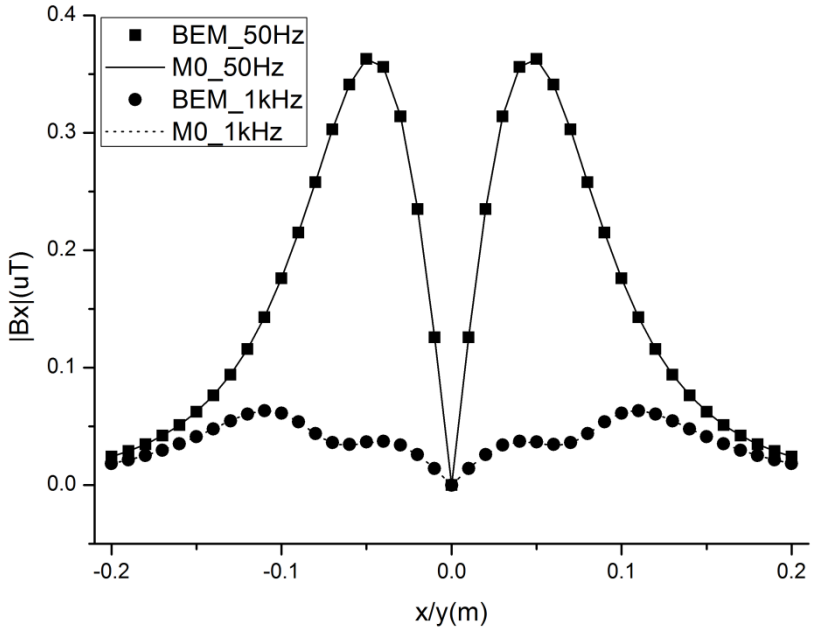

(a) The component of B_x

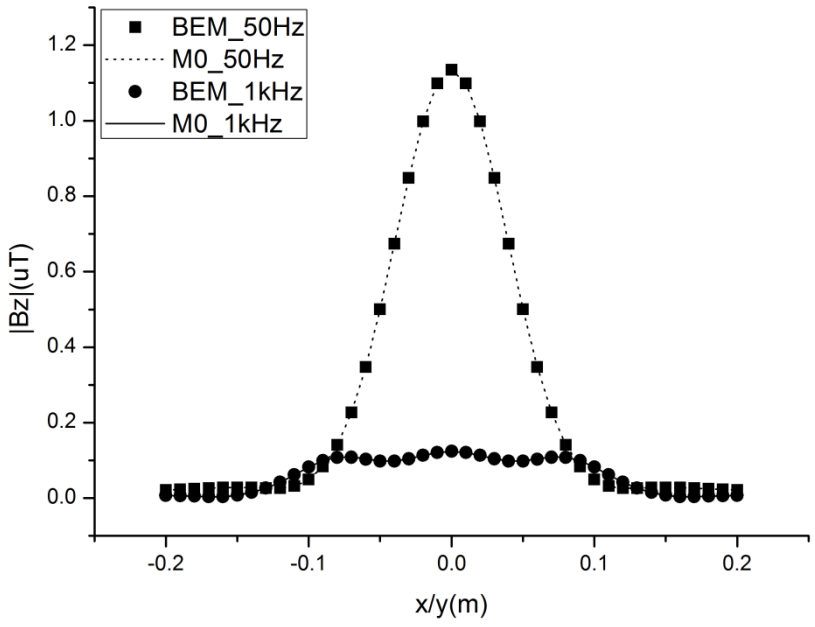

(b) The component of B_z

Figure 3.11 Comparison of B field at a diagonal line above the plate.

3.2.3. Magnetic Plate

a) PEEC Model for Magnetic Plate

When the plate is made of magnetic material, the magnetic polarization needs to be taken into account. In each magnetic cell, the vector quantity of magnetization can be decomposed into three scalar components as follows:

$$\boldsymbol{M} = \boldsymbol{e}_x M_x + \boldsymbol{e}_y M_y + \boldsymbol{e}_z M_z \tag{3.14}$$

The magnetic vector $\boldsymbol{A}_m$ produced by magnetization $\boldsymbol{M}$ is defined as:

$$\boldsymbol{A}_m(\boldsymbol{r}) = \frac{\mu_0}{4\pi}\int_{v'} \boldsymbol{M}(\boldsymbol{r}') \times \nabla' \left(\frac{1}{R}\right) dv' \tag{3.15}$$

where $R = |\boldsymbol{R}| = |\boldsymbol{r} - \boldsymbol{r}'|$. Because of $\nabla = -\nabla'$, there is

$$\nabla' \left(\frac{1}{R}\right) = -\nabla \left(\frac{1}{R}\right) = \frac{\boldsymbol{R}}{R^3} \tag{3.16}$$

Therefore, Eq. (3.15) can be rewritten as

$$\begin{aligned}
\boldsymbol{A}_m(\boldsymbol{r}) &= \frac{\mu_0}{4\pi}\int_{v'} \frac{\boldsymbol{M}(\boldsymbol{r}') \times \boldsymbol{R}}{R^3} dv' \\
&= \frac{\mu_0}{4\pi}\int_{v'} \frac{1}{R^3} [(\boldsymbol{e}_x M_x + \boldsymbol{e}_y M_y + \boldsymbol{e}_z M_z) \times (\boldsymbol{e}_x \Delta x + \boldsymbol{e}_y \Delta y + \boldsymbol{e}_z \Delta z)] dv' \\
&= \boldsymbol{e}_x \frac{\mu_0}{4\pi}\int_{v'} \frac{\Delta z M_y - \Delta y M_z}{R^3} dv' + \\
&\quad \boldsymbol{e}_y \frac{\mu_0}{4\pi}\int_{v'} \frac{\Delta x M_z - \Delta z M_x}{R^3} dv' + \\
&\quad \boldsymbol{e}_z \frac{\mu_0}{4\pi}\int_{v'} \frac{\Delta y M_x - \Delta x M_y}{R^3} dv'
\end{aligned} \tag{3.17}$$

where spatial components $\Delta x = x - x'$, $\Delta y = y - y'$, $\Delta z = z - z'$. And the vector potentials along three orthogonal directions are given by:

$$A_{mx}(r) = \frac{\mu_0}{4\pi}\int_{v'} \frac{\Delta z M_y - \Delta y M_z}{R^3} dv' \tag{3.18a}$$

$$A_{my}(r)=\frac{\mu_0}{4\pi}\int_{v'}\frac{\Delta xM_z-\Delta zM_x}{R^3}dv' \tag{3.18b}$$

$$A_{mz}(r)=\frac{\mu_0}{4\pi}\int_{v'}\frac{\Delta yM_x-\Delta xM_y}{R^3}dv' \tag{3.18c}$$

The Eq. (3.8) can be rewritten into the following equivalent circuit equations with magnetization component being included:

$$\begin{aligned}&R_{x,i}J_{x,i}+j\omega\sum_{j=1}^{N_{cx}}L_{cx,ij}\bullet J_{x,j}+j\omega\sum_{j=1}^{N_{my}}Q_{xy,ij}\bullet M_{y,j}\\&+j\omega\sum_{j=1}^{N_{mz}}Q_{xz,ij}\bullet M_{z,j}-V_{x,i}=U^s_{x,i}\end{aligned} \tag{3.19a}$$

$$\begin{aligned}&R_{y,i}J_{y,i}+j\omega\sum_{j=1}^{N_{cy}}L_{cy,ij}\bullet J_{y,j}+j\omega\sum_{j=1}^{N_{mx}}Q_{yx,ij}\bullet M_{x,j}\\&+j\omega\sum_{j=1}^{N_{mz}}Q_{yz,ij}\bullet M_{z,j}-V_{y,i}=U^s_{y,i}\end{aligned} \tag{3.19b}$$

where the mutual coupling from the magnetization to the current cell are given as:

$$Q_{xy,ij}=\frac{\mu_0}{4\pi}\int_{l_{x,i}}\int_{v_{my,j}'}\frac{\Delta z}{R^3}dv'dl \tag{3.20a}$$

$$Q_{xz,ij}=\frac{\mu_0}{4\pi}\int_{l_{x,i}}\int_{v_{mz,j}'}\frac{-\Delta y}{R^3}dv'dl \tag{3.20b}$$

$$Q_{yx,ij}=\frac{\mu_0}{4\pi}\int_{l_{y,i}}\int_{v_{mz,j}'}\frac{-\Delta z}{R^3}dv'dl \tag{3.20c}$$

$$Q_{yz,ij}=\frac{\mu_0}{4\pi}\int_{l_{y,i}}\int_{v_{mz,j}'}\frac{\Delta x}{R^3}dv'dl \tag{3.20d}$$

Using the relationship $\boldsymbol{B}(\boldsymbol{r})=\nabla\times\boldsymbol{A}(\boldsymbol{r})$ magnetic flux density $\boldsymbol{B}$ can be expressed as follows:

$$\boldsymbol{B}_c(\boldsymbol{r})=\nabla\times\boldsymbol{A}_c(\boldsymbol{r})=\sum_{j=1}^{N_c}\nabla\times\boldsymbol{A}_{c,j}(\boldsymbol{r}) \tag{3.21a}$$

$$\boldsymbol{B}_s(\boldsymbol{r})=\nabla\times\boldsymbol{A}_s(\boldsymbol{r})=\sum_{j=1}^{N_s}\nabla\times\boldsymbol{A}_{s,j}(\boldsymbol{r}) \tag{3.21b}$$

$$\boldsymbol{B}_m(\boldsymbol{r})=\nabla\times\boldsymbol{A}_m(\boldsymbol{r})=\sum_{j=1}^{N_m}\nabla\times\boldsymbol{A}_{m,j}(\boldsymbol{r}) \tag{3.21c}$$

The item $\boldsymbol{B}_c$ is given by:

$$\begin{aligned}
\boldsymbol{B}_c(\boldsymbol{r}) &= \frac{\mu_0}{4\pi}\sum_{j=1}^{N_c}\int_{v'}\nabla\times\frac{\boldsymbol{J}_j(\boldsymbol{r}')}{R}dv' \\
&= \frac{\mu_0}{4\pi}\sum_{j=1}^{N_c}\int_{v'}\nabla(\frac{1}{R})\times\boldsymbol{J}_j(\boldsymbol{r}')dv' \\
&= \frac{\mu_0}{4\pi}\sum_{j=1}^{N_c}\int_{v'}\frac{1}{R^3}[-\boldsymbol{e}_r\times(\boldsymbol{e}_x J_{x,j}+\boldsymbol{e}_y J_{y,j}+\boldsymbol{e}_z J_{z,j})]dv' \\
&= \boldsymbol{e}_x(\frac{\mu_0}{4\pi}\sum_{j=1}^{N_{cz}}\int_{v_{cz,j}'}\frac{-\Delta y}{R^3}dv'\bullet J_{z,j}+\frac{\mu_0}{4\pi}\sum_{j=1}^{N_{cy}}\int_{v_{cy,j}'}\frac{\Delta z}{R^3}dv'\bullet J_{y,j})+ \\
&\quad \boldsymbol{e}_y(\frac{\mu_0}{4\pi}\sum_{j=1}^{N_{cx}}\int_{v_{cx,j}'}\frac{-\Delta z}{R^3}dv'\bullet J_{x,j}+\frac{\mu_0}{4\pi}\sum_{j=1}^{N_{cz}}\int_{v_{cz,j}'}\frac{\Delta x}{R^3}dv'\bullet J_{z,j})+ \\
&\quad \boldsymbol{e}_z(\frac{\mu_0}{4\pi}\sum_{j=1}^{N_{cy}}\int_{v_{cy,j}'}\frac{-\Delta x}{R^3}dv'\bullet J_{y,j}+\frac{\mu_0}{4\pi}\sum_{j=1}^{N_{cx}}\int_{v_{cx,j}'}\frac{\Delta y}{R^3}dv'\bullet J_{x,j})
\end{aligned} \tag{3.22}$$

Considering the structure in this study, Eq. (3.22) can be decomposed as follows:

$$B_{xy}(r)=\frac{\mu_0}{4\pi}\sum_{j=1}^{N_{cy}}\int_{v_{cy,j}'}\frac{\Delta z}{R^3}dv'\bullet J_{y,j} \tag{3.23a}$$

$$B_{yx}(r)=\frac{\mu_0}{4\pi}\sum_{j=1}^{N_{cx}}\int_{v_{cx,j}'}\frac{-\Delta z}{R^3}dv'\bullet J_{x,j} \tag{3.23b}$$

$$B_{zx}(r)=\frac{\mu_0}{4\pi}\sum_{j=1}^{N_{cx}}\int_{v_{cx,j}'}\frac{\Delta y}{R^3}dv'\bullet J_{x,j} \tag{3.23c}$$

$$B_{zy}(r)=\frac{\mu_0}{4\pi}\sum_{j=1}^{N_{cy}}\int_{v_{cy,j}'}\frac{-\Delta x}{R^3}dv'\bullet J_{y,j} \tag{3.23d}$$

Similarly, $\boldsymbol{B}_s$ contributed by source current in this case is given by:

$$B_{sx}(r)=\frac{\mu_0}{4\pi}\sum_{j=1}^{N_{sy}}\int_{l_{y,j}'}\frac{\Delta z}{R^3}dl'\bullet I_{y,j} \tag{3.24a}$$

$$B_{sy}(r)=\frac{\mu_0}{4\pi}\sum_{j=1}^{N_{sx}}\int_{l_{x,j}'}\frac{-\Delta z}{R^3}dl'\bullet I_{x,j} \tag{3.24b}$$

$$B_{sz}(r)=\frac{\mu_0}{4\pi}\sum_{j=1}^{N_{sx}}\int_{l_{x,j}'}\frac{\Delta y}{R^3}dl'\bullet I_{x,j}+\frac{\mu_0}{4\pi}\sum_{j=1}^{N_{sy}}\int_{l_{y,j}'}\frac{-\Delta x}{R^3}dl'\bullet I_{y,j} \tag{3.24c}$$

$\boldsymbol{B}_m$ is contributed by magnetization M via mutual coupling coefficients. It is expressed by:

$$\boldsymbol{B}_m(\boldsymbol{r}) = \frac{\mu_0}{4\pi}\sum_{j=1}^{N_m}\int_{v'}\nabla\times[-\boldsymbol{M}_j(\boldsymbol{r}')\times\nabla(\frac{1}{R})]dv' \tag{3.25}$$

Using the vector identity and considering the uniform distribution:

$$\nabla\times(\boldsymbol{A}\times\boldsymbol{B}) = \boldsymbol{A}\nabla\bullet\boldsymbol{B} - \boldsymbol{B}\nabla\bullet\boldsymbol{A} + (\boldsymbol{B}\bullet\nabla)\boldsymbol{A} - (\boldsymbol{A}\bullet\nabla)\boldsymbol{B} \tag{3.26}$$

There is:

$$\begin{aligned}\boldsymbol{B}_m(\boldsymbol{r}) = &-\frac{\mu_0}{4\pi}\sum_{j=1}^{N_m}\int_{v'}[\boldsymbol{M}_j(\boldsymbol{r}')\nabla\bullet\nabla(\frac{1}{R}) - \nabla(\frac{1}{R})\nabla\bullet\boldsymbol{M}_j(\boldsymbol{r}')\\ &+(\nabla(\frac{1}{R})\bullet\nabla)\boldsymbol{M}_j(\boldsymbol{r}') - (\boldsymbol{M}_j(\boldsymbol{r}')\bullet\nabla)\nabla(\frac{1}{R})]dv'\\ =&\frac{\mu_0}{4\pi}\sum_{j=1}^{N_m}\int_{v'}[(\boldsymbol{M}_j(\boldsymbol{r}')\bullet\nabla)\nabla(\frac{1}{R})]dv'\end{aligned} \tag{3.27}$$

As a result, vector $\boldsymbol{B}_m$ can be decomposed to three scalar components, as follow:

$$\begin{aligned}B_{mx} = &\frac{\mu_0}{4\pi}[\sum_{j=1}^{N_{mx}}\int_{v'}(\frac{3\Delta x^2}{R^5} - \frac{1}{R^3})dv'\bullet M_{x,j}\\ &+\sum_{j=1}^{N_{my}}\int_{v'}\frac{3\Delta x\Delta y}{R^5}dv'\bullet M_{y,j} + \sum_{j=1}^{N_{mz}}\int_{v'}\frac{3\Delta x\Delta z}{R^5}dv'\bullet M_{z,j}]\end{aligned} \tag{3.28a}$$

$$\begin{aligned}B_{my} = &\frac{\mu_0}{4\pi}[\sum_{j=1}^{N_{mx}}\int_{v'}\frac{3\Delta y\Delta x}{R^5}dv'\bullet M_{x,j}\\ &+\sum_{j=1}^{N_{my}}\int_{v'}(\frac{3\Delta y^2}{R^5} - \frac{1}{R^3})dv'\bullet M_{y,j} + \sum_{j=1}^{N_{mz}}\int_{v'}\frac{3\Delta y\Delta z}{R^5}dv'\bullet M_{z,j}]\end{aligned} \tag{3.28b}$$

$$\begin{aligned}B_{mz} = &\frac{\mu_0}{4\pi}[\sum_{j=1}^{N_{mx}}\int_{v'}\frac{3\Delta z\Delta x}{R^5}dv'\bullet M_{x,j}\\ &+\sum_{j=1}^{N_{my}}\int_{v'}\frac{3\Delta z\Delta y}{R^5}dv'\bullet M_{y,j} + \sum_{j=1}^{N_{mz}}\int_{v'}(\frac{3\Delta z^2}{R^5} - \frac{1}{R^3})dv'\bullet M_{z,j}]\end{aligned} \tag{3.28c}$$

The solution matrix can be then set up as follow:

$$\begin{bmatrix} \mathbf{L_x} & \mathbf{0} & \mathbf{C}_x^t & \mathbf{Q_x} \\ \mathbf{0} & \mathbf{L_y} & \mathbf{C}_y^t & \mathbf{Q_y} \\ \mathbf{C_x} & \mathbf{C_y} & \mathbf{0} & \mathbf{0} \\ \mathbf{T_x} & \mathbf{T_y} & \mathbf{0} & \mathbf{P} \end{bmatrix} \begin{bmatrix} \mathbf{J_x} \\ \mathbf{J_y} \\ \mathbf{\Phi} \\ \mathbf{M} \end{bmatrix} = \begin{bmatrix} \mathbf{U_x^s} \\ \mathbf{U_y^s} \\ \mathbf{0} \\ \mathbf{B_s} \end{bmatrix} \tag{3.29}$$

where $\mathbf{\Phi}$ and $\mathbf{M}$ are respectively the potential and magnetization density at nodes, $\mathbf{U^s}$ and $\mathbf{B_s}$ are the inductive voltage and magnetic field contributed by the current source. Both $\mathbf{C_x}$ and $\mathbf{C_y}$ are the nodal incidence matrices for X and Y current cells. Assuming $\hat{u}_{ij}$ is zero if $i \neq j$ and $\hat{u}_{ij}$ is one if $i = j$, elements in sub-matrix of [16] are given by:

$$\mathrm{L_{ij}} = \frac{l_i}{\sigma}\hat{u}_{ij} + \frac{j\omega\mu_0}{4\pi}\int_{l_i}\int_{v_j'}\frac{1}{|r_i - r_j'|}dv'dl \tag{3.30a}$$

$$\mathrm{Q_{ij}} = \frac{j\omega\mu_0}{4\pi}\int_{l_i}\int_{v_j'}\frac{\hat{b}(r_j')\times(r_i - r_j')}{|r_i - r_j'|^3}dv'dl \tag{3.30b}$$

$$\mathrm{T_{ij}} = \frac{\mu_0}{4\pi}\int_{v_j'}\frac{\nabla\times f(r_j')}{|r_i - r_j'|}dv' \tag{3.30c}$$

$$\mathrm{P_{ij}} = \frac{\mu_0}{4\pi}\int_{v_j'}\frac{\nabla\times(\hat{b}(r_j')\times(r_i - r_j'))}{|r_i - r_j'|^3}dv' - \frac{\mu_0 \bullet \mu_r}{\mu_r - 1}\hat{u}_{ij} \tag{3.30d}$$

$$\mathrm{U_{s,i}} = \frac{j\omega\mu_0}{4\pi}\sum_{j=1}^{N_s}\int_{l_i}\int_{l_j'}\frac{I_{s,j}}{|r_i - r_j'|}dl'dl \tag{3.30e}$$

$$\mathrm{B_{s,i}} = \frac{\mu_0}{4\pi}\sum_{j=1}^{N_s}\int_{l_j'}\frac{\nabla\times I_{s,j}}{|r_i - r_j'|}dl' \tag{3.30f}$$

where $\hat{b}(r)$ and $f(r)$ represent the unit vector for $\boldsymbol{M}(r)$ and $\boldsymbol{J}(r)$, respectively. Excluding the reference node, the number of total unknowns in is equal to $6N_xN_y - N_x - N_y - 1$.

b) Numerical Validation

The PEEC model of Eq. (3.29) is validated numerically. The numerical

validation is conducted by comparing these results with those from the software IES-FARADAY based on BEM. The test problem will be small in size, and therefore easily handled by the other methods.

The structure under investigation is as shown in Fig. 3.8. The thin plate is made from linear magnetic materials with the conductivity of $\sigma = 0.75\times10^7 S/m$ and permeability of $\mu_r = 200$. The filamentary wire carrying a a.c. current $I = 1A$ at the frequency $f = 50Hz$. The dimensions of the structure are: w=200mm, d=2mm, h=50mm. A uniform mesh of $40\times40\times4$ ($N_x = 40$, $N_y = 40$) is adopted.

The proposed procedure (PM) has been implemented in MATLAB. For comparison the results computed by the boundary-element method-based (BEM) software IES-FARADAY are presented in the figure as well. Fig. 3.12 shows the eddy current and magnetization density J_y and M_x in the middle line on the bottom of the plate. It can be seen that the results are matched well in most area, a little deviation exist in the area near to edge and the maximum errors are 4.13% and 3.37%, respectively. The two components of resultant magnetic flux density B along a diagonal line above the plate are presented in Figure 3.13, the results matched very well and the maximum error is 2.4%.

In this section, due to the magnetic material involved, the EFIE and magnetic equation are integrated as a complete set of equations to solve the eddy current and magnetization in the plate and magnetic field around the plate. The proposed numerical procedure has been validated and compared with the BEM-based software IES-FARADAY, the results indicated the approach has a fairly good accuracy in evaluating low frequency magnetic shielding.

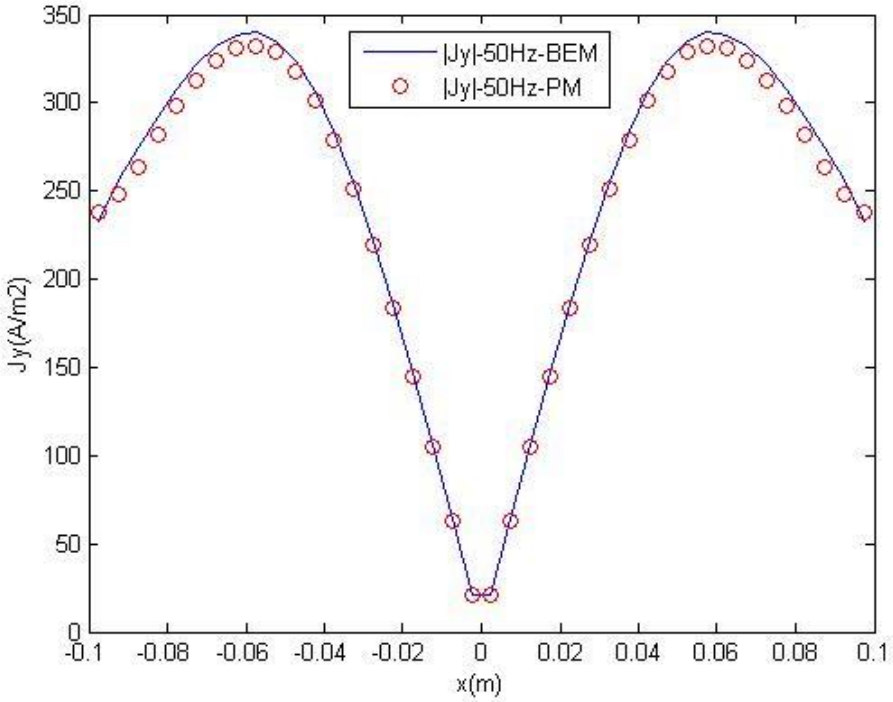

(a) J_y

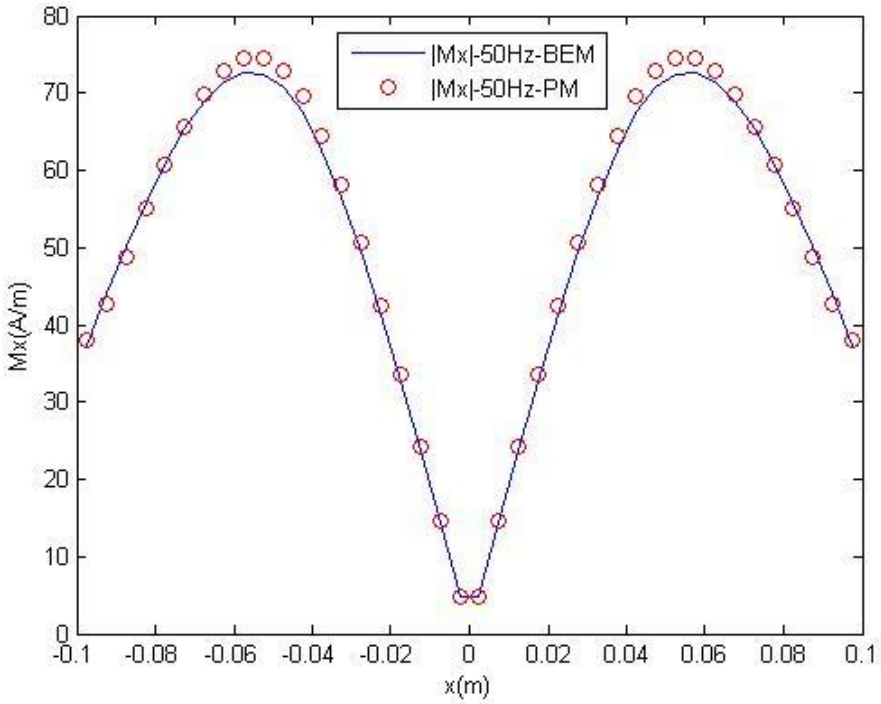

(b) M_x

Figure 3.12 Comparison of EM components at a line on the bottom of the plate.

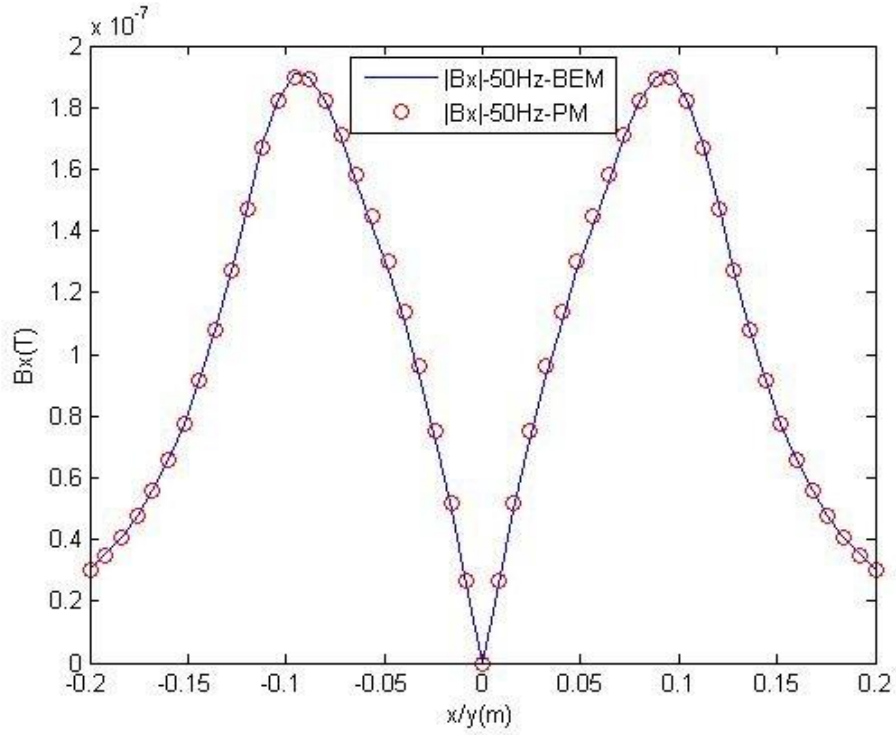

(a) B_x

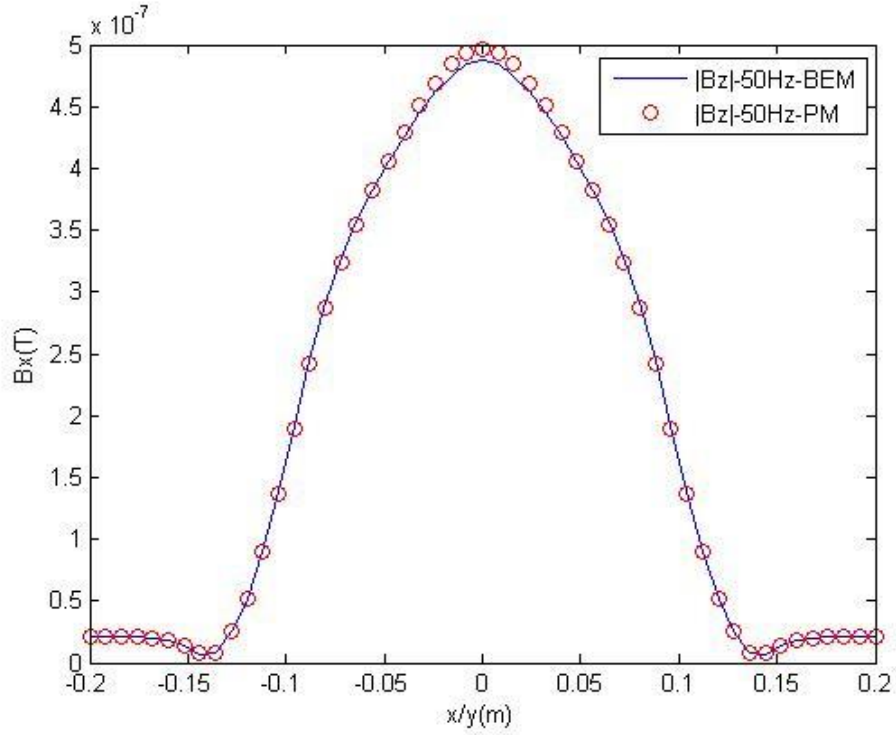

(b) B_z

Figure 3.13 Comparison of B field at a diagonal line above the plate (z=100mm).

3.3. 2D PEEC Model for Metal Plate

3.3.1. 2D PEEC Formulations

Green's theorem is one of the most useful theorems in solving electromagnetic problems. Many of the solution methods, including classical and numerical methods, are based on Green's theorem. It is derived directly from the divergence theorem.

In a free space, Green's function is a response function relating the field point ($\boldsymbol{r}$) and the source point ($\boldsymbol{r}'$), and it is the fundamental solution of the same operator equation. The free space Green's function in a 2D case is given as:

$$G(\boldsymbol{r},\boldsymbol{r}') = \frac{1}{2\pi}\ln\frac{1}{|\boldsymbol{r}-\boldsymbol{r}'|} \tag{3.31}$$

Then, the vector potentials $\boldsymbol{A}_c$ and $\boldsymbol{A}_s$, produced by induced current and external current sources respectively, are given as follows:

$$\boldsymbol{A}_c(\boldsymbol{r}) = \frac{\mu_0}{2\pi}\int_{S'}\ln\frac{1}{R}\bullet\boldsymbol{J}_c(\boldsymbol{r}')dS' \tag{3.32}$$

$$\boldsymbol{A}_s(\boldsymbol{r}) = \frac{\mu_0}{2\pi}\ln\frac{1}{R}\bullet\boldsymbol{I}_s(\boldsymbol{r}') \tag{3.33}$$

where $R = |\boldsymbol{R}| = |\boldsymbol{r}-\boldsymbol{r}'|$, $\boldsymbol{J}_c$, $\boldsymbol{I}_s$ represent the induced current density and external sources current, respectively. The induced eddy current circulates in the plate plane, and vertically through the cross-section, as seen in Fig. 2.8.

If the magnetic material is involved, the vector potential $\boldsymbol{A}_m$ produced by magnetic polarization is given as follow:

$$\boldsymbol{A}_m(\boldsymbol{r}) = \frac{\mu_0}{2\pi}\int_{S'}\boldsymbol{M}(\boldsymbol{r}')\times\nabla'\left(\frac{1}{R}\right)dS' \tag{3.34}$$

where $\boldsymbol{M}$ is magnetization density, ∇' is nabla operator.

3.3.2. 2D PEEC Model

Some of shielding structures can be simplified, and represented by 2D models if the variation in one dimension is not significant. The unknowns will be reduced sharply and the complexity of the model would be lowered greatly. Therefore, the efficiency and applicability of the models will be improved significantly.

The 2D plate is discretized into a number of 2D rectangular cells, which are defined potential cells. With the assumption that the electromagnetic components in a cell are constant, the 2D model can be established. For ferromagnetic materials, the magnetic density inside the plate should be solved.

This section presents an approach for evaluating eddy currents at low frequency in presence of a 2D magnetic plate. The plate is divided into a number of 2D rectangular cells, which are defined potential cells. The eddy current is solved with the constitutive relation in a magnetic material. The resultant magnetic field can be calculated with the Biot-Savart law. This method uses few unknown variables, and requires less computer resource. The proposed method has been applied to evaluate the eddy-current in the metal plates with different kinds of magnetic material.

The plate of concern is made from linear magnetic material. It is characterized by conductivity σ and permeability μ, and has a width of w and a thickness of d illustrated in Figure. 3.14. It is noted that the thickness of the plate is much less than its relevant characteristic width. The normal component of the current

density within a plate is thus considered to negligible in a quasi-stationary field problem. According to Maxwell's equations, the plate can be substituted by a non-magnetic plate carrying an equivalent magnetic current of $\nabla \times M$. For efficient calculation magnetization vector *M* instead of the equivalent current is introduced as the unknown variable together with conductive current density J_c.

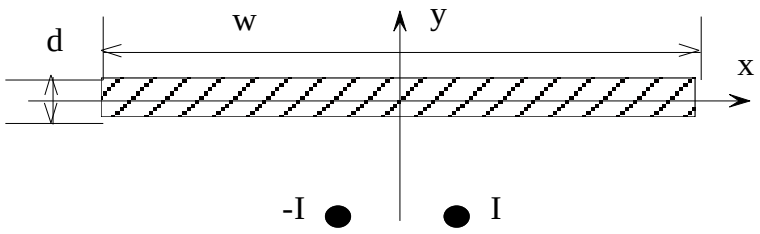

Figure 3.14 Configuration of a magnetic plate in 2D domain.

To solve unknown conductive and magnetization currents numerically, the plate has to be meshed into small rectangular cells (e.g., N segments along X direction and M segments along Y direction). Using the relationship for electrical scalar potential and magnetic vector potential $E + j\omega A = -\nabla\phi$, a voltage equation can be established for each cell along its length. The magnetic vector potential *A* is contributed by three items: external source current *I*, the eddy current J_c, and equivalent magnetic current $\nabla \times M$. Voltage *V* per unit along z direction in a cell is expressed as follows:

$$\begin{aligned} V_i = \quad & \frac{J_{ci}}{\sigma} + j\omega \sum_{j=1}^{N_s} \frac{\mu_0}{2\pi} \ln \frac{1}{|r - r'|} I_j + j\omega \sum_{j=1}^{N} \frac{\mu_0}{2\pi} \int_{S_j} \ln \frac{1}{|r - r'|} J_{cj}(y')\, ds' + \\ & j\omega \sum_{j=1}^{N} \frac{\mu_0}{2\pi} \int_{S_j} \frac{(y - y')}{(r - r')^2} M_{xj}(y')\, ds' + j\omega \sum_{j=1}^{M} \frac{\mu_0}{2\pi} \int_{S_j} \frac{-(x - x')}{(r - r')^2} M_{yj}(x')\, ds' \end{aligned} \tag{3.35}$$

where N_s is the number of external source lines, *i* and *j* are the index for observation and source cells, respectively. For the linear magnetic material both

M_x and M_y can be expressed in terms of J_c and I using the constitutive relation, $M = \chi_m \bullet H$ where $\chi_m = \mu_r - 1$. With this equation, current density J_c can be directly obtained. Subsequently, the magnetic field in or around plate can be calculated using the Bio-Savart law.

In the equation $B = \nabla \times A(r,t)$, the vector potential A contains three items: A_s, A_c and A_m. There items are respectively generated by external source current I, eddy current J_c, and equivalent magnetic current $\nabla \times M$ respectively. So the equation can be substituted by $B = \nabla \times (A_s + A_c + A_m)$, which is decoupled into two orthogonal equations, as follows:

$$\begin{aligned} B_i(x) = & \sum_{j=1}^{N_s} \frac{\mu_0}{2\pi} \frac{-(y-y')}{(r-r')^2} I_j + \sum_{j=1}^{N} \frac{\mu_0}{2\pi} \int_{S_j} \frac{-(y-y')}{(r-r')^2} J_{cj}(y')\,ds' + \\ & \sum_{j=1}^{N} \frac{\mu_0}{2\pi} \int_{S_j} \frac{(x-x')^2 - (y-y')^2}{(r-r')^4} M_{xj}(y')\,ds' \\ & + \sum_{j=1}^{M} \frac{\mu_0}{2\pi} \int_{S_j} \frac{2(x-x')(y-y')}{(r-r')^4} M_{yj}(x')\,ds' \end{aligned} \tag{3.36a}$$

$$\begin{aligned} B_i(y) = & \sum_{j=1}^{N_s} \frac{\mu_0}{2\pi} \frac{(x-x')}{(r-r')^2} I_j + \sum_{j=1}^{N} \frac{\mu_0}{2\pi} \int_{S_j} \frac{(x-x')}{(r-r')^2} J_{cj}(y')\,ds' \\ & + \sum_{j=1}^{N} \frac{\mu_0}{2\pi} \int_{S_j} \frac{2(x-x')(y-y')}{(r-r')^4} M_{xj}(y')\,ds' \\ & + \sum_{j=1}^{M} \frac{\mu_0}{2\pi} \int_{S_j} \frac{(y-y')^2 - (x-x')^2}{(r-r')^4} M_{yj}(x')\,ds' \end{aligned} \tag{3.36b}$$

These are the expressions for the x and y components of the magnetic field respectively.

Intuitively, the plate is meshed uniformly, and assuming that the current density J_c, magnetization vector M in every cell are constant. Note that both the codncutive and magnetization currents vary significantly along its width and

thickness, meshing with small cells is required. Fig. 3.15 illustrates a typical grid generation.

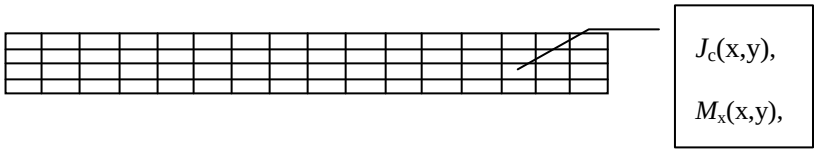

Figure 3.15 Two-dimensional meshing of a magnetic plate

Based on the Equations (3.35) and (3.36), such a system can be expressed in the following matrix equation form:

$$[[G11]+K_e \bullet E_{N\times M}][J_c]+[G12][M_x]+[G13][M_y]=[S] \tag{3.37a}$$

$$[G21][J_c]+[[G22]-K_m \bullet E_{N\times M}][M_x]+[G23][M_y]=[B_{xs}] \tag{3.37b}$$

$$[G31][J_c]+[G32][M_x]+[[G33]-K_m \bullet E_{N\times M}][M_y]=[B_{ys}] \tag{3.37c}$$

where $K_e=1/\sigma$, $K_m=\mu_0\mu_r/(\mu_r -1)$, and [S], [$B_{xs}$] and [$B_{ys}$] are column vectors of ($N\times M$) order whose elements are defined by

$$S_i = -j\omega\sum_{j=1}^{N_s}\frac{\mu_0}{2\pi}\ln\frac{1}{|r-r'|}I_j \tag{3.38}$$

$$B_{xsi} = -\sum_{j=1}^{N_s}\frac{\mu_0}{2\pi}\frac{-(y-y')}{(r-r')^2}I_j \tag{3.39a}$$

$$B_{ysi} = -\sum_{j=1}^{N_s}\frac{\mu_0}{2\pi}\frac{(x-x')}{(r-r')^2}I_j \tag{3.39b}$$

and [G11], [G12], [G13], [G21], [G22], [G23], [G31], [G32], [G33] are square matrices of (($N\times M$) $\times$($N\times M$)) order given by

$$G11_{ij} = j\omega\sum_{j=1}^{N}\frac{\mu_0}{2\pi}\int_{S_j}\ln\frac{1}{|r-r'|}J_{cj}(y')ds' \tag{3.40a}$$

$$\mathrm{G12_{ij}} = j\omega\sum_{j=1}^{N}\frac{\mu_0}{2\pi}\int_{S_j}\frac{(y-y')}{(r-r')^2}M_{xj}(y')ds' \tag{3.40b}$$

$$G13_{ij} = j\omega\sum_{j=1}^{M}\frac{\mu_0}{2\pi}\int_{S_j}\frac{-(x-x')}{(r-r')^2}M_{yj}(x')ds' \tag{3.40c}$$

$$G22_{ij} = \sum_{j=1}^{N}\frac{\mu_0}{2\pi}\int_{S_j}\frac{(x-x')^2-(y-y')^2}{(r-r')^4}M_{xj}(y')ds' \tag{3.40d}$$

$$G23_{ij} = \sum_{j=1}^{M}\frac{\mu_0}{2\pi}\int_{S_j}\frac{2(x-x')(y-y')}{(r-r')^4}M_{yj}(x')ds' \tag{3.40e}$$

$G21_{ij} = -G12_{ij}$, $G31_{ij} = -G13_{ij}$, $G32_{ij} = G23_{ij}$, $G33_{ij} = -G22_{ij}$.

Numerical validation was conducted on the plate (*w*=400mm, *d*=2mm) shown in Fig. 3.9. The 8eddy current along the bottom edge of the magnetic plate is calculated using the proposed method (one-dimensional meshing method) and a boundary element method. Three cases with different frequency and material parameters were considered, that is, f=50Hz, μ_r=200, f=50Hz, μ_r=10000and (3) f=5000Hz, μ_r=200. It is noted that the calculated results agree well in these cases, as seen in Fig. 3.16.

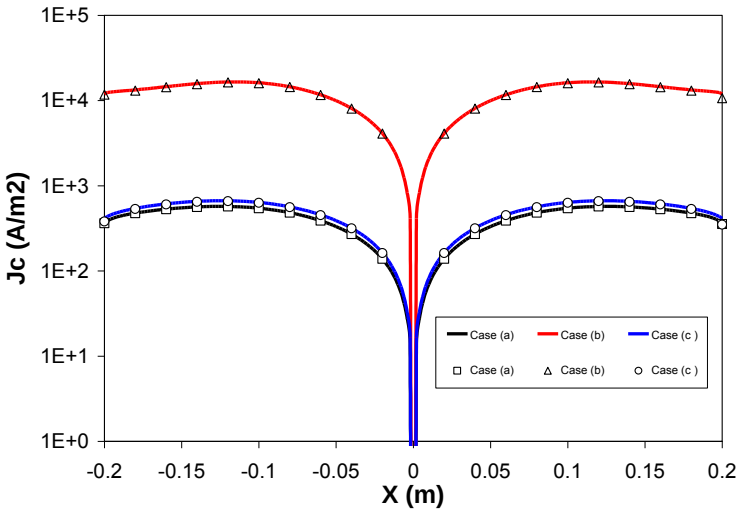

Figure 3.16 Current density in the plate (lines = proposed method, dots = BEM)

Different meshing methods are also compared numerically using the same plate shown above. The plate has the width of 400mm and the thickness of 2mm. It has

the permeability μ_r of 200, and the conductivity $\sigma=0.75\times10^7$. The frequency of source current f is set to be 50Hz.

When using the one-dimensional meshing method, the plate is divided into 100×4 cells. Every cell has the equal size. Assuming that the current density J_c, magnetization vector M within the area of each cell are constant, and as same as the characteristic value at the middle point of this cell. The curve of J_c and M_x along the bottom of plate are shown as Fig. 3.17 and Fig. 3.18 respectively.

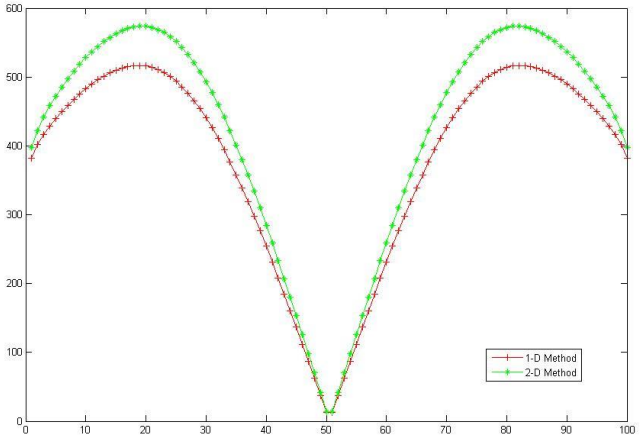

Figure 3.17 Current density J_c on the bottom of the plate.

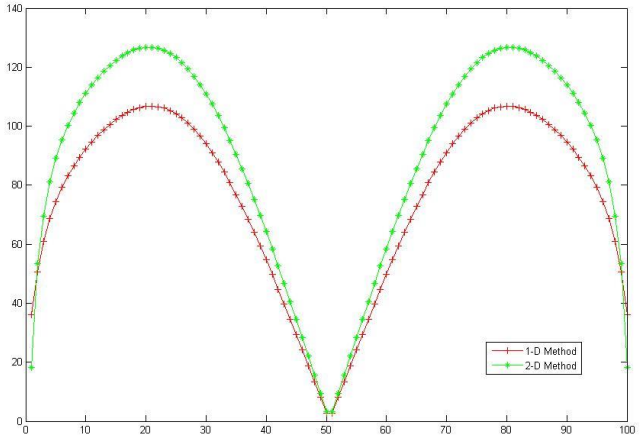

Figure 3.18 Magnetization M_x on the bottom of the plate.

3.4. Conclusion

In this Chapter, the classic PEEC method (named “M0”) based on the uniform distribution of EM components in the cell is provided. Both non-magnetic and magnetic materials have been considered for investigation. In non-magnetic plates, the solutions of both induced current and the resultant magnetic field around the plate can be obtained easily. In magnetic plates, the magnetizing current needs to be taken into account. The 3D and 2D PEEC models all have been established and discussed.

The proposed approach was validated numerically. The high accurate results can be obtained when there is a high density of grid. Unfortunately, because of the big effort for discretization and the high number of unknowns this approach is not practicable in many cases. Due to the significant variation of EM components inside the metal plate, the dense grid is required and the method is hard to model large structures. How to solve the large complex structures with huge number of unknowns more quickly is very useful and valuable.

4. PEEC Model Using Analytic Distribution Functions

Generally speaking, a denser meshing scheme yields a higher accuracy of the simulation results. This, however, increases the number of unknowns in the matrix equation significantly. It would not be possible to solve such a big problem with limited capacities of the computing facilities available. Therefore, it is necessary to develop appropriate meshing schemes so that the number of unknowns in the matrix equation is reduced dramatically, and shielding problems can be solved efficiently.

This chapter presents an extended PEEC modeling procedure. In this procedure an analytical expression using the double exponential function is applied to describe the variation of both induced current and magnetization densities. With this approximation the discretization over the cross section of the plate is avoided and a new method (named “M1”) is proposed, where the number of unknowns is reduced significantly and the accuracy generally retains. In addition, non-uniform meshing is assigned for the part on a plate corresponding to the location of external current sources. The refinement is particularly done in the edge area for improving the accuracy of solutions. An improved method (named “IM1”) is also presented for the non-magnetic thin plate. Numerical validation of the proposed procedure using the commercial FEM package is presented finally.

4.1. Skin Effect in PEEC Models

4.1.1. Cross-Sectional Discretization

As mentioned in Section 3.1, the assumption of a uniform current distribution is only correct where the skin depth $\delta = \sqrt{2/\omega\mu_0\sigma}$ is greater than half of the cross-sectional dimensions. Fig. 2.6 shows the PEEC adequate solution for considering the skin effect is the finer cross-sectional segmentation in cells so that the current is uniformly distributed in each of them. This approach has been implemented in Chapter 3. In this way, both the skin effect and the proximity effect can be taken into account simultaneously. Unfortunately, because of the greater effort for discretization and the higher number of unknowns this approach is not practicable in many cases. Numerical calculations show that a relatively high number of cells for the cross-sectional discretization is needed to obtain accurate results (e.g. (Coperich, K. M. et al. 2000, Wollenberg, G et al. 2003)).

In a traditional PEEC model, the unknowns such as current and magnetization densities in a volume cell are considered to be constant. Discretization is then made along x, y and z directions, as seen in Fig. 3.3. When these densities vary significantly across plate thickness, a denser grid is required in order to retain the accuracy of simulation results. The total number of unknowns for a large plate is then significantly high. If some analytical functions are available for the distribution of unknown parameters along plate thickness, discretization along thickness becomes unnecessary. In this case, a surface discreitzation scheme

would be sufficient for solving the problem.

4.1.2. Analytical Function Based on the Skin Effect

In probability theory and statistics, the double exponential distribution is a continuous probability distribution, because it can be thought of as two exponential distributions (with an additional location parameter) spliced together back-to-back.

The implementation of the skin effect in PEEC model by introduction of an analytical expression of double exponential distribution has been revealed in (N. Ida 1995), that the current density in an infinite plate which is perpendicular to the z axis. The aim of this is to reduce the number of unknown currents for representation of the elements on the cross section (C.V. Dodd and W.E. Deeds 1968). If the current density varies with the z direction, it is given by, as shown as follow

$$J(z) = J_1 e^{\alpha z} + J_2 e^{-\alpha z} \tag{4.1}$$

where $\alpha = -(1+j)/\delta$, and the skin depth of the plate is $\delta = \sqrt{2/\omega\mu_0\sigma}$. Both J_1 and J_2 in Eq. (4.1) are two unknowns to be determined. The eddy current in a current cell is similar to that in such an infinite plate. This analytical expression is adopted to describe the current density within the cell to avoid the discretization along the plate thickness. As shown in Fig. 4.1, in traditional discretization, the plate needs be segmentalized along the thickness when the skin depth is less than half of the cross-sectional dimension. When the analytical expression is applied, this segmentation is avoided and the number of unknowns

is reduced from *Nz* to just 2. In a current cell i the function $J_i(z)$ in Eq. (4.1) can be rewritten in terms of current densities J_i^- and J_i^+ on both the bottom and top surfaces of the cell, respectively. The current density in the cell can be approximated by a double exponential function, as follow:

$$J_i(z) = \frac{J_i^- sh(\alpha(d/2 - z)) + J_i^+ sh(\alpha(d/2 + z))}{sh(\alpha d)} \tag{4.2}$$

where *d* is the thickness of the plate. In Eq. (4.2) superscripts "+" and "-" denote the top and bottom surfaces of a cell, respectively. This expression is applicable to any orientation of an external magnetic field.

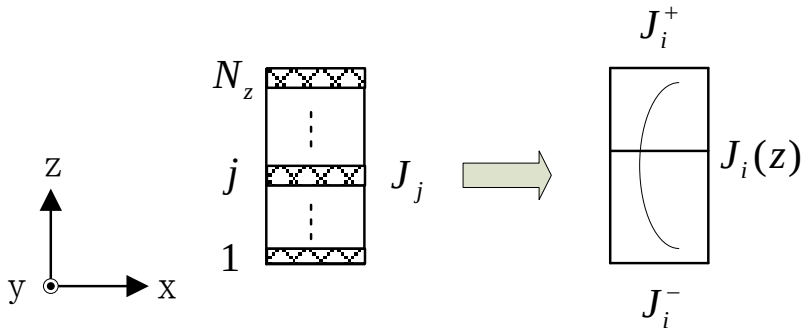

Figure 4.1 The analytical expression is adopted within the cell.

Similarly, the magnetization $\boldsymbol{M}$ can be expressed analytically as follow:

$$M_i(z) = \frac{M_i^- sh(\alpha(d/2 - z)) + M_i^+ sh(\alpha(d/2 + z))}{sh(\alpha d)} \tag{4.3}$$

Using such a distribution expression, division for magnetization along the thickness of the plate is also avoided and the unknowns can be reduced sharply.

4.1.3. Numerical Investigation

In this section, the hypothesis of double exponential distribution of the electromagnetic components is checked numerically. A commercial numerical tool FARADAY based on the Boundary Element Method (BEM) is employed to

reveal the distribution of the electromagnetic components across plate thickness. FARADAY is a CAE software package designed to perform full 3D simulations of both Time Harmonic (eddy current) and Magnetostatic physical systems.

The configuration of wire-plate shown in Fig. 3.8 is selected for testing. Firstly, the field values of the electromagnetic components distributed on the bottom and top surfaces of the plate are directly obtained from IES-FARADAY. Then, using the double exponential functions to calculate the field values on the selected positions (1, 2, 3), as shown in Fig. 4.2. Finally, the results are compared with the corresponding values from IES-FARADAY.

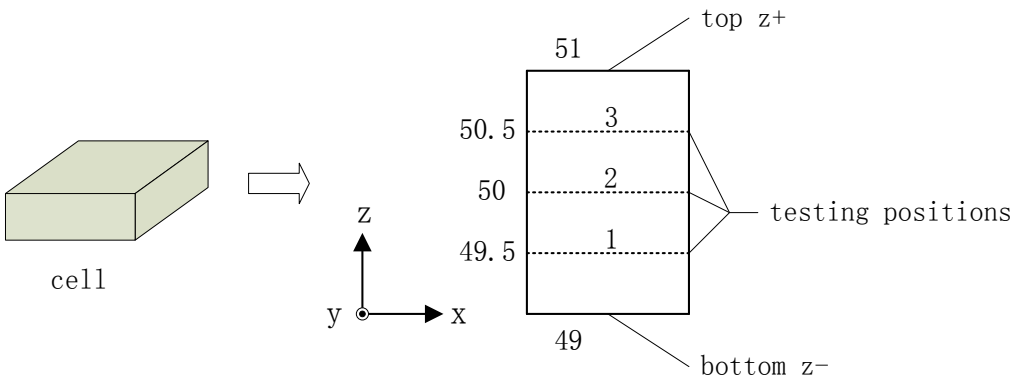

Figure 4.2 Testing positions in a cell.

Fig. 4.3 shows the flat ferromagnetic plate for numerical evaluation using the FARADAY. The plate is made from linear magnetic material with $\sigma = 7.5 \times 10^6 \mathrm{S/m}$ and $\mu_r = 200$. The plate has the dimensions of $200 \times 200 \times 2\mathrm{mm}$. The external source, as seen in Fig. 3.2, is a filamentary conductive loop frame with the dimension of $100 \times 100\mathrm{mm2}$, and it carries the current of $\mathrm{I} = 1\mathrm{A}$ at the frequency of $\mathrm{f} = 50\mathrm{Hz}$. The source is located in the center with the

separation distance of 50mm from the plate.

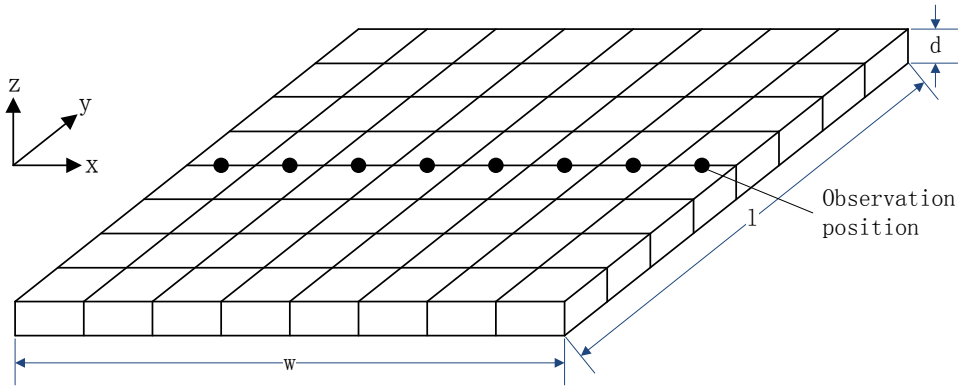

Figure 4.3 The plate under investigation.

A set of middle lines within the plate have been chosen for comparison with the analytical function, as shown in Fig. 4.2. The results of the lines located on the bottom and top (position=49mm, 51mm) of the plate have been obtained from the IES-FARADAY firstly. Then, the values on the top and bottom surfaces of the plate are used to construct the analytical functions given in Eq. (4.2) and (4.3). These functions are finally to computer the values on three lines (position=49.5mm, 50mm, 50.5mm). The calculated results are compared with the corresponding values from IES-FARADAY. Fig. 4.4 is the geometry in the IES-FARADAY environment.

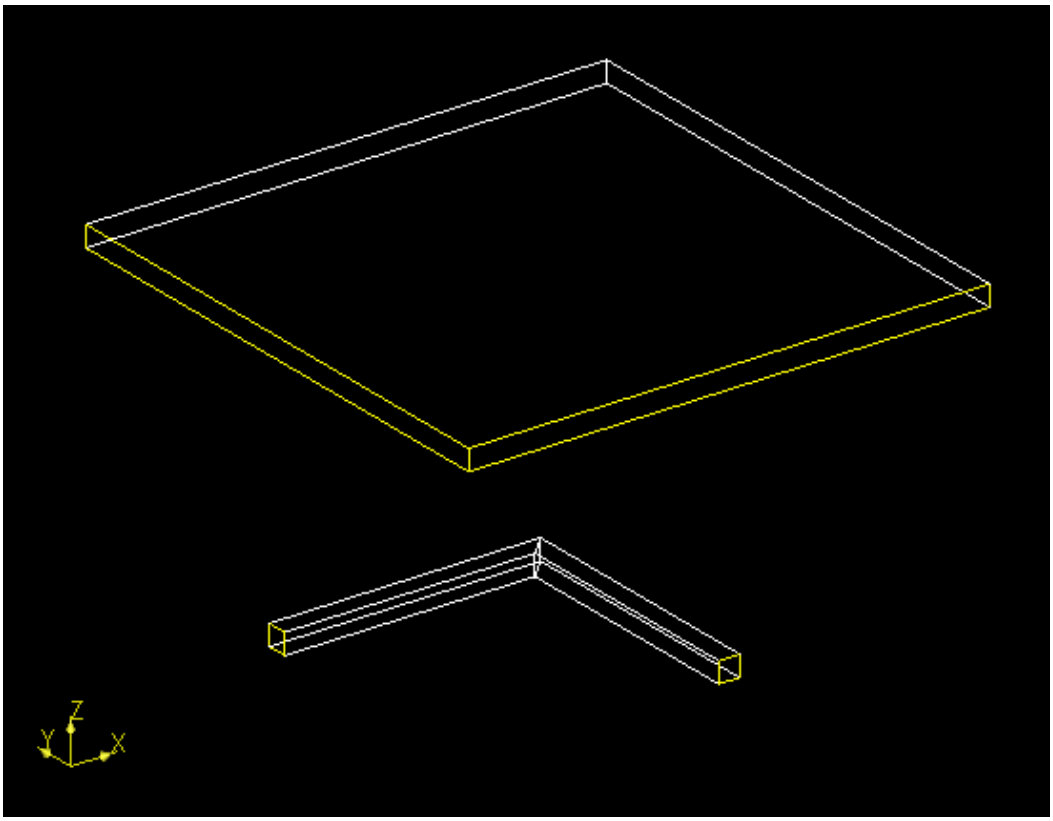

Figure 4.4 The geometry under computation in IES-FARADAY.

In order to make the comparison scientifically, the results are departed into the real part and the imaginary part. Fig. 4.5 shows the comparison of induced current density on the plate. It can be seen that, both the real part and the imaginary part of current density J_y are agreed with the double exponential function very well. Except the singular values on the edge, the deviations on almost area are close to zero. The average error is around 0.2%.

The results of magnetic density M_x are also agreed well with the software, as seen in Fig. 4.6. The average error is less than 0.3%. For the magnetic density component of M_z, there is a significant deviation at the edge points. Except this special position, the deviation can be neglected.

As a result, the analytical expression of double exponential function can be

applied in most part of the plate. For the area closed to the side, the analytical expression cannot describe the magnetic density M_z accurately. And for J_y and M_x, there still exist tiny deviations in the area closed to side. However, the refinement of meshing can be used to decrease this deviation.

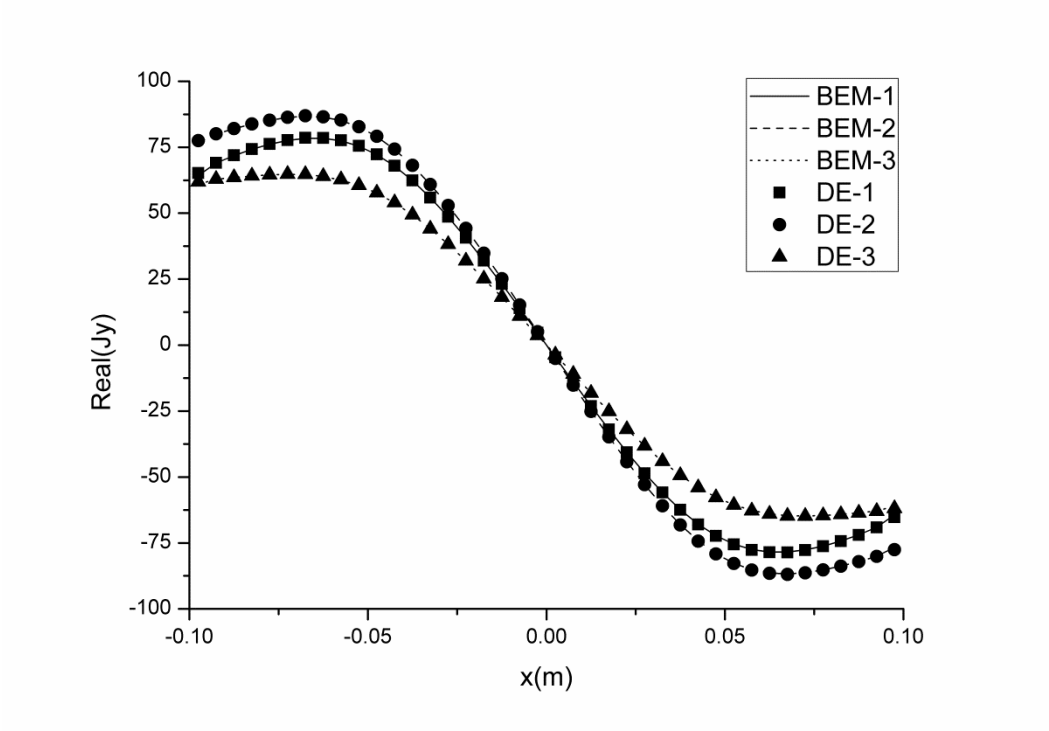

(a) The real part of magnetization density *Jy*.

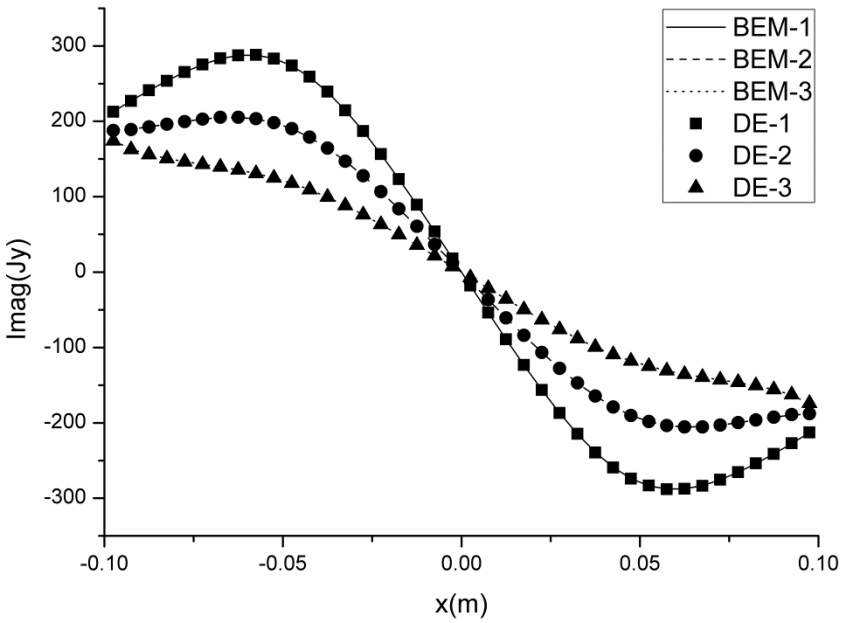

(b) The imaginary part of magnetization density *Jy*.

Figure 4.5 Validation of the analytical expression for current density J_y.

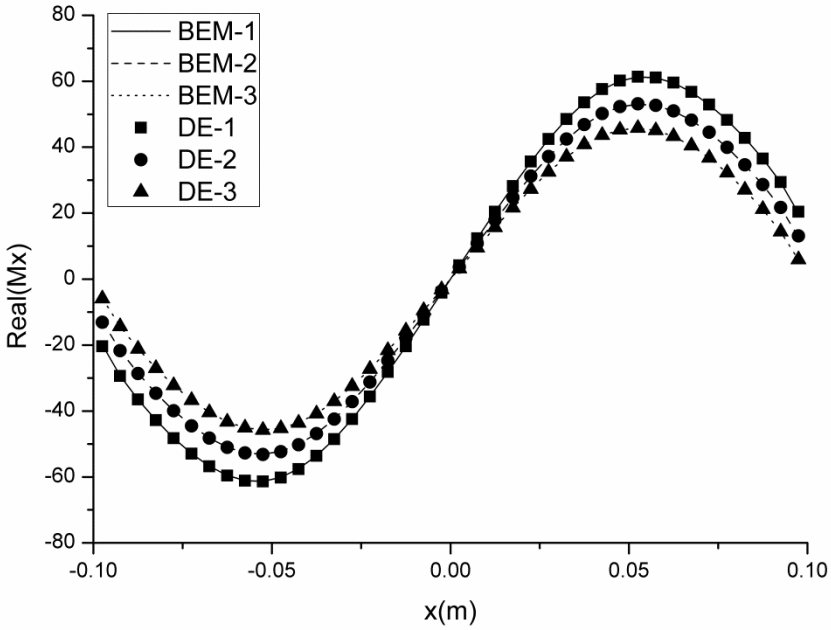

(a) The real part of magnetization density *Mx*.

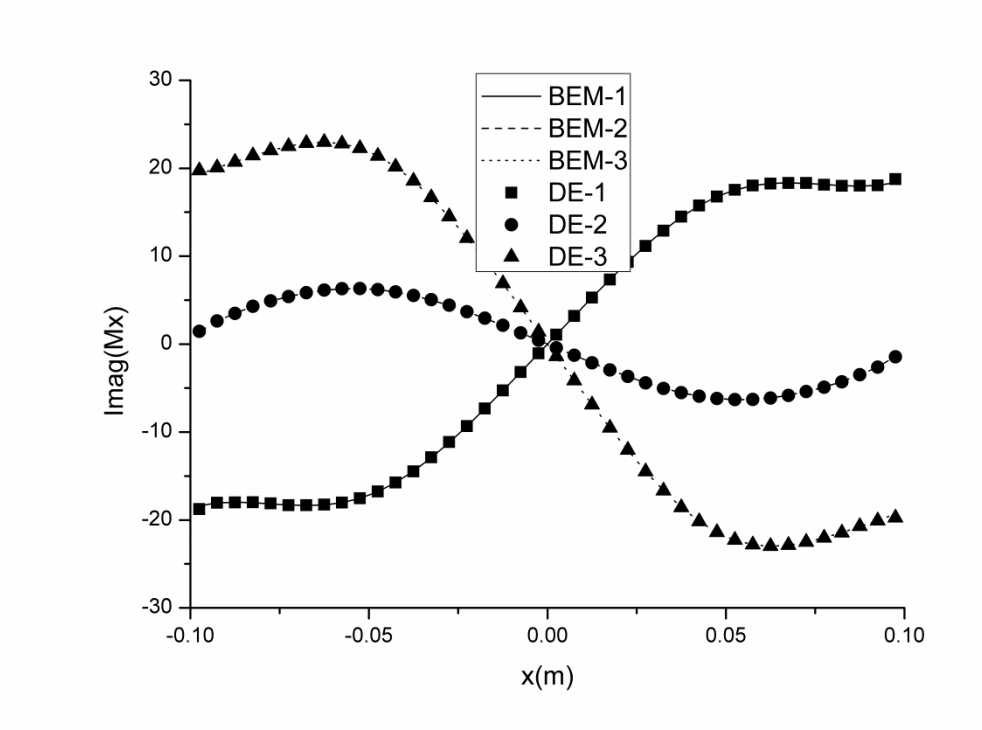

(b) The imaginary part of magnetization density *Mx*.

Figure 4.6 Validation of the analytical expression for magnetic density M_x.

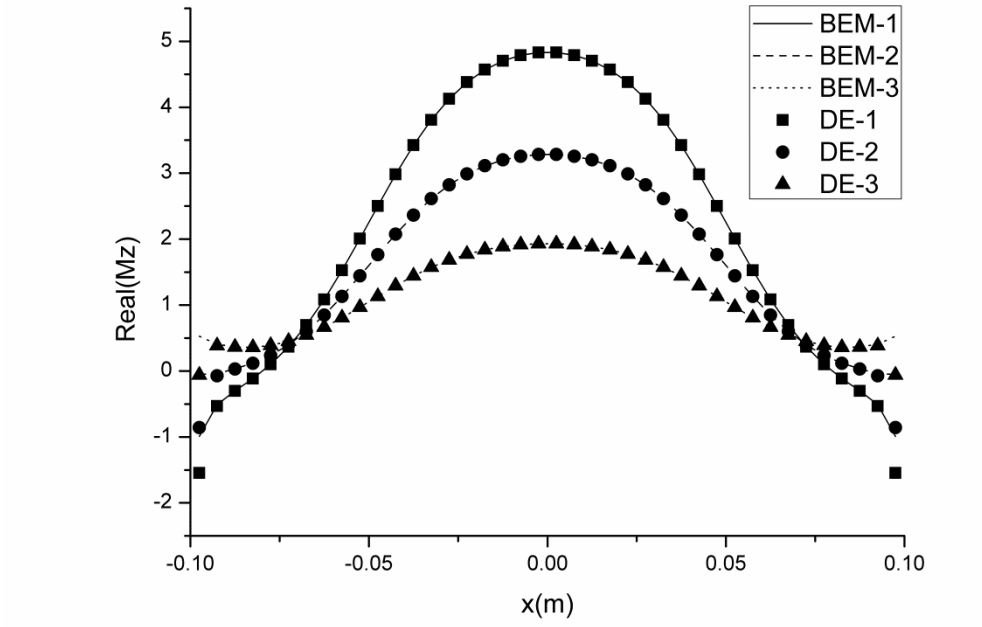

(a) The real part of magnetization density *Mz*.

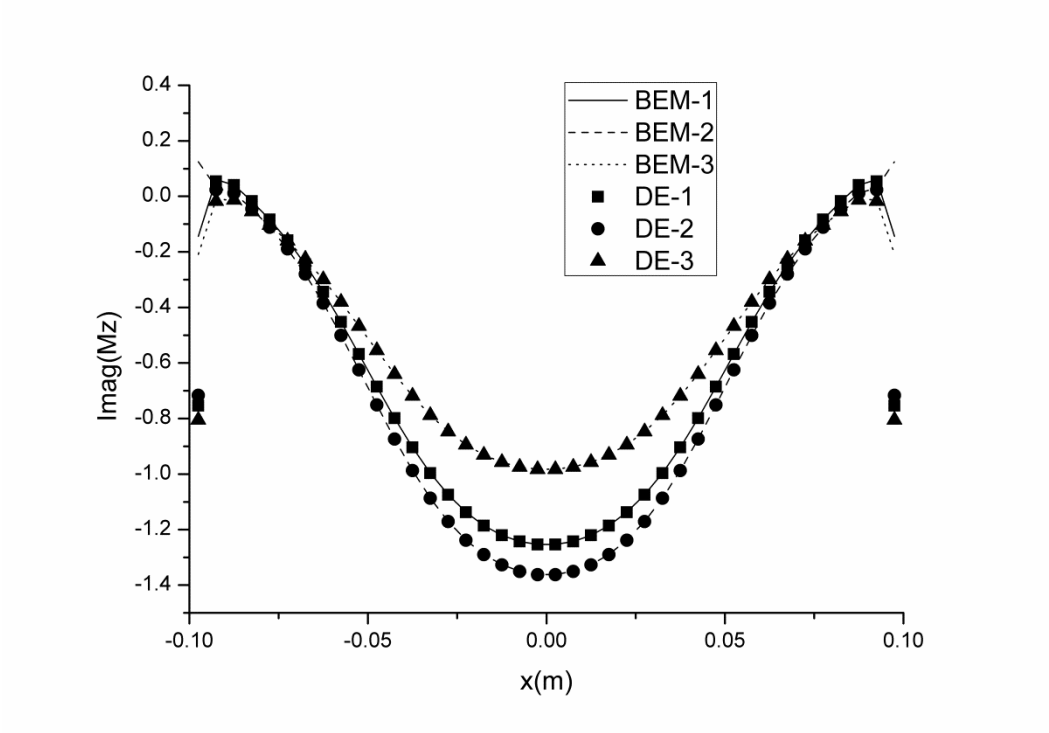

(b) The imaginary part of magnetization density *Mz*.

Figure 4.7 Validation of the analytical expression for magnetization density M_z.

4.2. Application of the Expression to Induced Current

As the flat metal plate is concerned, the analytical expression is applied to describe the distribution of induced current over the cross section of the plate. The induced current density ***J*** in the cells are replaced by unknowns defined on the cell bottom and top surfaces, i.e., $\mathbf{J}^-$, $\mathbf{J}^+$. As seen in Fig. 4.8, the assumption of constant in each cell is replaced by the analytical function along the thickness.

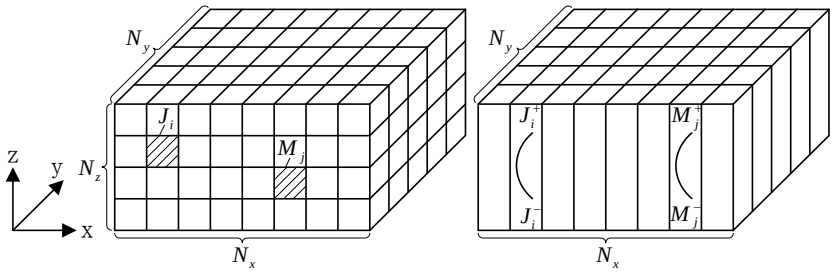

(a) constant value in cells (b) analytical function in cells.

Figure 4.8 Meshing techniques across plate thickness.

And the KCL equations are applied to enforce the continuity of current at potential nodes. As the distribution function of current density is identical in all current cells, the current continuity holds on any x-y plane of a potential cell. KCL equations are then set up on the bottom and top surfaces of all potential cells, as follow:

$$\mathbf{C_x} \bullet \mathbf{J}_x^{-,+} + \mathbf{C_y} \bullet \mathbf{J}_y^{-,+} = 0 \tag{4.4}$$

where $\mathbf{C_x}$ and $\mathbf{C_y}$ are respectively the nodal incidence matrices for x-dir. and y-dir. current cells.

Then, the solution matrix (3.13) can be rewritten as follow:

$$\begin{bmatrix} \mathbf{L_x} & \mathbf{0} & \mathbf{C}_x^t \\ \mathbf{0} & \mathbf{L_y} & \mathbf{C}_y^t \\ \mathbf{C_x} & \mathbf{C_y} & \mathbf{0} \end{bmatrix} \begin{bmatrix} \mathbf{J_x}^{-,+} \\ \mathbf{J_y}^{-,+} \\ \mathbf{\Phi}^{-,+} \end{bmatrix} = \begin{bmatrix} \mathbf{U_{sx}}^{-,+} \\ \mathbf{U_{sy}}^{-,+} \\ \mathbf{0} \end{bmatrix} \tag{4.5}$$

where $\mathbf{\Phi}^{-,+}$ is the potential at nodes. $\mathbf{U_s}^{-,+}$ is the inductive voltage on the bottom and up surfaces of cells, which are contributed by the current source. In (4.5) both $\mathbf{L_x}$ and $\mathbf{L}_y$ are the equivalent impedance of current cells. Assuming $\hat{u}_{ij}$ is zero if $i \neq j$, and $\hat{u}_{ij}$ is one if $i = j$, elements in sub-matrix of (4.5) are given by:

$$\mathrm{L_{ij}} = \frac{l_i}{\sigma}\hat{u}_{ij} + \frac{j\omega\mu_0}{4\pi}\int_{l_i}\int_{v_j}\frac{k}{|r_i - r_j'|}dv'dl \tag{4.6}$$

$$\mathrm{U_{s,i}} = \frac{j\omega\mu_0}{4\pi}\sum_{j=1}^{N_s}\int_{l_i}\int_{l_j'}\frac{I_{s,j}}{|r_i - r_j'|}dl'dl \tag{4.7}$$

where $f(r)$ represents the unit vector for $\boldsymbol{J}(r)$. Parameter k is determined by the density distribution function, and is give by

$$k = \frac{sh(\alpha(d/2 - z'))}{sh(\alpha d)} \tag{4.8a}$$

for unknowns on the top surfaces, and

$$k = \frac{sh(\alpha(d/2 + z'))}{sh(\alpha d)} \tag{4.8b}$$

on the bottom surface..

For validation, the same material characteristic and the structure as in section 3.2.1 are applied. Using an uniform mesh in the x-y plane of 40×40, the plate is divided into a large number of potential cells. And the observation position for resultant magnetic field is as same as in section 3.2.1. The comparison position for the current density J_y is at the middle line on the bottom of the plate.

It can be seen that the solutions, both the electromagnetic components distributed in the plate and the resultant magnetic field in the space are matched very well with the software. It also confirms that the analytical expression of double exponential function for current densities is available and accurate.

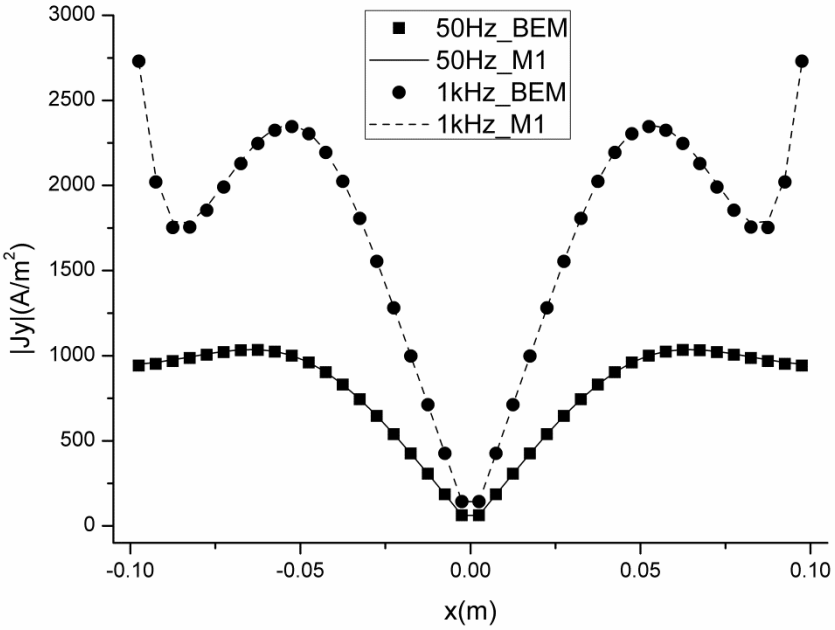

Figure 4.9 Current density J_y at the line (y=0) on the bottom of the plate.

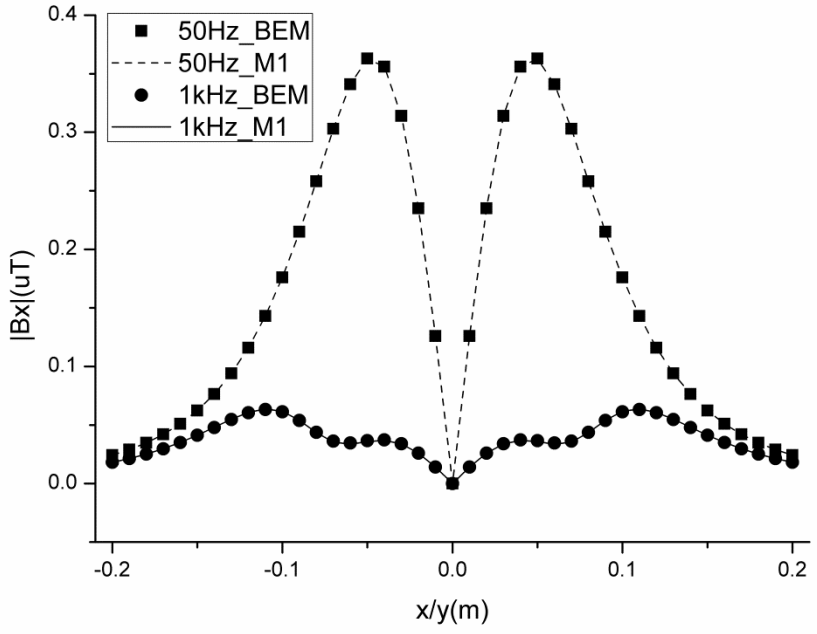

(a) B_x

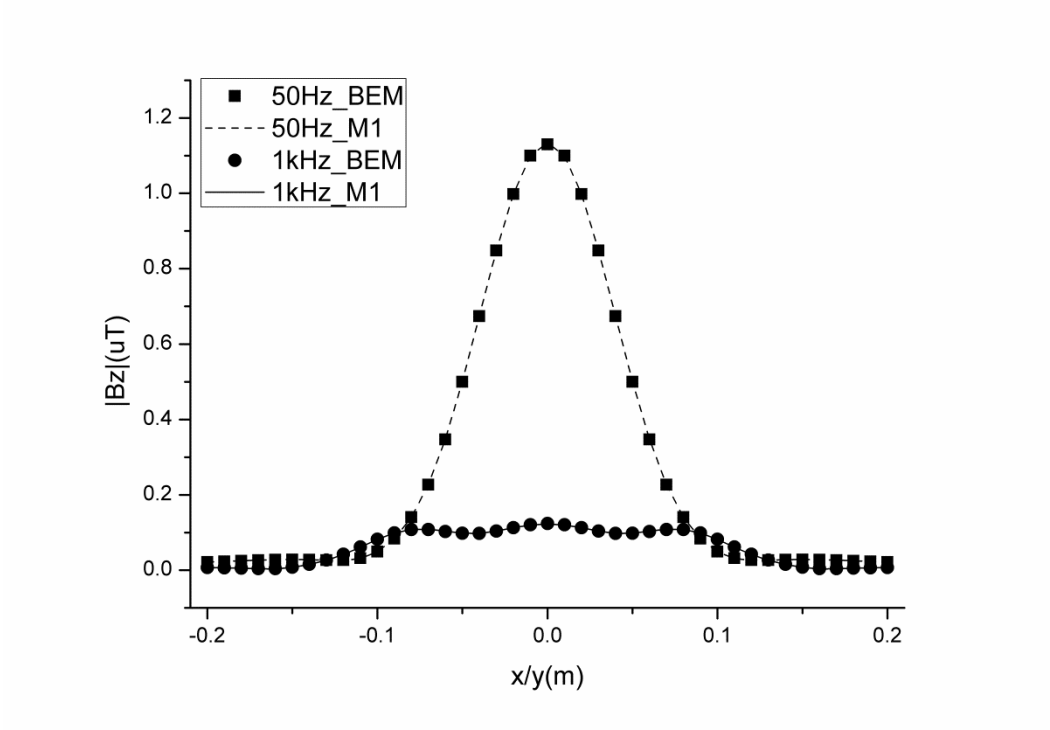

(b) B_z

Figure 4.10 Comparison of B field at a diagonal line above the plate.

4.3. An Improved Method for Evaluating Magnetic Field

In this section, an improved equivalent circuit method (named "IM1") for evaluating low-frequency magnetic fields in the presence of non-ferromagnetic plate is presented. In this method, a double-exponential function is adopted for the eddy current distribution across the thickness of a plate. A voltage equation is established by applying the electric current integral equation on the middle plane of the thin plate. Using the proposed meshing model an equivalent circuit network is established. The equivalent branch current, which is the current density on the middle plane, can be solved directly using the transitional circuit analysis techniques. This method is tested on a model made of a conductive plate excited by an external current source. The results are compared with other integral

equation method, and a good agreement is found in the simulation. In this method there is only one unknown for each cell. The total number of unknowns is significantly reduced. It is efficient to solve the eddy-current or shielding problems containing thin plates.

As stated above, in a current cell i, the current density $J_i(z)$ varies along the z direction, but remains constant on a x-y plane. When the cell size is small, the current density in the cell can be approximated by a double exponential function, as follows:

$$J_i(z) = \frac{J_i^- sh(\alpha(d/2 - z)) + J_i^+ sh(\alpha(d/2 + z))}{sh(\alpha d)} \tag{4.9}$$

where d is the thickness of the plate, J_i^- and J_i^+ are the current densities on the bottom surface ($-d/2$) and the top surface ($d/2$) of the plate, respectively.

In solving the eddy current efficiently the current density at the middle plane of the cell ($z = 0$) is introduced as the unknown variable. According to Eq. (4.7), the current density $J_{0,i}$ can be expressed using J_i^- and J_i^+, as follow:

$$J_{0,i} = \frac{sh(\alpha d/2)}{sh(\alpha d)}(J_i^- + J_i^+) \tag{4.10}$$

It is noted from Eq. (3.19) that voltage V_i in current cell i is balanced by resistive and inductive voltages generated by the current in cell i, and inductive voltage generated by other cell j ($j = 1 \ldots N$). N is the number of total cells in the plate. Applying Eq. (3.19) on a line at z=0 (middle plane) in the current cell yields a branch voltage equation for cell i at frequency ω, as follows:

$$V_i(0)=\frac{l_i}{\sigma}J_{0,i}+\frac{j\omega\mu_0}{4\pi}\left(\sum_{j=1}^{N}\int_{l_i}\int_{v_j'}\frac{J_j(z')}{R_{z'}}dv'dl+\sum_{k=1}^{M}I_k\int_{l_i}\int_{l_k'}\frac{1}{|r-r'|}dl'dl\right) \qquad (4.11)$$

in which I_k is the current in external source wire k, and M is the number of wires. And distance $R_{z'}=|r-r'|$ when z=0, and is given by $\sqrt{(x-x')^2+(y-y')^2+(z')^2}$.

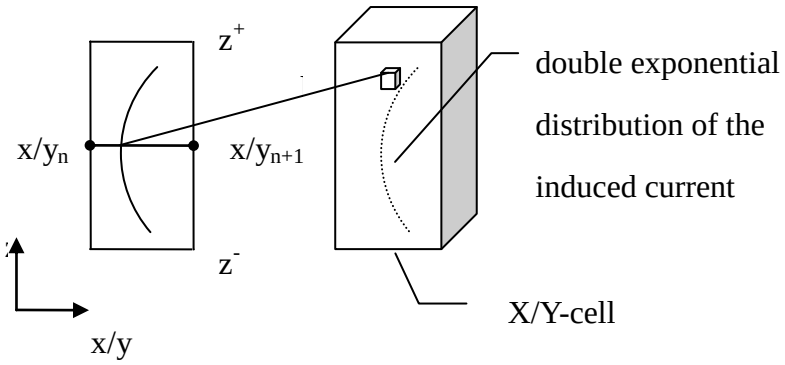

Figure 4.11 Interaction from current cells to electrical branch.

Substituting (4.10) in (4.11) yields a voltage equation for a circuit branch i, as follows:

$$V_i(0)=R_{ii}J_{0,i}+\sum_{j=1}^{N}j\omega(L_{ij}^{+}J_{ij}^{+}+L_{ij}^{-}J_{ij}^{-})+\sum_{k=1}^{M}j\omega L_{s,ik}I_k \qquad (4.12)$$

where equivalent resistance R_{ii}, equivalent inductance L_{ij}^{+} and L_{ij}^{-}, and source inductance $L_{s,ik}$ are given by

$$\begin{aligned}
R_{ii} &= \frac{l_i}{\sigma}\\
L_{ij}^{+} &= \frac{\mu_0}{4\pi}\sum_{j=1}^{N}\int_{l_i}\int_{x_j}\int_{y_j}\int_{z_j}\frac{sh[\alpha(d/2+z')]}{sh(ad)R}dz'dy'dx'dl\\
L_{ij}^{-} &= \frac{\mu_0}{4\pi}\sum_{j=1}^{N}\int_{l_i}\int_{x_j}\int_{y_j}\int_{z_j}\frac{sh[\alpha(d/2-z')]}{sh(ad)R}dz'dy'dx'dl\\
L_{s,ik} &= \int_{l_i}\int_{l_k'}\frac{1}{|r-r'|}dl'dl
\end{aligned} \qquad (4.13)$$

Note that two definite integrals are identical to each other, that is,

$$\int_{-\frac{d}{2}}^{\frac{d}{2}} \frac{sh[\alpha(d/2+z')]}{sh(\alpha d)R_{z'}} dz' = \frac{2sh(\alpha d/2)}{sh(\alpha d)} \int_0^{\frac{d}{2}} \frac{ch(\alpha z')}{R_{z'}} dz$$
$$\int_{-\frac{d}{2}}^{\frac{d}{2}} \frac{sh[\alpha(d/2-z')]}{sh(\alpha d)R_{z'}} dz' = \frac{2sh(\alpha d/2)}{sh(\alpha d)} \int_0^{\frac{d}{2}} \frac{ch(\alpha z')}{R_{z'}} dz' \quad (4.14)$$

Voltage equation (5.3) is then simplified into

$$V_i(0) = R_{ii} J_{0,i} + \sum_{j=1}^{N} j\omega L_{ij} J_{0.j} + \sum_{k=1}^{M} j\omega L_{s,ik} I_k \quad (4.15)$$

where $L_{ij} = \frac{\mu_0}{2\pi} \sum_{j=1}^{N} \int_{l_i} \int_{x_j} \int_{y_j} \int_0^{\frac{d}{2}} \frac{ch(\alpha z')}{R_{z'}} dz' dy' dx' dl$.

It is noted in (4.15) that there is only one unknown in each current cell. The total number of unknowns is, therefore, significantly reduced.

Now a current cell shown in Fig. 4.11 is represented by a circuit component with its self-resistance and inductance, and mutual inductance with other cells. The circuit component is connected to other components at the potential nodes. Therefore, an equivalent circuit network, which consists of a number of circuit cells, is formulated after using the grid generation approach described above. Using the transitional circuit analysis techniques, current density or eddy current in the plate can be numerically obtained.

The magnetic field around the plates can be calculated using the formula $B = \nabla \times A$, where vector potential A is contributed by both the eddy current and source current, as illustrated in . Consider the distance to an observation point is usually much greater than plate thickness. Distance $|r - r'|$ is independent of z', and can be approximately expressed by $R_z = \sqrt{(x-x')^2 + (y-y')^2 + z^2}$. Therefore, the term contributed by the eddy current is expressed by

$$A_c(z) = \frac{\mu_0}{4\pi} \sum_{j=1}^{N} \int_{l_i} \int_{x_j} \int_{y_j} \int_{z_j} \frac{J_j(z')}{R_z} dz' dy' dx' dl \tag{4.16}$$

After substituting (4.10) in (4.16) and using the identity given in (4.14), the vector potential contributed by the eddy current is given by

$$A_c(z) = \frac{\mu_0}{2\pi} \sum_{j=1}^{N} \int_{l_i} \int_{x_j} \int_{y_j} \int_{0}^{\frac{d}{2}} \frac{ch(\alpha z')}{R_{z'}} dz' dy' dx' dl \tag{4.17}$$

It can be seen that the current density distributed on the center plane of the plate is matched very well with the solution from software, and the resultant magnetic field in the space are also matched very well.

The proposed method has been implemented in MATLAB, and tested on one plate model. As shown in Fig. 3.8, the configuration of the model in the presence of an external magnetic field generated from a loop coil. The aluminum plate has the conductivity of $\sigma = 3.8 \times 10^7$ S/m, and the dimension is $200 \times 200 \times 2\text{mm}^3$. The coil in this case carries the current of 1 A at 50 Hz or 1 kHz. In the computation the plate was divided into 40×40 potential cells. A uniform meshing model based on the classic integral equation (IE method) was also applied to do the calculation for comparison.

By using the proposed method, the current density on the middle plane of the plate is solved directly. Fig. 4.12 shows the y-component of the current density on the plate, which is distributed symmetrically on the plane.

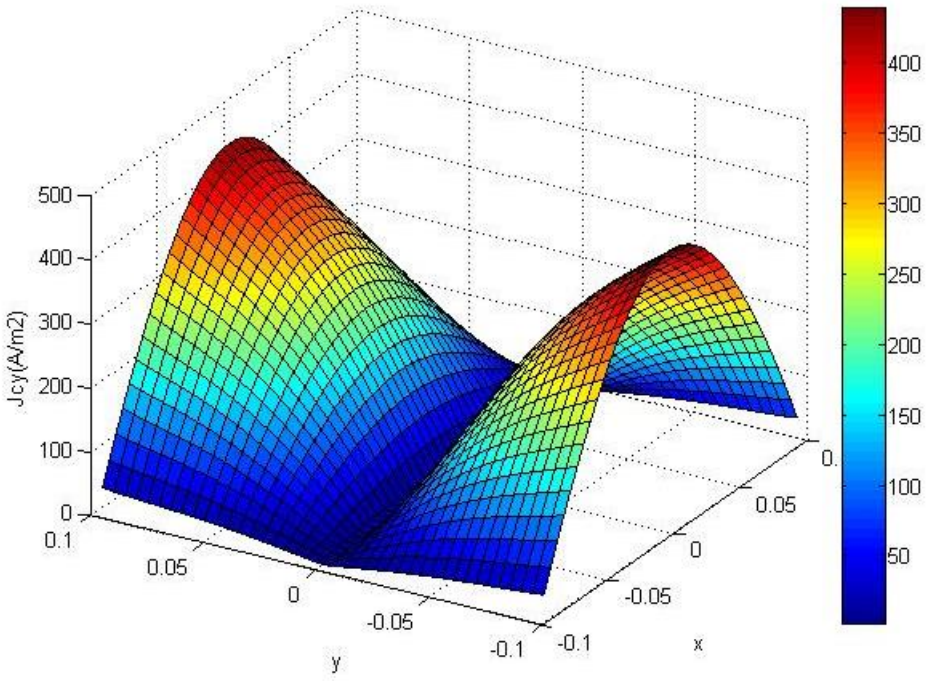

Figure 4.12 The induced current density on the middle plane of plate

For comparison, the y-component of the induced current density on the middle line within the plate ($J_{cy}, y=0$) were extracted. The results computed by the proposed method and the IE method at 50 Hz and 1 kHz are presented in Fig. 4.13 (a) and (b), respectively. It is noted from the figures that the current distribution computed by these two methods matches very well. Fig. 4.14 shows the resultant magnetic field on a horizontal line at the distance of 0.1m above the plate. It is noted that the field results at 50Hz match well again.

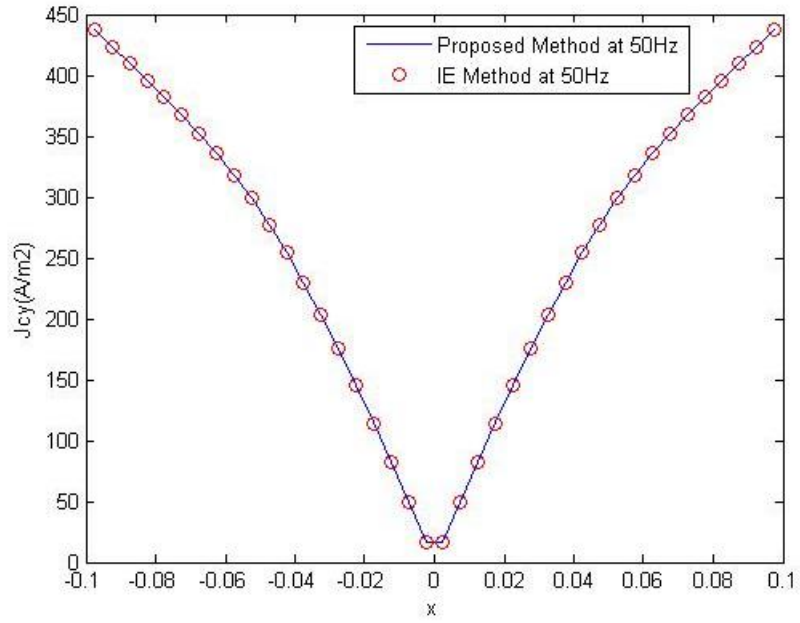

(a) 50 Hz

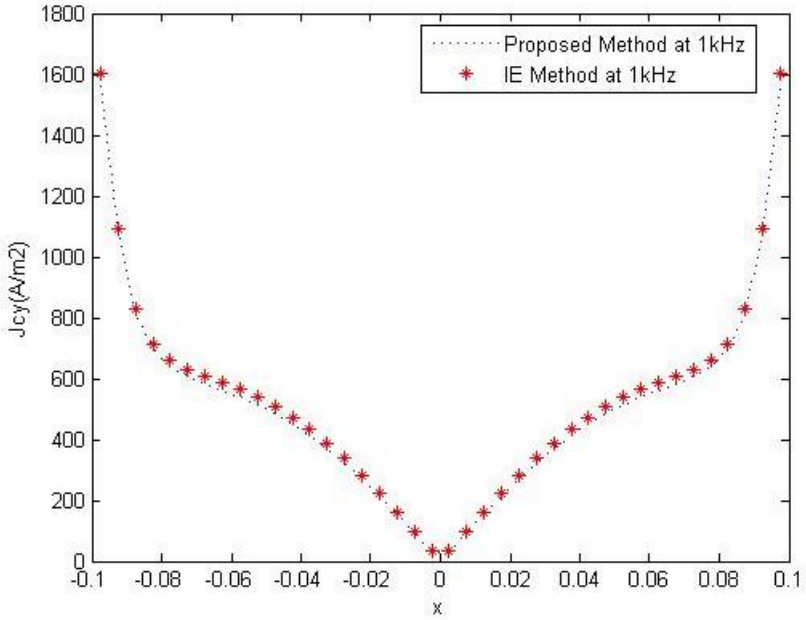

(b) 1kHz

Figure 4.13 Comparison of the current density on the middle line

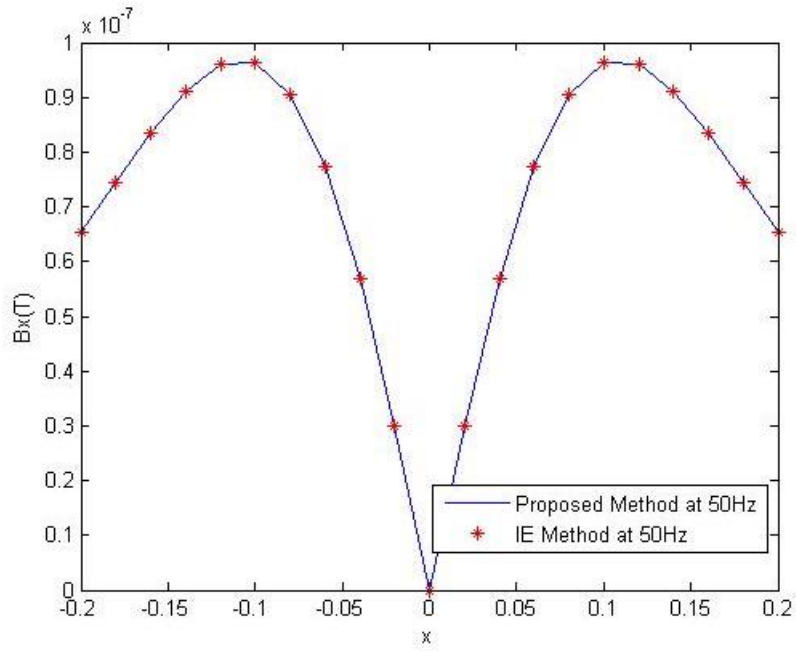

Figure 4.14 Comparison of the magnetic fields comparison at 50Hz.

4.4. Application of the Expression to Magnetization

Magnetic vector ***A****m* in a magnetic plate is generally expressed by:

$$\boldsymbol{A}_m(\boldsymbol{r}) = \frac{\mu_0}{4\pi}\int_{v'} \frac{\nabla \times \boldsymbol{M}(\boldsymbol{r}')}{|\boldsymbol{r}-\boldsymbol{r}'|} dv' + \frac{\mu_0}{4\pi}\int_{s'} \frac{\boldsymbol{M}(\boldsymbol{r}')\times \boldsymbol{n}'}{|\boldsymbol{r}-\boldsymbol{r}'|} ds' \tag{4.18}$$

When magnetic polarization in a volume cell is constant, the first term in $\boldsymbol{A}_{\mathrm{m}}$ is identical to zero, which was adopted in [11]. However, very fine meshing is required in this case as ***M*** varies significantly within the plate. In this chapter, an analytical function is adopted for magnetization density across plate thickness, and no discritzation is required along this direction. Similar to the induced current, magnetization density $\boldsymbol{M}$ can be expressed analytically, as follow:

$$\boldsymbol{M}_i(z) = \frac{\boldsymbol{M}_i^- sh(\alpha(d/2-z)) + \boldsymbol{M}_i^+ sh(\alpha(d/2+z))}{sh(\alpha d)} \tag{4.19}$$

Vector potential $\boldsymbol{A}_m$ is then expressed by:

$$\boldsymbol{A}_m(\boldsymbol{r}) = \frac{\mu_0}{4\pi}\int_{v'} \frac{\boldsymbol{M}(\boldsymbol{r}')\times(\boldsymbol{r}-\boldsymbol{r}')}{|\boldsymbol{r}-\boldsymbol{r}'|^3} dv' \tag{4.20}$$

As a result, the voltage equation in can be rewritten as:

$$\begin{aligned}&\frac{1}{\sigma}\int_{l_i}\boldsymbol{J}_i(\boldsymbol{r})dl+\frac{j\omega\mu_0}{4\pi}\sum_{j=1}^{N_c}\int_{l_i}\int_{v_j}\frac{\boldsymbol{J}_j(\boldsymbol{r}')}{|\boldsymbol{r}-\boldsymbol{r}'|}dvdl+\\&\frac{j\omega\mu_0}{4\pi}\sum_{j=1}^{N_m}\int_{l_i}\int_{v_j}\frac{\boldsymbol{M}_j(\boldsymbol{r}')\times(\boldsymbol{r}-\boldsymbol{r}')}{|\boldsymbol{r}-\boldsymbol{r}'|^3}dvdl+\Delta V_i\\&=\frac{j\omega\mu_0}{4\pi}\sum_{j=1}^{N_s}\int_{l_i}\int_{l_j'}\frac{\boldsymbol{I}_{s,j}(\boldsymbol{r}')}{|\boldsymbol{r}-\boldsymbol{r}'|}dl'dl\end{aligned}\tag{4.21}$$

where N_c, N_m, N_s represent the number of current cells, potential cells and source cells, respectively.

Magnetization $\boldsymbol{M}_j$ ($j=1...N_m$) is introduced as additional unknowns in modeling magnetic plates. Additional equations are needed to make the problem well posed. Assume that the plate material is linear, and is characterized by relative permeability μ_r. According to the constitution law:

$$\boldsymbol{B}(\boldsymbol{r})=\frac{\mu_0\bullet\mu_r}{\mu_r-1}\boldsymbol{M}(\boldsymbol{r})\tag{4.22}$$

Note that magnetic flux density $\boldsymbol{B}$ is expressed by vector potential $\boldsymbol{A}$. The following equation then yields:

$$\frac{\mu_0\bullet\mu_r}{\mu_r-1}\boldsymbol{M(r)}=\nabla\times\boldsymbol{A(r)}\tag{4.23}$$

The equation for magnetization density $\boldsymbol{M}$ at any node is established, as follows:

$$\begin{aligned}&\frac{\mu_0}{4\pi}\sum_{j=1}^{N_s}\int_{l_j'}\nabla\times\frac{\boldsymbol{I}_{s,j}(\boldsymbol{r}')}{|\boldsymbol{r}-\boldsymbol{r}'|}dl'=\frac{\mu_0}{4\pi}\sum_{j=1}^{N_c}\int_{v_j}\nabla\times\frac{\boldsymbol{J}_j(\boldsymbol{r}')}{|\boldsymbol{r}-\boldsymbol{r}'|}dv\\&+\frac{\mu_0}{4\pi}\sum_{j=1}^{N_m}\int_{v_j}\nabla\times\frac{\boldsymbol{M}_j(\boldsymbol{r}')\times(\boldsymbol{r}-\boldsymbol{r}')}{|\boldsymbol{r}-\boldsymbol{r}'|^3}dv-\frac{\mu_0\bullet\mu_r}{\mu_r-1}\boldsymbol{M}_i(\boldsymbol{r})\end{aligned}\tag{4.24}$$

As similar as the matrix equation (4.5), add the magnetization density as the unknown, the new matrix equation can be set up:

$$\begin{bmatrix} \mathbf{L_x} & \mathbf{0} & \mathbf{C}_x^t & \mathbf{Q_x} \\ \mathbf{0} & \mathbf{L_y} & \mathbf{C}_y^t & \mathbf{Q_y} \\ \mathbf{C_x} & \mathbf{C_y} & \mathbf{0} & \mathbf{0} \\ \mathbf{T_x} & \mathbf{T_y} & \mathbf{0} & \mathbf{P} \end{bmatrix} \begin{bmatrix} \mathbf{J_x^{-,+}} \\ \mathbf{J_y^{-,+}} \\ \mathbf{\Phi}^{-,+} \\ \mathbf{M}^{-,+} \end{bmatrix} = \begin{bmatrix} \mathbf{U_{sx}^{-,+}} \\ \mathbf{U_{sy}^{-,+}} \\ \mathbf{0} \\ \mathbf{B_s^{-,+}} \end{bmatrix} \tag{4.25}$$

where $\mathbf{B_s^{-,+}}$ is the magnetic field on the bottom and up surfaces of cells, which is contributed by the current source. In (4.25) both $\mathbf{Q_x}$ and $\mathbf{Q}_y$ are viewed as the **M**-control voltage sources. Assuming $\hat{u}_{ij}$ is zero if $i \neq j$, and $\hat{u}_{ij}$ is one if $i = j$, elements in sub-matrix of (4.25) are given by:

$$\mathrm{Q_{ij}} = \frac{j\omega\mu_0}{4\pi}\int_{l_i}\int_{v_j'} k \bullet \frac{\hat{b}(r_j') \times (r_i - r_j')}{|r_i - r_j'|^3} dv' dl \tag{4.26a}$$

$$\mathrm{T_{ij}} = \frac{\mu_0}{4\pi}\int_{v_j'} k \bullet \frac{\nabla \times f(r_j')}{|r_i - r_j'|} dv' \tag{4.26b}$$

$$\mathrm{P_{ij}} = \frac{\mu_0}{4\pi}\int_{v_j'} k \bullet \frac{\nabla \times (\hat{b}(r_j') \times (r_i - r_j'))}{|r_i - r_j'|^3} dv' - \frac{\mu_0 \bullet \mu_r}{\mu_r - 1}\hat{u}_{ij} \tag{4.26c}$$

$$\mathrm{B_{s,i}} = \frac{\mu_0}{4\pi}\sum_{j=1}^{N_s}\int_{l_j'} \frac{\nabla \times I_{s,j}}{|r_i - r_j'|} dl' \tag{4.26d}$$

where $\hat{b}(r)$ and $f(r)$ represent the unit vector for $\boldsymbol{M}(r)$ and $\boldsymbol{J}(r)$, respectively. By excluding the reference node, the number of total unknowns in (4.25) is reduced to $2\times(6N_xN_y - N_x - N_y - 1)$.

Each a coefficient matrix in (4.25) has the configuration of $\begin{bmatrix} \mathrm{A_{11}} & \mathrm{A_{12}} \\ \mathrm{A_{21}} & \mathrm{A_{22}} \end{bmatrix}$, which reflects the self-coupling and cross-coupling between the quantities distributed on bottom and top surfaces.

The structure under evaluation is as shown in Fig. 3.8. The thin plate is made from linear magnetic materials with the conductivity of $\sigma = 0.75\times10^7 S/m$ and permeability of $\mu_r = 200$. The external source is a filamentary conductor

carrying a current $I = 1A$ at the frequency $f = 50Hz$. The dimensions of the structure are: w=200mm, d=2mm, h=50mm. A non-uniform mesh of 40×40 is adopted.

The M1 has been implemented in MATLAB. For comparison the results computed by the boundary-element method-based (BEM) software IES-FARADAY are presented in the figure as well. Fig. 4.15 shows the eddy current and magnetization density J_y and M_x in the middle line on the bottom of the plate. It can be seen that the results are matched well in most area, a little deviation exist in the area near to edge and the maximum errors are 4.13% and 3.37%, respectively. The two components of resultant magnetic flux density $\boldsymbol{B}$ along a diagonal line above the plate are presented in Fig. 4.16, the resultant magnetic field matched very well and the maximum error is 4.2%.

It is clearly that there are significant deviations between the proposed method and the IES-FARADAY. This is because that when the magnetic material is involved, the EM components which distributed on the plate vary greatly, especially in the edge region. The distribution in the edge region does not strictly comply with the analytical function. The assumption causes the deviation of simulation from the real physical situation.

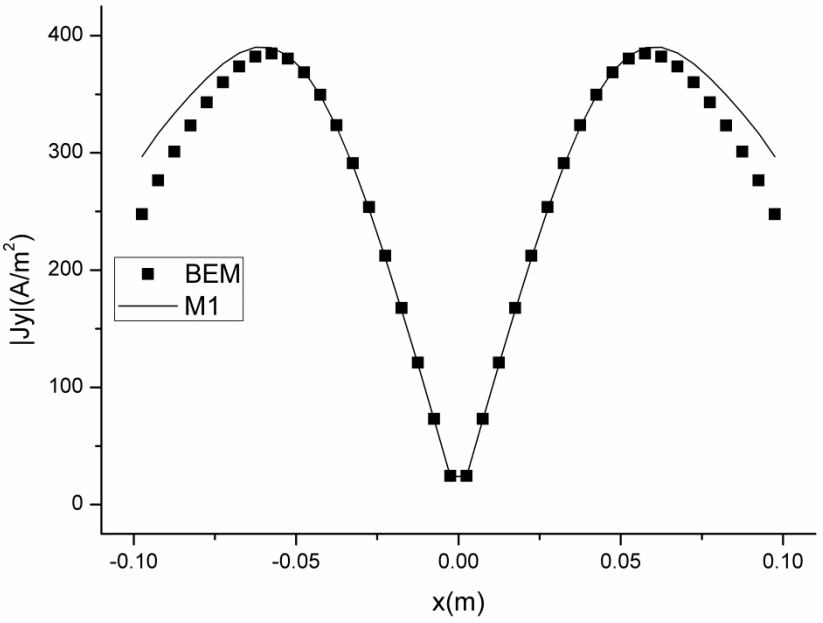

(a) J_y

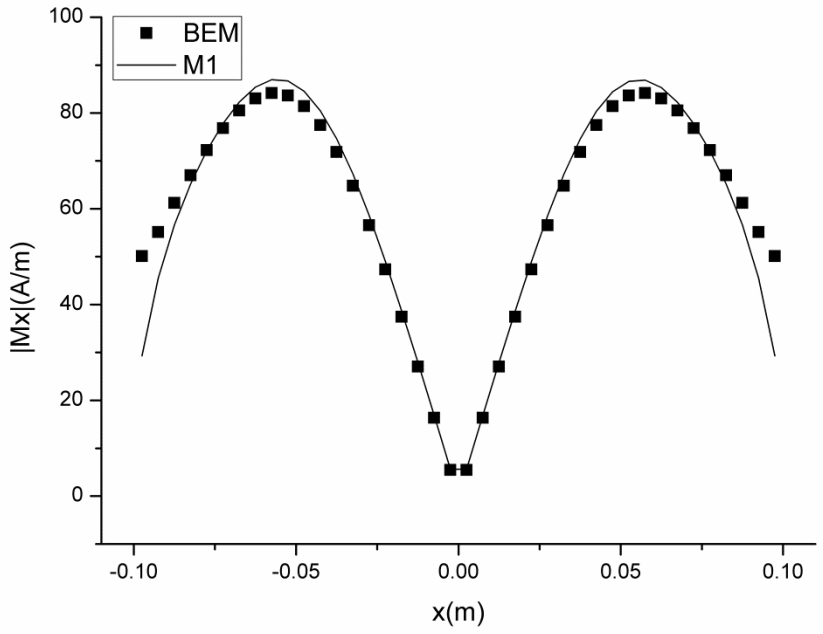

(a) M_x

Figure 4.15 At the middle line (y=0, z=49mm) on the bottom of the plate.

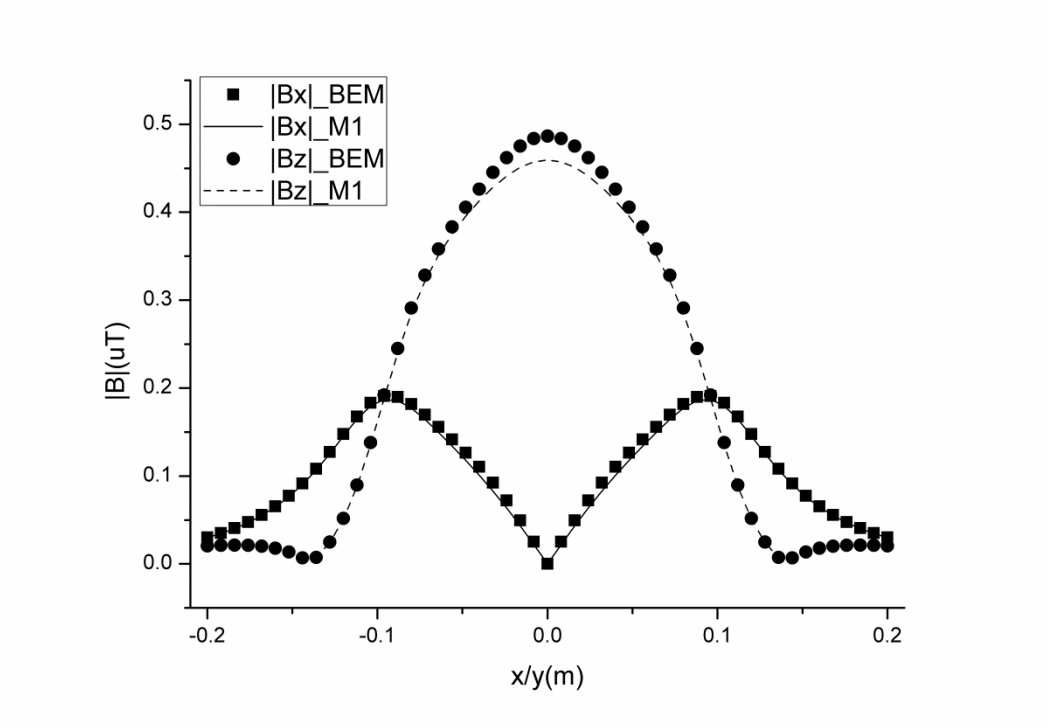

Figure 4.16 Comparison of B field at a diagonal line above the plate.

4.5. Distribution of EM Components

It is obviously that there are deviations for the electromagnetic components distributed on the plate between the proposed methods and IES-FARADAY, as shown in Fig. 4.15. As a contrast, there is a matched well result when the plate is made of non-magnetic material.

In this section, the distribution of different electromagnetic components on the plate will be presented and discussed. And the aim is to obtain the principle of the distribution and find the key factor which causes the deviations.

Due to all the deviations existed in former comparisons are significantly in the edge area of the plate, the characteristics of distribution of the electromagnetic components in this area will be focused. As shown in Fig. 4.17, for a magnetic plate, the edge region with a depth of 6mm is taken for

investigation.

As similar as the validation for the analytical expression in section 4.1.3, the data from IES-FARADAY is employed for investigation. The results on the bottom and top surface from IES-FARADAY will be got firstly. Then, the values of lines L1, L2, L3 shown in Fig. 4.17 can be calculated by using the Eq. (4.2) and (4.3). The results will be compared with the field values obtained directly from IES-FARADAY. The difference will be focused and discussed.

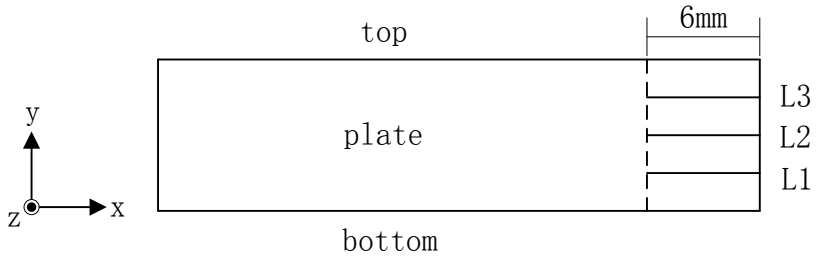

Figure 4.17 Edge region for investigating the distribution of EM components.

As shown in Fig. 4.18, the comparison of the electromagnetic components distributed on the edge area has been done. For the induced current density (Jx, Jy) and the magnetization density components (Mx, My), the characteristics of their distribution comply with the double exponential distribution function in most area, as shown in Fig. 4.18(a-b). In the edge region, roughly estimated 2mm area, there is also a deviation with small amplitude. For the magnetization component , such deviation is significant in the edge region but matched in most area as well, as shown in Fig. 4.18(c). It is this significant deviation resulting in a double exponential distribution assumption on the edge region, which leads the errors existed in the results of electromagnetic components distributed on the plate and the resultant fields around the plate.

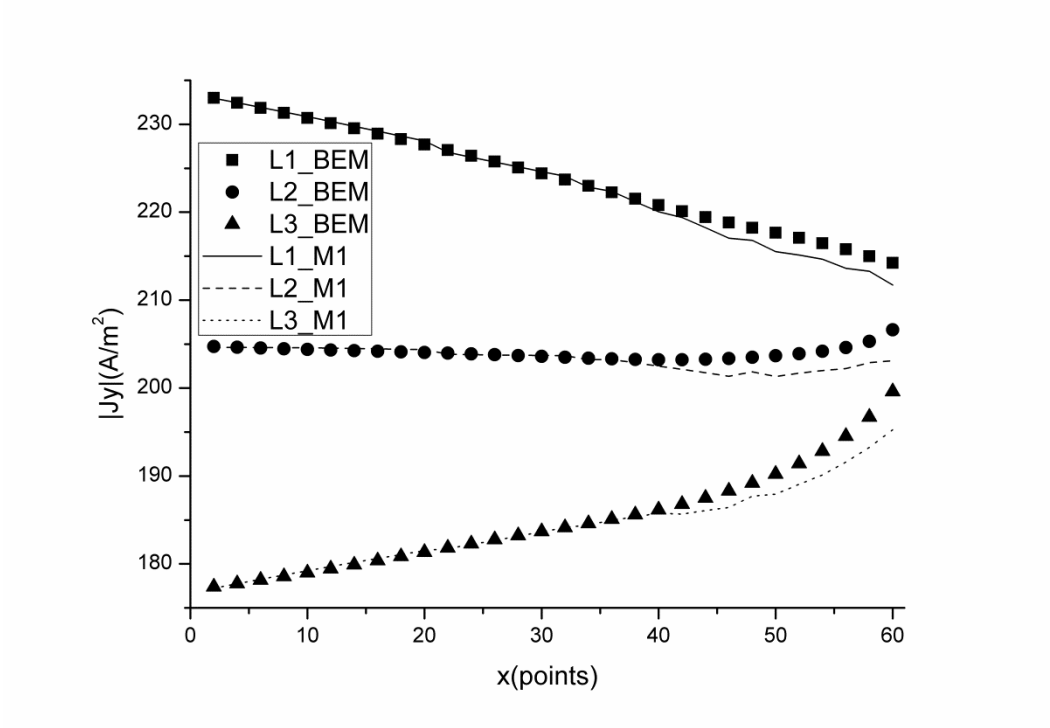

(a) The comparison of the induced current density.

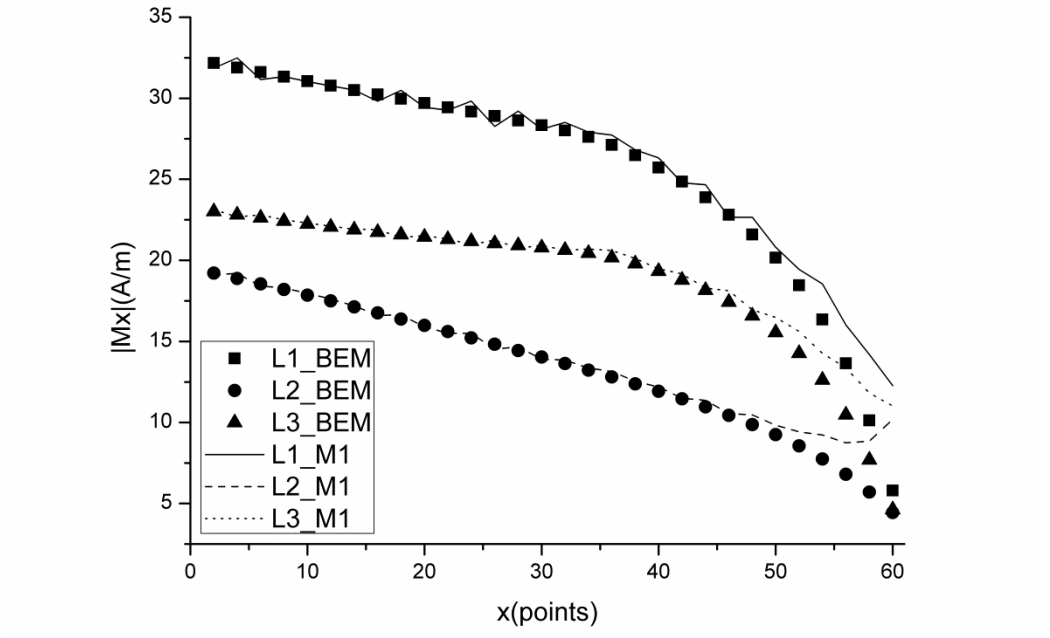

(b) The comparison of the magnetization density.

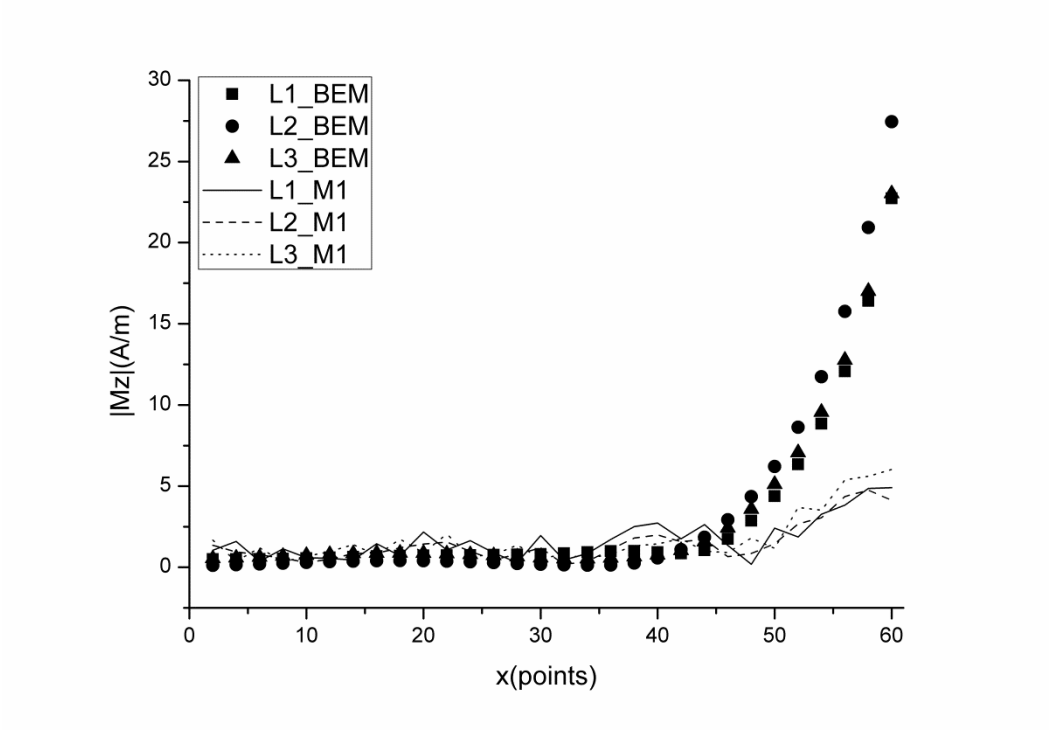

(c) The comparison of the magnetization density.

Figure 4.18 Comparison of the EM components distributed on the edge area.

4.6. A Non-uniform Meshing Technique

For any numerical method, the huge number of unknowns arose from discretization is a heavy burden on computing resources and accordingly limits its application range. How to catch an effective meshing scheme has been being a research focus, which ensures the accuracy of calculation, while produces as little as possible number of unknowns.

The results of previous two PEEC models illustrate that the existing density of grid is not enough to get a precise solution. And it is little significance and unacceptable to increase the density of grid blindly.

In this section, a non-uniform meshing technique is presented, which is based on the principle of the distribution of electromagnetic quantities on the plate.

While taking into account the skin effect from multi-surface in the edge region of the plate, a refinement is done in this region, as shown in Fig. 4.19. In the other hand, some areas, which are closed to the external magnetic field source and with relatively stronger responses, are assigned mesh refinement as well, as shown in Fig. 4.21.

As seen in the Fig. 4.19, the couplings are not only come from the upper and lower surfaces but also the side surface. A region for mesh refinement close to the side can be defined, which is roughly the skin depth $\delta = \sqrt{2/\omega\mu_0\sigma}$ of the plate.

Furthermore, as seen in Fig. 4.18, the electromagnetic components vary steeper when it is closer to the side boundary. A superimposed non-uniform meshing can be done during the refinement region. A set of weighting coefficients, such as [0.1, 0.2, 0.3, 0.4], can be defined to generate the non-uniform segmentation from the side boundary to the interior of plate.

In other regions of the plate, due to the distribution of the electromagnetic components exhibits relatively smooth, uniform grid can meet the requirement. As we known that the great difference between the sizes of adjacent cells will cause the result is not smooth, skip or even inaccurate. Therefore, a connection region is needed between the uniform area and refinement area, as shown in Fig. 4.19. It mitigates the difference of the different sizes of non-uniform grid.

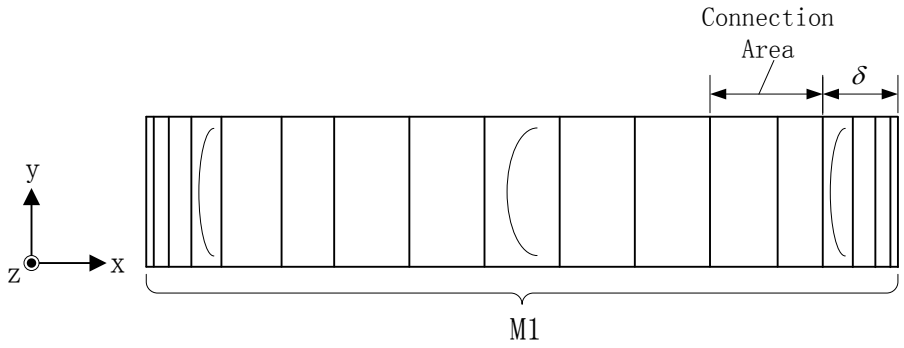

Figure 4.19 Mesh refinement on the edge area.

The proposed meshing scheme is employed for the numerical test presented in Section 4.4. Because this procedure is based on the M1 and with the mesh refinement, it is marked M1_R.

Fig. 4.20 shows the comparison of induced current density and magnetization from different numerical solvers. The results from M1_R which employs the non-uniform meshing scheme are matched with the results from IES-FARADAY. Compared with the results from M1, which applies the uniform meshing scheme, the results from M1_R are at a significant higher accuracy. The average error of induced current density reduces from 3.95% to 0.96%, and for magnetization it is reduces from 5.87% to 2.8%. It is obvious that the proposed meshing scheme improves the accuracy of solution.

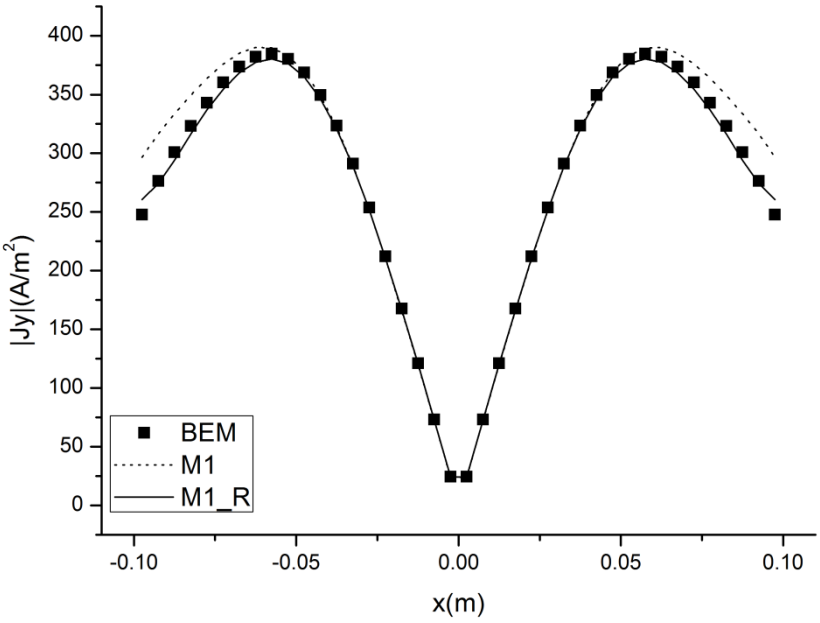

(a) Comparison of induced current density.

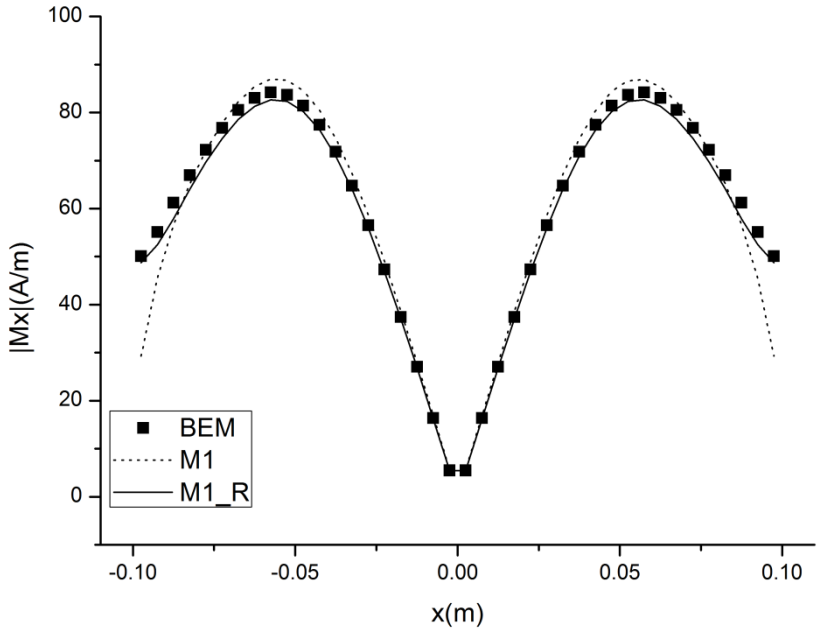

(b) Comparison of magnetization density.

Figure 4.20 Comparison at the middle line on the bottom of the plate.

Moreover, another meshing scheme is presented. The response in the area

close to the external magnetic source is significant than other areas. And this means that the electromagnetic components vary greatly. To describe this uneven distribution, a refinement grid is supposed to assign for this area. As seen in Fig. 4.21, in addition to the refinement on the edge area, a finer grid is done for the areas which are closed to the current sources (*I* and -*I*). Similarly, the connection area is needed.

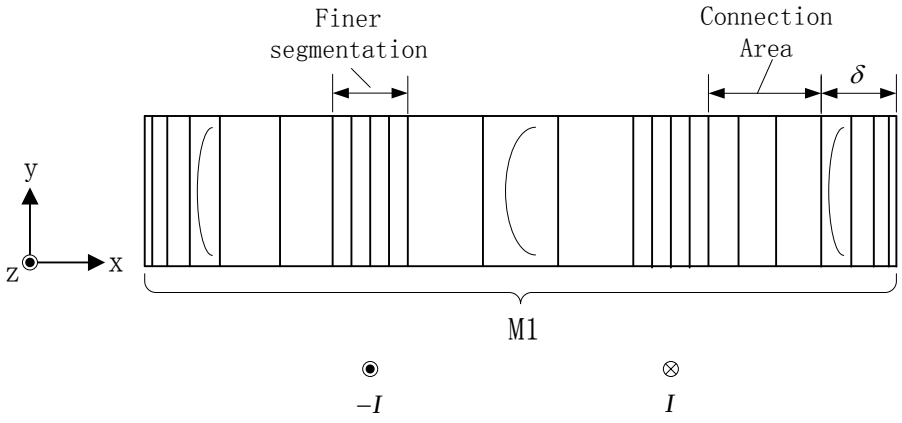

Figure 4.21 Mesh refinement corresponding to the external current sources.

4.7. A Hybrid PEEC Method

For the plate made from ferromagnetic material, as the response, the electromagnetic components vary singularly in edge area of the plate. In section 4.6, the mesh refinement for specific areas greatly improves the accuracy of the solution fields. However, note that the assumption of double exponential function is not accurate in the edge region of the magnetic plate, as seen in Fig. 4.18. Essentially, the mesh refinement just compress the error caused by this assumption, but not eliminates. In this section a new hybrid modeling method (named M3) will be presented, which is expected to essentially reduce this error.

From the exhibition in Fig. 4.18, it is clear that the electromagnetic

components (J_x, J_y, M_x, M_y) which are involved in the plane of the plate have smooth fluctuation during the total area. Although there is a little deviation in the edge area, it can be reduced by the implementation of mesh refinement in this area.

For the component (M_z) which is perpendicular to the plane of the plate, it has a gradual fluctuation among the most area but a dramatic change in the edge area. The mesh refinement for the edge area is less effective and costly. As mentioned in Chapter 3 that a higher density of grid will lead higher accuracy result based on the traditional volume cells. It means that enough number of volume cells can simulate the distribution of M_z in the edge area. Therefore, a hybrid mesh scheme will be applied for M_z. For the edge region, roughly estimated as the skin depth, the discretization of traditional volume cells is done. And for the rest most area, the double exponential expression is still employed.

The hybrid mesh scheme has two benefits: 1) the assumption of analytical expression distribution reduces the number of unknowns compared with M0; 2) the traditional volume cells applied for M_z in edge region improves the accuracy of solution.

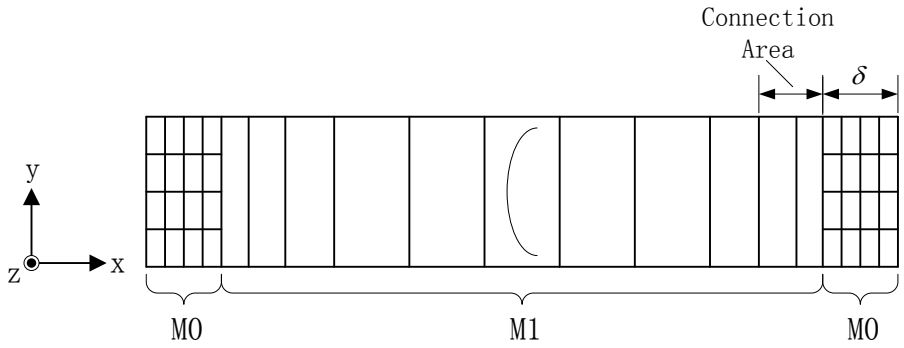

Figure 4.22 Meshing scheme of M3.

The new hybrid method is tested with the configuration presented in section 3.2. The results are compared with the M1, M1_R, and validated by the IES-FARADAY. As shown in Fig. 4.23, the results from M3 are very closer to the results from M1_R. The average error of induced current of M3 compared with BEM is less than 1%, and the largest value which is located on the boundary is 5.35%. For the magnetization, the accuracy is improved compared with M1. The average error is reduced from 5.87% to 2.8%, and the largest value is just 3.47%.

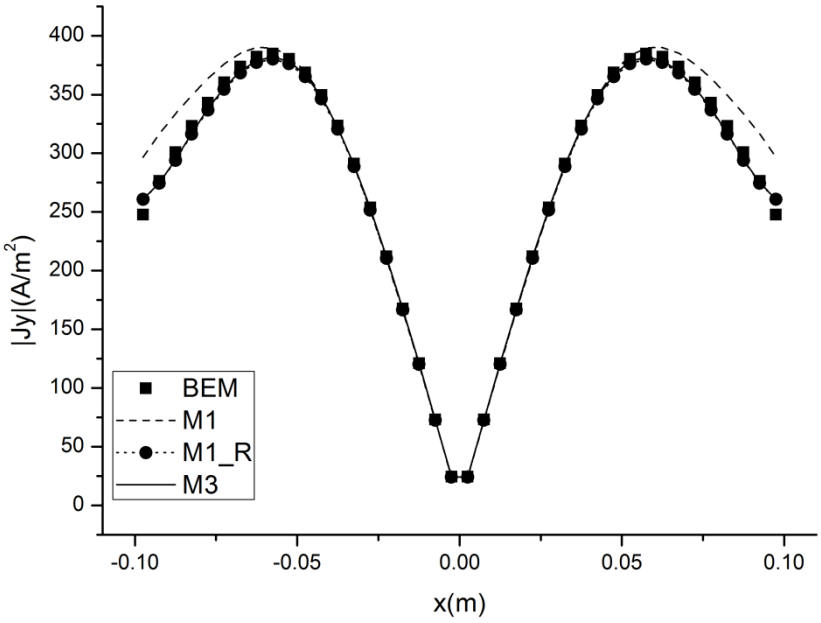

(a) Comparison of induced current density.

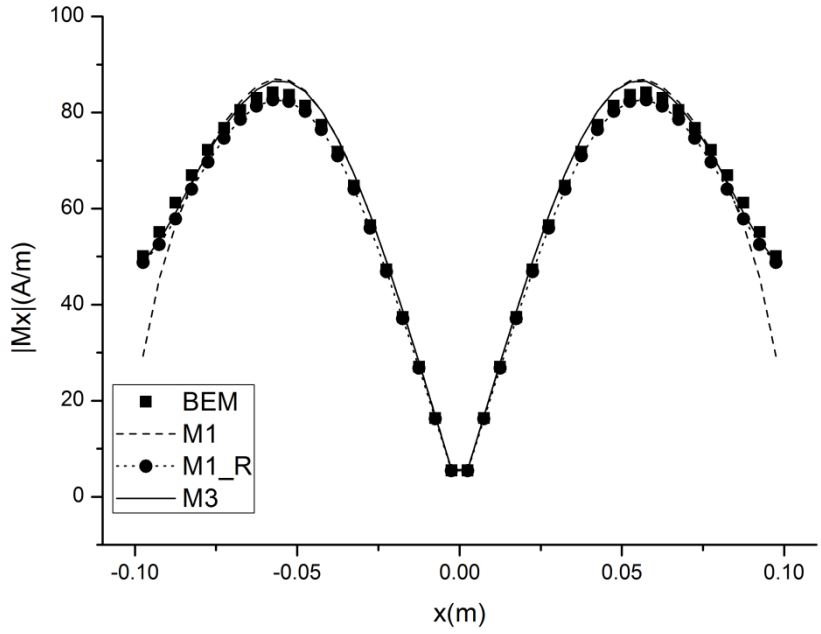

(b) Comparison of magnetization density.

Figure 4.23 Comparison of EM components between different methods.

4.8. Conclusion

In this chapter, a double exponential function is adopted to describe the distribution of the induced current and magnetization along the thickness of the plate. With this assumption, a new PEEC modeling method is presented and named M1. The plate can be then meshed into a set of volume current cells only along its width and length. These cells join together at the potential cells according to their topology. The circuit model and its correspond circuit parameters of a cell were developed using the electric current integral equation. As the discretization over the cross section of the plate is avoided, the total number of unknowns is significantly reduced.

This procedure has been tested using the model with a simple plate configuration. Both the current density on the plate and the resultant magnetic around the plate were calculated. The results were compared with that obtained using the IE method. It was found that the proposed procedure is efficient in solving the eddy-current or shielding problems with a large thin plate structure.

For improving the solution accuracy, the non-uniform meshing technique is presented for all the electromagnetic components. For the component which is perpendicular to the plate, the volume cells are assigned for the edge region. Then the hybrid numerical method (M3) is proposed. The numerical testing reflects that the assumption of double exponential function is effective and very efficient. The hybrid meshing scheme further improves the accuracy of PEEC model.

This numerical tool may be considered an extension of the traditional PEEC approach for solving low-frequency eddy-current/shielding problems of large plates, which is usually applied to three-dimensional multi-conductor systems in electronic systems. The proposed PEEC approach will broaden the spectrum of PEEC applications, and because the skin effect and magnetic properties of plate material have been taken into account, it will contribute to the solution of low-frequency EM problems where a strong skin effect exists in the plates.

5. Surface Elements of Magnetization

In this chapter, an extended PEEC formulation is proposed to model 3D metallic plates for magnetic shielding at low frequency. The plates are made of linear magnetic material, and exhibit induced current and magnetization current under the excitation of an external magnetic field. In the proposed PEEC formulation the volume current of magnetization is substituted with the induced current in the plate. An analytical function is then adopted for the induced current to avoid volume discretization on the plate. Circuit equations are then built up, and solved for both induced current and surface current of magnetization on the plate, subsequently the magnetic field around the magnetic plate. The proposed method was tested on a shielding structure made by a magnetic plate. A comparison of the results with the boundary-element-method (BEM) based software is presented finally.

5.1. The Problems in Above Models of Magnetization

The PEEC method or the equivalent circuit method has been proposed to solve shielding problems at low frequency. One challenging issues faced in its application for shielding is the non-uniform distribution of eddy current within the plate. For a shielding problem associated with 3D plates, a large number of elementary volume cells are required in order to improve the accuracy of its results. It is because volume currents of cells in the standard PECC formulation are assumed to be constant, as seen in method M0. This certainly requires a significant amount of computing resources for solving 3D shielding problems.

The novel technique of M1 has been proposed to deal with the current distribution over the cross section of the plate [6], and has been successfully applied to solve shielding problems associated with 3D conductive plates.

In both M0 and M1, the potential cells are the volume cells. Even a small plate can bring out a large number of cells. Besides that, since magnetization M_z is singular in the edge area and varies sharply in this area, the volume cell scheme cannot describe preciously the characteristic of M_z near the edge. Therefore, it is necessary to search an appropriate approach to represent the distribution of M_z accurately and to avoid big deviation in the area close to plate edges.

5.2. Magnetization

In the absence of an external magnetic field, the magnetic dipoles in a piece of material are oriented at random, as shown in Fig. 5.1(a). Thus, the net magnetic moment is nearly zero. In the presence of an external magnetic field, each magnetic dipole experiences a torque that tends to align it with the magnetic field, as illustrated in Fig. 5.1(b). The figure shows an ideal case of perfect alignment, but in reality, the alignment is only partial. The alignment of the magnetic dipoles is different with the electric dipoles. The alignment of the magnetic poles in paramagnetic and ferromagnetic materials increases the original magnetic field. The alignment of the magnetic dipoles within the material is equivalent to the current along the surface of the material, as depicted in Fig. 5.1(c). This current results in an additional magnetic field within the

material.

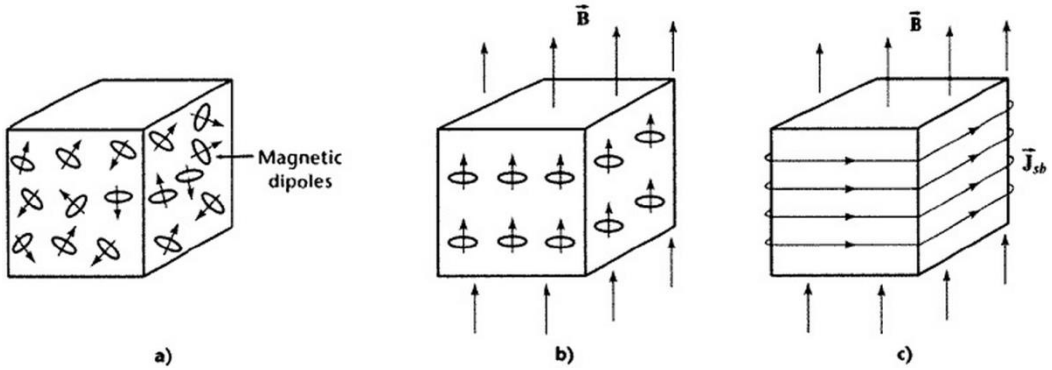

(a) A piece of magnetic material with randomly oriented magnetic dipoles; (b) An external field causes the magnetic dipoles to align with it; (c) The small aligned current loops of (b) are equivalent to a current along the surface of the material.

Figure 5.1 Magnetic polarization

When a finite volume of a magnetic material is considered, the global magnetic vector potential generated by the magnetic polarization is:

$$\boldsymbol{A}_m(\boldsymbol{r}) = \frac{\mu_0}{4\pi}\int_{v'} \boldsymbol{M}(\boldsymbol{r}')\times\nabla'\left(\frac{1}{R}\right)dv' \tag{5.1}$$

where $R = |\boldsymbol{R}| = |\boldsymbol{r}-\boldsymbol{r}'|$, $\boldsymbol{A_m}$ is the magnetic vector potential, and $\boldsymbol{M}$ is the magnetization density.

The use of vector identities allows to obtain a different representation of $\boldsymbol{A_m}$ which provides an interpretation in terms of surface currents:

$$\begin{aligned}\boldsymbol{A}_m(\boldsymbol{r}) &= \frac{\mu_0}{4\pi}\int_{v'}\frac{\boldsymbol{M}(\boldsymbol{r}')\times\boldsymbol{R}}{R^3}dv' \\ &= \frac{\mu_0}{4\pi}\int_{v'}\frac{\nabla\times\boldsymbol{M}(\boldsymbol{r}')}{R}dv' + \frac{\mu_0}{4\pi}\int_{S'}\frac{\boldsymbol{M}(\boldsymbol{r}')\times\boldsymbol{n}'}{R}dS'\end{aligned} \tag{5.2}$$

where $\boldsymbol{n}'$ is the unit vector of the surface element S'.

When the magnetic polarization is uniform inside the volume v' and the quasi-static approximation (delays negligible) is assumed, the first term in $\boldsymbol{A}_m$ is

identical to zero. As a consequence, the magnetic vector potential will be interpreted in terms of only surface current:

$$\boldsymbol{A}_m(\boldsymbol{r}) = \frac{\mu_0}{4\pi}\int_{S'} \frac{\boldsymbol{M}(\boldsymbol{r}')\times \boldsymbol{n}'}{R} dS' \tag{5.3}$$

This technique was adopted in [10]. However, magnetization is not always homogeneous within a body, but rather varies between different points. When the magnetic polarization is non-uniform inside the volume v', the volume current needs to be taken into account.

Note that the magnetization $\boldsymbol{M}$ makes a contribution to the current density $\boldsymbol{J}_m$ in the volume v', known as the magnetization current or bound current:

$$\boldsymbol{J}_m = \nabla \times \boldsymbol{M} \tag{5.4}$$

Then, the vector potential $\boldsymbol{A}_m(\boldsymbol{r})$ can be expressed further by:

$$\boldsymbol{A}_m(\boldsymbol{r}) = \frac{\mu_0}{4\pi}\int_{v'} \frac{\boldsymbol{J}_m(\boldsymbol{r}')dv'}{R} dv' + \frac{\mu_0}{4\pi}\int_{S'} \frac{\boldsymbol{M}(\boldsymbol{r}')\times \boldsymbol{n}'}{R} dS' \tag{5.5}$$

5.3. PEEC Model Based on Surface Elements of Magnetization

5.3.1. Vector Potential Using Surface Current of Magnetization

Electrical current $\boldsymbol{J}_c$ appears in a general PEEC formulation. From the Maxwell's Equations, there is a relation between electrical current $\boldsymbol{J}_c$ and the magnetic field $\boldsymbol{H}$, as follows:

$$\boldsymbol{J}_c = \nabla \times \boldsymbol{H} \tag{5.6}$$

In many materials, such as ferromagnetic, the response of the magnetization $\boldsymbol{M}$ in a diamagnet or paramagnet is approximately linear:

$$\boldsymbol{M} = \chi_m \boldsymbol{H} \tag{5.7}$$

where the constant χ_m of proportionality is the magnetic susceptibility of the material.

Thus, current density of magnetization $\boldsymbol{J_m}$ can be expressed in terms of electrical current density $\boldsymbol{J_c}$, as follow:

$$\boldsymbol{J_m} = \chi_m \nabla \times \boldsymbol{H} = \chi_m \boldsymbol{J_c} \tag{5.8}$$

and, because of $\chi_m = \mu_r - 1$,

$$\boldsymbol{J_m} = (\mu_r - 1)\boldsymbol{J_c} \tag{5.9}$$

Consequently, in the presence of magnetic material the total magnetic vector potential at a point $\boldsymbol{r}$ is given by:

$$\begin{aligned} &\boldsymbol{A_c}(\boldsymbol{r}) + \boldsymbol{A_m}(\boldsymbol{r}) \\ &= \frac{\mu_0}{4\pi}\int_{v'}\frac{\boldsymbol{J_c}(\boldsymbol{r}')}{R}dv' + \frac{\mu_0}{4\pi}\int_{v'}\frac{\boldsymbol{J_m}(\boldsymbol{r}')}{R}dv' + \frac{\mu_0}{4\pi}\int_{S'}\frac{\boldsymbol{M}(\boldsymbol{r}')\times\boldsymbol{n}'}{R}dS' \\ &= \frac{\mu_0\mu_r}{4\pi}\int_{v'}\frac{\boldsymbol{J_c}(\boldsymbol{r}')}{R}dv' + \frac{\mu_0}{4\pi}\int_{S'}\frac{\boldsymbol{M}(\boldsymbol{r}')\times\boldsymbol{n}'}{R}dS' \end{aligned} \tag{5.10}$$

The two updated items of vector potential are as follows:

$$\boldsymbol{A_c}'(\boldsymbol{r}) = \frac{\mu_0\mu_r}{4\pi}\int_{v'}\frac{\boldsymbol{J_c}(\boldsymbol{r}')}{R}dv' \tag{5.11}$$

$$\boldsymbol{A_m^S}(\boldsymbol{r}) = \frac{\mu_0}{4\pi}\int_{S'}\frac{\boldsymbol{M}(\boldsymbol{r}')\times\boldsymbol{n}'}{R}dS' \tag{5.12}$$

This indicates that the effect of magnetization current inside the magnetic material can be taken into account by using the induced current in an infinite magnetic medium. As a result, the electrical equation is established with two types of unknowns: induced current density and surface current density of magnetization. Fig. 5.2 illustrates both induced current density and surface current density of magnetization within a magnetic plate. With the constitutive

relation (4b), these unknowns can be obtained directly using traditional circuit analysis tools.

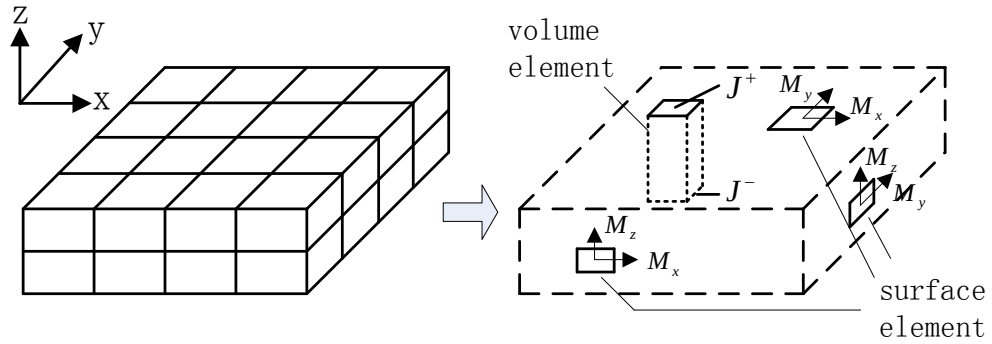

Figure 5.2 Volume elements for induced current and surface elements for surface current of magnetization.

Then, using the vector identity:

$$\nabla\times(f\boldsymbol{F})=\nabla f\times\boldsymbol{F}+(\nabla\times\boldsymbol{F})f \tag{5.13}$$

The magnetic flux contributed by magnetization at a point in the space is expressed as:

$$\begin{aligned}\boldsymbol{B}(\boldsymbol{r})&=\nabla\times\boldsymbol{A}(\boldsymbol{r})\\&=\frac{\mu_0}{4\pi}\int_{\tau'}\frac{\boldsymbol{J}_m(\boldsymbol{r}')\times\boldsymbol{R}}{R^3}d\tau'+\frac{\mu_0}{4\pi}\int_{S'}\frac{\boldsymbol{K}_m(\boldsymbol{r}')\times\boldsymbol{R}}{R^3}dS'\end{aligned} \tag{5.14}$$

where

$$\boldsymbol{J}_m(\boldsymbol{r}')=\nabla'\times\boldsymbol{M}(\boldsymbol{r}') \tag{5.15}$$

$$\boldsymbol{K}_m(\boldsymbol{r}')=\boldsymbol{M}(\boldsymbol{r}')\times\boldsymbol{n}' \tag{5.16}$$

5.3.2. Discretization of the Plate

The discretization of a plate is required for both volume electric current and surface current of magnetization. First of all, the plate is divided into a number of surface cells over its six surfaces with numbers (N_x+1, N_y+1, N_z+1) of grid lines in x, y and z directions, as illustrated in Fig. 5.3(a). The total number of

surface cells is $N_m^S = 2(N_x N_y + N_x N_z + N_y N_z)$. These cells are introduced for defining surface density of magnetization ($\boldsymbol{M} \times \boldsymbol{n}$).

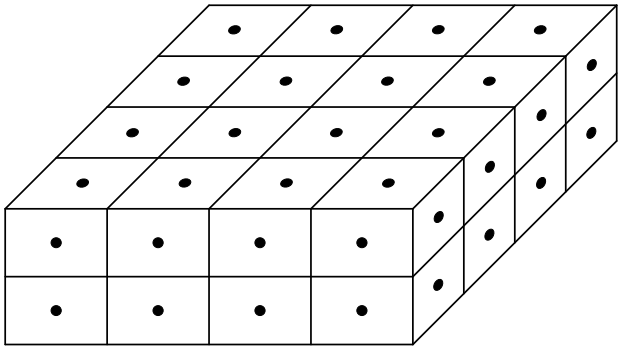

(a) Surface elements of magnetization

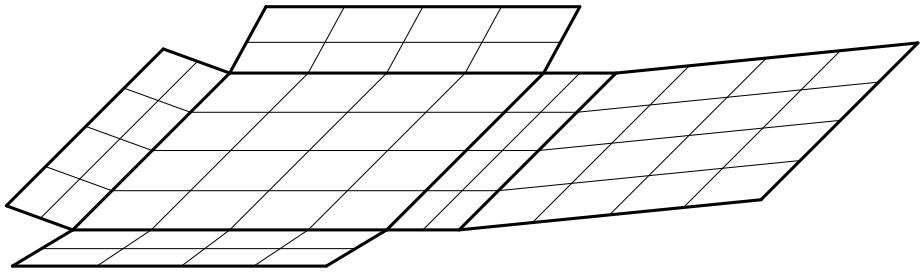

(b) Segmentation on the surfaces of a magnetic plate for magnetization

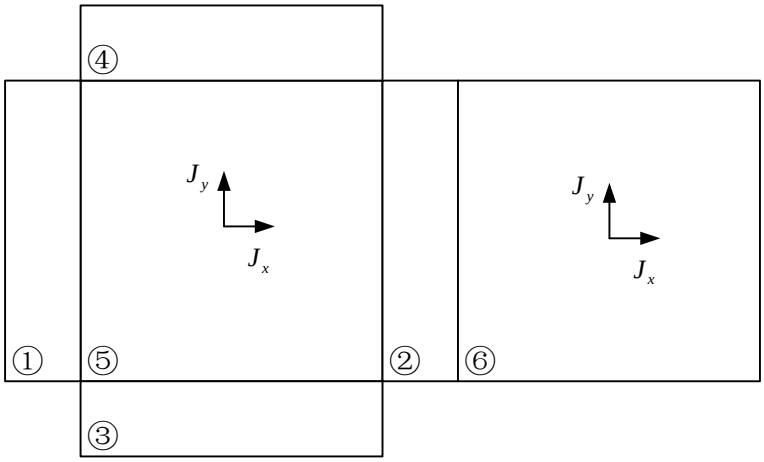

(c) Mark for surfaces and the distribution of electric currents

Figure 5.3 Discretization and the elementary cells of the plate.

The electric current flows in the x-y plane only. The potential cell is then formed by taking the volume between two opposite surface cells in the x-y plane,

as illustrated in Fig. 5.3(c). Then, current cells are formed by taking the volume between the centre points of these adjacent potential cells. The current cells on the plate are classified into two types, which carry the currents in two orthogonal directions. These cells are named X cells and Y cells. The numbers of X cells and Y cells are $NX = (N_x - 1)N_y$ and $NY = N_x(N_y - 1)$, respectively.

5.3.3. New PEEC Model for Magnetic Plate

With the proposed meshing, the PEEC model can be built up in the form of a set of branch equations. The branch voltage defined in Eq. (2.14) can be rewritten, as follow:

$$\begin{aligned} &\frac{l_i}{\sigma}\bullet \boldsymbol{J}_{c,i}(z) + \frac{j\omega\mu_0\mu_r}{4\pi}\sum_{j=1}^{N_c}\int_{l_i}\int_{v_j'}\frac{\boldsymbol{J}_{c,j}(z')}{R}dv'dl + \\ &\frac{j\omega\mu_0}{4\pi}\sum_{j=1}^{N_m^S}\int_{l_i}\int_{S_j'}\frac{\boldsymbol{M}_j\times\boldsymbol{n}'}{R}dS'dl + V_i \\ &= \frac{j\omega\mu_0}{4\pi}\sum_{j=1}^{N_s}\int_{l_i}\int_{l_j'}\frac{\boldsymbol{I}_{s,j}}{R}dl'dl \end{aligned} \tag{5.17}$$

where N_c, N_m^S, N_s represent the numbers of induced current cells, magnetization cells and source wires, respectively.

The constitutive relation given in Eq. (2.17) introduces additional equations for surface density of magnetization $\boldsymbol{M}\times\boldsymbol{n}$ at any node, as follow:

$$\begin{aligned} &\frac{\mu_0\mu_r}{4\pi}\sum_{j=1}^{N_c}\int_{v_j'}\frac{\nabla\times\boldsymbol{J}_{c,j}(z')dv'}{R} \\ &+\frac{\mu_0}{4\pi}\sum_{j=1}^{N_m^S}\int_{S_j'}\frac{\nabla\times(\boldsymbol{M}_j\times\boldsymbol{n}')}{R}dS' - \frac{\mu_0\bullet\mu_r}{\mu_r-1}\boldsymbol{M}(\boldsymbol{r}) \\ &=\frac{\mu_0}{4\pi}\sum_{j=1}^{N_s}\int_{l_j'}\frac{\nabla\times\boldsymbol{I}_{s,j}}{R}dl' \end{aligned} \tag{5.18}$$

Both $\boldsymbol{J}_{c,i}$ and $\boldsymbol{M}_i \times \boldsymbol{n}$ can be solved for directly using traditional circuit techniques. With known $\boldsymbol{J}_{c,i}$ and $\boldsymbol{M}_i \times \boldsymbol{n}$ on the plate, it is possible to evaluate the resultant field around the plate, which is contributed by the excited source current, the induced current and surface current of magnetization. The resultant magnetic field $\boldsymbol{B}$ around the plate is given, as follow:

$$\begin{aligned}\boldsymbol{B}(\boldsymbol{r}) = \frac{\mu_0 \mu_r}{4\pi} \sum_{j=1}^{N_c} \int_{v_j'} \frac{\nabla \times \boldsymbol{J}_{c,j}(z')}{R} dv' + \frac{\mu_0}{4\pi} \sum_{j=1}^{N_s} \int_{l_j'} \frac{\nabla \times \boldsymbol{I}_{s,j}}{R} dl' \\ + \frac{\mu_0}{4\pi} \sum_{j=1}^{N_m^S} \int_{S_j'} \frac{\nabla \times (\boldsymbol{M}_j \times \boldsymbol{n}')}{R} dS'\end{aligned} \tag{14}$$

5.4. Numerical Investigation

For numerical validation, the simple shielding structure is investigated in this paper, as shown in Fig. 3.9. The thin plate is made from linear magnetic materials with the conductivity of $\sigma = 0.75 \times 10^7 S/m$ and the relative permeability of $\mu_r = 200$. It is a square plate with the side length of $w = 200mm$ and the thickness of $d = 2mm$. The external source is a filamentary conductive square loop with the side length of $D = 100mm$ running in parallel with the plate. It is located in the centre with the separation distance of 50mm from the plate. The source loop carries an a.c. current of $I = 1A$ at the frequency of $f = 50Hz$.

The proposed method (M2) has been run on the platform of MATLAB. Two different meshing schemes (PM1 and PM2) were considered for the simulation. PM1 is a uniform meshing scheme with $N_x = 30$, $N_y = 30$, and $N_z = 4$. Considering strong non-uniform distribution of induced current and surface current of magnetization, fine meshing around the edges of the plate was adopted in PM2, that is, $N_x = 44$, $N_y = 44$ and $N_z = 4$. For comparison, the results

computed by the commercial software based on Boundary Element Method (BEM) are presented as well. Similarly, two grid sizes have been implemented for using BEM: BEM1 ($N_x = 30$, $N_y = 30$, $N_z = 4$) and BEM2 ($N_x = 40$, $N_y = 40$, $N_z = 4$).

Considering the geometrical symmetry of the structure under investigation, a quarter of the structure was modeled in the simulation by using these two different methods (the detail is presented in Chapter 6). The requirements for computer resources were relaxed significantly. The information of the computer used for the simulation is given, as follows:

- CPU: Intel(R) Pentium(R) 4, 2.00GHz
- Memory: 2.00GB of RAM

The computation information is given in Table 5.1. It is clearly that the computation time for the proposed method is much less than the software. Note that no particular optimization procedure was taken in the program for the proposed method running on the Matlab platform.

TABLE 5.1 Number of Unknowns and Computation Time

	PM1	**PM2**	**BEM1**	**BEM2**
Elements in total	570	1144	570	960
Unknowns	2040	4224	3010	5010
Computation time	3’36’’	16’38’’	32’22’’	54’

The resultant magnetic field was calculated by both methods on a line above the plate. It runs in parallel with the diagonal line of the plate at the height of 50mm. The results are compared in Fig. 5.4. It is noted that the field curves

obtained from two different methods match well generally. Relatively large difference is observed in the central area of the plate. With less dense meshing schemes (PM1 and BEM1), the maximum difference is found to be 3.7% at the central point of the plate. With more dense meshing schemes (PM2 and BEM2), the maximum difference is reduced to be less than 1% at the same location. Reduction of the difference is contributed by the improvement of results in both BEM and PM (e.g., 50% reduction in BEM and 50% in PM).

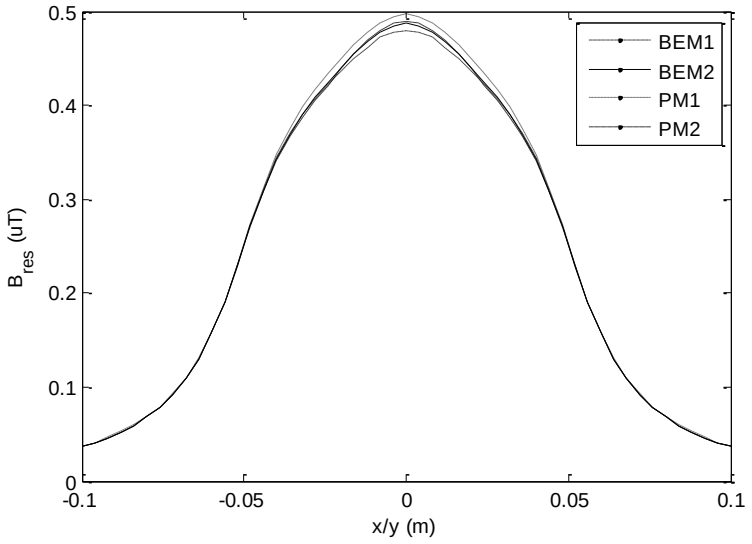

Figure 5.4 Resultant magnetic field on a diagonal line above the plate (z=100mm).

5.5. Conclusion

In this section, an extended PEEC model based on the surface elements of magnetization was proposed. In the presence of linear magnetic material, circuit equations and constitutive relation equations were set up using both volume induced current and surface current of magnetization. The volume current of magnetization is substituted by the induced current. This approach avoids volume meshing for magnetization, and improves the accuracy of simulation. A double

exponential function analytical expression is adopted for the current density to avoid the discretization along the thickness of the plate, subsequently reduces number of the unknowns greatly. A testing example was presented for validating the proposed method with the commercial software. It was found that the resultant magnetic fields obtained from these two methods match well. The computation time is significantly less than that required by the BEM when the similar meshing size was adopted in the simulation.

6. The Techniques for Reduction of PEEC Unknowns

In above chapters, the PEEC method has been developed to deal with the electromagnetic problems with the structures of wires and plates. It has the capability to generate the models of the interconnected structure in the form of an electrical circuit. This allows a better understanding of the shielding behavior using circuit concepts.

However, when using this method for a large 3D problem, the number of unknowns would be significantly large due to volume discretization [6]. The research on minimizing model complexity in order to reduce solution time is particularly interesting. Reduction of unknowns in a PEEC model is one of the most popular approaches.

In this chapter, two techniques for reducing the number of PEEC unknowns for 3D metal plates in magnetic shielding are presented, that is, loop analysis technique and modeling technique for symmetrical shielding structure. Firstly, the loop analysis approach is developed to combine the electric field integral equations set up for the branches along different orthogonal directions. The branches are merged into loops and the unknown of electrical potential is eliminated. According to the pattern of eddy current distribution on the plate, the induced current components (J_x, J_y) can be expressed by each other. Then the variable set is compressed to a reduced set with one variable only (J_x, J_y , or a new variable - loop current I).. Secondly, according to the pattern of both eddy current distribution and magnetization distribution in the plate, symmetric

and/or anti-symmetric properties in a shielding problem can be identified. The set of system equations can be further reduced by these symmetrical and anti-symmetric properties. The reduced set of system equations will then be solved efficiently.

6.1. Loop Analysis Techniques

6.1.1. Variable Elimination

For simplicity of discussion, the general matrix equation (3.29) given in Chapter 3 for a shielding structure made of linear magnetic/conductive materials is presented below:

$$\begin{bmatrix} \mathbf{L_x} & \mathbf{0} & \mathbf{C}_x^t & \mathbf{Q_x} \\ \mathbf{0} & \mathbf{L_y} & \mathbf{C}_y^t & \mathbf{Q_y} \\ \mathbf{C_x} & \mathbf{C_y} & \mathbf{0} & \mathbf{0} \\ \mathbf{T_x} & \mathbf{T_y} & \mathbf{0} & \mathbf{P} \end{bmatrix} \begin{bmatrix} \mathbf{J_x} \\ \mathbf{J_y} \\ \mathbf{\Phi} \\ \mathbf{M} \end{bmatrix} = \begin{bmatrix} \mathbf{U_x^s} \\ \mathbf{U_y^s} \\ \mathbf{0} \\ \mathbf{B_s} \end{bmatrix} \tag{6.1}$$

The matrix equation (6.1) can be solved uniquely for induced current densities ($\mathbf{J_x}$ and $\mathbf{J_y}$), potential $\mathbf{\Phi}$ and magnetization density ($\mathbf{M_x}$, $\mathbf{M_y}$ and $\mathbf{M_z}$). Excluding an electric scalar potential for reference node, the number of unknowns for the variables $\mathbf{\Phi}$, $\mathbf{J_x}$, $\mathbf{J_y}$, and $\mathbf{M}$ are $N_\varphi = N_x N_y - 1$, $N_{cx} = (N_x - 1) \bullet N_y$, $N_{cy} = N_x \bullet (N_y - 1)$ and $N_m = 3N_x N_y$, respectively. Therefore, the total number of unknowns in (6.1) is equal to $N_{tot} = 6N_x \bullet N_y - N_x - N_y - 1.$

It is noted that scalar potential $\mathbf{\Phi}$ is not necessary in calculating the resultant magnetic field, and that there are a considerable number of zeros in the matrix. This leads to a very large system matrix equation, and wastes computer

resources significantly.

Moreover, the eddy current circulates within the plate and the orthogonal eddy current components are not independent. Different components can be expressed by each other. There is a possibility of combining these current components or replacing these components with a new variable. At the same time the unknowns of electric potential $\mathbf{\Phi}$ are eliminated.

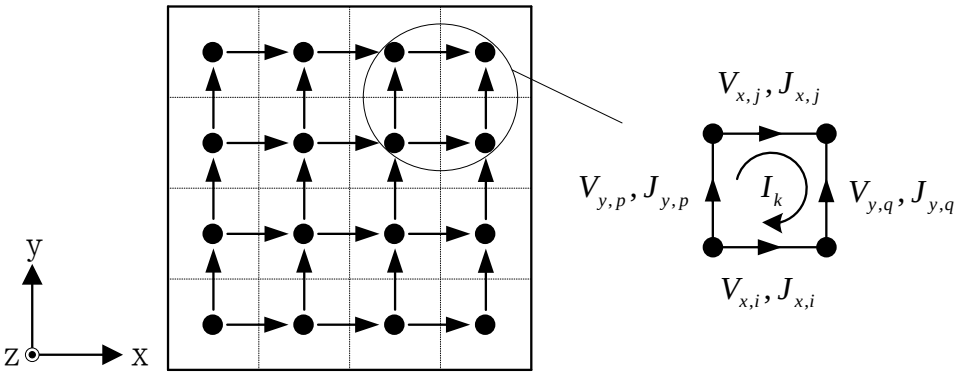

Figure 6.1 Closed loop formed by X/Y branches.

As shown in Fig. 6.1, a closed loop is formed with four adjacent branches. Potential difference for each branch is determined by all loop currents on the plate. The total potential difference along the loop is identically zero, that is:

$$V_{x,i} + V_{x,j} + V_{y,p} + V_{y,q} = 0 \tag{6.2}$$

Voltage equations for these branches are already available in (6.1). Substituting the corresponding branch equations of Eq. (6.1) to (6.2) yields a loop equation:

$$\begin{aligned}&(\mathrm{L_{x,i}} - \mathrm{L_{x,j}})\mathbf{J}_\mathrm{x} + (\mathrm{L_{y,q}} - \mathrm{L_{y,p}})\mathbf{J}_\mathrm{y} + (\mathrm{Q_{x,i}} - \mathrm{Q_{x,j}} - \mathrm{Q_{y,p}} + \mathrm{Q_{y,q}})\mathbf{M} \\ &= \mathrm{U_{sx,i}} - \mathrm{U_{sx,j}} - \mathrm{U_{sy,p}} + \mathrm{U_{sy,q}}\end{aligned} \tag{6.3}$$

From Eq. (3.11) of the KCL relation, $\mathbf{J}_\mathbf{x}$ and $\mathbf{J}_\mathbf{y}$ can be expressed by each other, as follow

$$\mathbf{J_y} = -\mathbf{C_x}^{-1} \bullet \mathbf{C_y} \bullet \mathbf{J_x} \tag{6.4}$$

Eq. (6.3) can be rewrote as follow

$$\begin{aligned}&[(L_{x,i} - L_{x,j}) - (L_{y,q} - L_{y,p}) \bullet \mathbf{C_y}^{-1} \bullet \mathbf{C_x}] \bullet \mathbf{J_x} + (Q_{x,i} - Q_{x,j} - Q_{y,p} + Q_{y,q})\mathbf{M} \\ &= U_{sx,i} - U_{sx,j} - U_{sy,p} + U_{sy,q}\end{aligned} \tag{6.5}$$

As a result, the adjacent four X/Y branches can be integrated to one circuit loop, the variables of $\mathbf{J_y}$ and $\mathbf{\Phi}$ in Eq. (6.1) can be substituted with one variable $\mathbf{J_x}$, and (6.1) can be written as:

$$\begin{bmatrix} \mathbf{L_x^*} & \mathbf{Q^*} \\ \mathbf{B^*} & \mathbf{P} \end{bmatrix} \begin{bmatrix} \mathbf{J_x} \\ \mathbf{M} \end{bmatrix} = \begin{bmatrix} \mathbf{U_{s,loop}} \\ \mathbf{B_s} \end{bmatrix} \tag{6.6}$$

where $\mathbf{U_{s,loop}}$ is the excitation on the loop by external current source. The total number of unknowns in Eq. (6.6) is equal to $N_{tot} = 4N_x \bullet N_y - N_y$.

This procedure provides an automatic conversion algorithm for reducing the set of system equations in which only one variable *Jx* retains and the unknown of electrical potential is eliminated completely.

6.1.2. Loop Current

In some cases, a generalized loop current is introduced to establish system equation for the induced current problem. As seen in Fig. 6.2, four adjacent nodes are connected by four current cells, which include two X-cells and two Y-cells. The relationship between the loop current and the current densities carried in the four cells is as follow:

$$I_k = -J_{x,i} \bullet w_{x,i} = J_{x,j} \bullet w_{x,j} = J_{y,p} \bullet w_{y,p} = -J_{y,q} \bullet w_{y,q} \tag{6.7}$$

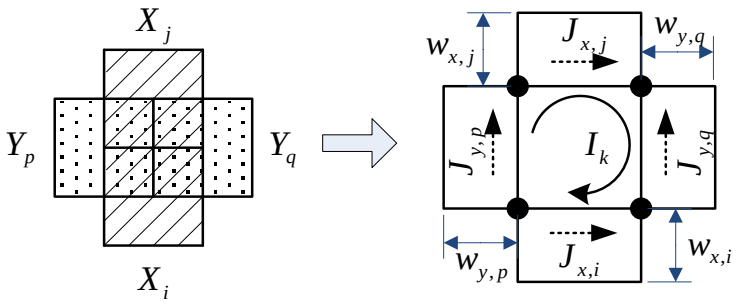

Figure 6.2 The relationship between loop current and X/Y cells.

After introducing loop current I on the plate (I_k for loop k in Fig. 6.2), both J_x and J_y can be expressed by:

$$\mathbf{J_x} = \mathbf{C}_x^{'}\mathbf{I}, \quad \mathbf{J_y} = \mathbf{C}_y^{'}\mathbf{I} \tag{6.8}$$

where $\mathbf{C}_x^{'}$ and $\mathbf{C}_y^{'}$ are the modified nodal incidence matrices by including current cell width in the entry for that current cell.

There are two benefits: 1) the set of two induced current variables have been compressed to one variable; 2) the relationship between X/Y cells has been merged in the transformation to loop current. As a result, the Eq. (6.3) can be rewritten as:

$$\begin{aligned}&[(\mathrm{L_{x,i}}-\mathrm{L_{x,j}})\mathbf{C}_x^{'}+(\mathrm{L_{y,q}}-\mathrm{L_{y,p}})\mathbf{C}_y^{'}]\mathbf{I}+(\mathrm{Q_{x,i}}-\mathrm{Q_{x,j}}-\mathrm{Q_{y,p}}+\mathrm{Q_{y,q}})\mathbf{M}\\&=\mathrm{U_{sx,i}}-\mathrm{U_{sx,j}}-\mathrm{U_{sy,p}}+\mathrm{U_{sy,q}}\end{aligned} \tag{6.9}$$

The matrix equation with loop current **I** as the unknown is then given by:

$$\begin{bmatrix}\mathbf{L_{loop}} & \mathbf{Q_{loop}}\\ \mathbf{B_{loop}} & \mathbf{P}\end{bmatrix}\begin{bmatrix}\mathbf{I}\\ \mathbf{M}\end{bmatrix}=\begin{bmatrix}\mathbf{U_{s,loop}}\\ \mathbf{B_s}\end{bmatrix} \tag{6.10}$$

As loop number is equal to $(N_x-1)\times(N_y-1)$, the number of total unknowns in matrix (6.10) is reduced to $4N_xN_y-N_x-N_y-1$.

6.2. Modeling for Symmetrical Structures

In some structures, the electromagnetic components distributed inside and on

the surface of the plates are symmetrical or anti-symmetrical with respective to the x, y or z axis in a Cartesian coordinate system. Solve the total electromagnetic components for the plates without taking into these symmetric or anti-symmetric properties is a waste of computing resources and unnecessary. For a symmetrical shielding structure, only a part of the structure needs to be taken into account. For example, as shown in Fig. 6.3, the structure is symmetric to the z-axis, that is, the electromagnetic components inside and on the surface of the plate is anti-symmetrically. Therefore, we can pick up a quarter of the plate for setting up the PEEC model. The unknowns will be reduced to 1/4, and the solution matrix will be reduced to 1/16.

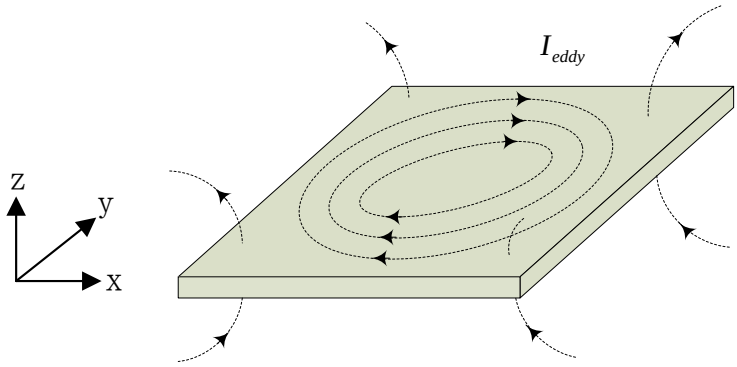

Figure 6.3 Distribution of electromagnetic components around the plate.

Long power lines are commonly fixed in buildings, the magnetic shielding at power frequency for them is valuable. During the shielding structures by metal plates, two typical cases are introduced in Fig. 4. Reference to the plate, the source line is parallel in case A and perpendicular in case B. Obviously, there exists symmetric and anti-symmetric patterns for the distribution of eddy current and magnetization in the plate. Electromagnetic components in some parts of the

structure have the same amplitude but different symbol. On the other hand, since the overall structure is modeled as interconnected and coupled circuit components, some sub-matrixes of the coefficient matrix in Eq. (12) can be folded and recombined. Then both the number of unknowns and the size of the solution matrix will be reduced greatly.

Long power lines are commonly found in buildings. The magnetic shielding at power frequency against these lines is necessary. For the shielding structures made by metal plates, two typical cases are introduced in Fig. 4. With reference to the plate, the source line is parallel in case A and perpendicular in case B. Obviously, there exists symmetric and anti-symmetric patterns for the distribution of eddy current and magnetization in the plate. Electromagnetic components in some parts of the structure have the same amplitude but opposite phase angle. On the other hand, since the overall structure is modeled as interconnected and coupled circuit components, some sub-matrixes of the coefficient matrix in Eq. (12) can be folded and recombined. Then both the number of unknowns and the size of the solution matrix will be reduced greatly.

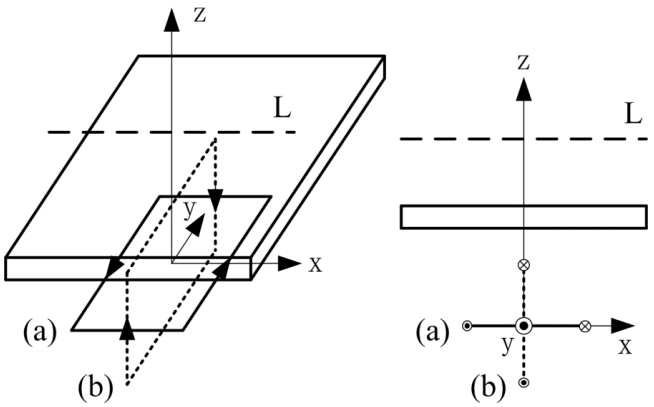

Figure 6.4 Configurations of a wire-plate structure.

In both case A and case B, the source lines can be treated as current loops and the excited magnetic field can be described in Fig. 5. The plate can be then divided into four parts with unique field pattern in each part. According to the distribution of magnetic field, the relationship of eddy current and magnetization distributed on different parts can be analyzed separately.

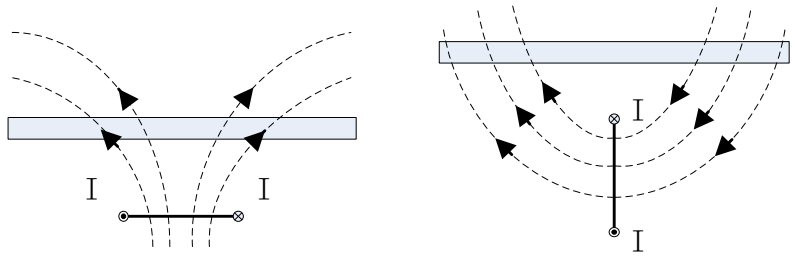

(a) Case A. (b) Case B.

Figure 6.5 Distribution of magnetic field in the two cases.

6.2.1. Modeling for Eddy Current

The current distribution in a plate is determined by the orientation of a current source. Note from the Faraday's law that the induced current flows in such a way that its magnetic field is opposite to the source field. The patterns of the current distribution in two cases can then be obtained, as shown in Fig. 6.6. In Fig. 6.6 both L1 and L2 are either the symmetrical or anti-symmetrical plane, perpendicular to the plate surface, and divide the plate into four parts. Table 1 presents a summary of the symmetrical properties of current components in the plate.

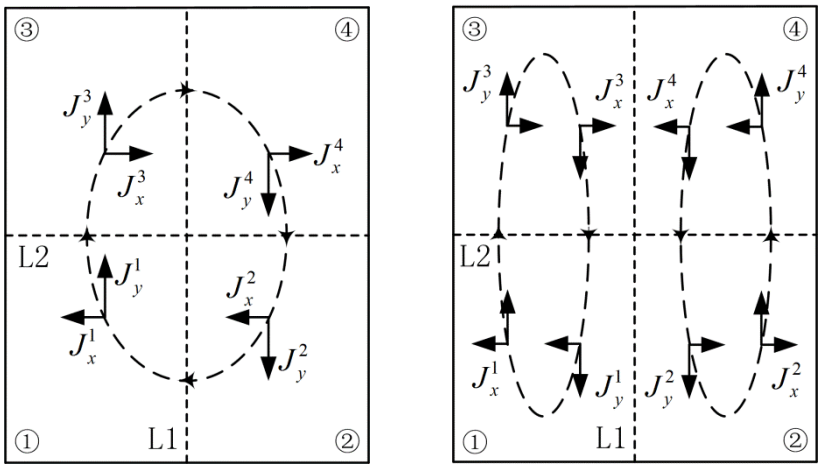

(a) Case A. (b) Case B.

Figure 6.6 Relationship of eddy current distributed on different parts.

Table 6.1 Symmetrical properties of current density and magnetization density.

Symmetrical plane	J_x or J_y		M_x, M_y or M_z	
	L1	L2	L1	L2
Case A	anti-sym.	anti-sym.	sym.	sym.
Case B	sym.	anti-sym.	anti-sym.	sym.

For case A, the induced current flows across both L1 and L2. The relationship among these orthogonal components in four parts is given by:

$$\begin{aligned} J_x^1 &= J_x^2 = -J_x^3 = -J_x^4 \\ J_y^1 &= -J_y^2 = J_y^3 = -J_y^4 \end{aligned} \tag{6.11}$$

For case B, two current loops are formed in the two parts separately, and there is no current crossover L1. The following relationship is obtained:

$$\begin{aligned} J_x^1 &= -J_x^2 = -J_x^3 = J_x^4 \\ J_y^1 &= J_y^2 = J_y^3 = J_y^4 \end{aligned} \tag{6.12}$$

As illustrated in Table 6.1 and Eq. (6.11) or (6.12), the current components in corresponding cells of these four parts either are identical or negatively identical. Therefore, only one part of the plate needs to be modeled for problem solving.

Accordingly, the voltage equation on branch *i* given in Eq. (6.1) is expressed by the current components in four parts, as follows:

$$\left[\mathrm{L}^1_{\mathrm{x,i}}\ \ \mathrm{L}^2_{\mathrm{x,i}}\ \ \mathrm{L}^3_{\mathrm{x,i}}\ \ \mathrm{L}^4_{\mathrm{x,i}}\right]\left[\mathbf{J}^1_{\mathrm{x}}\ \ \mathbf{J}^2_{\mathrm{x}}\ \ \mathbf{J}^3_{\mathrm{x}}\ \ \mathbf{J}^4_{\mathrm{x}}\right]^{\mathrm{T}} + \mathrm{Q}^1_{\mathrm{x,i}}\mathbf{M} + \mathrm{V}^1_{\mathrm{x,i}} = \mathrm{U}^1_{\mathrm{sx,i}} \tag{6.13}$$

In Eq. (6.13) $\mathbf{J}^2_{\mathrm{x}}\ \mathbf{J}^3_{\mathrm{x}}\ \mathbf{J}^4_{\mathrm{x}}$ can be substituted by $\mathbf{J}^1_{\mathrm{x}}$ using the symmetrical properties. Elements in (6.13) are then merged to form a modified equation with a reduced set of unknowns:

$$(\mathrm{L}^1_{\mathrm{x,i}} + \mathrm{L}^2_{\mathrm{x,i}} - \mathrm{L}^3_{\mathrm{x,i}} - \mathrm{L}^4_{\mathrm{x,i}})\bullet\mathbf{J}^1_{\mathrm{x}} + \mathrm{Q}^1_{\mathrm{x,i}}\bullet\mathbf{M} + \mathrm{V}^1_{\mathrm{x,i}} = \mathrm{U}^1_{\mathrm{sx,i}} \tag{6.14}$$

for Case A. Repeating the merging process for all branch equations and applying the procedure described in Section 6.1 yield a reduced matrix equation, as follows:

$$\begin{bmatrix} \mathbf{L}^{11}_{\mathrm{loop}} & \mathbf{Q}^{1,*}_{\mathrm{loop}} \\ \mathbf{B}^{*,1}_{\mathrm{loop}} & \mathbf{P} \end{bmatrix}\begin{bmatrix} \mathbf{I}^1_{\mathrm{loop}} \\ \mathbf{M} \end{bmatrix} = \begin{bmatrix} \mathbf{U}^1_{\mathrm{s,loop}} \\ \mathbf{B}_{\mathrm{s}} \end{bmatrix} \tag{6.15}$$

The matrix equation for Case B can be derived in a similar way. The number of unknown loop currents in (6.15) is now reduced to $N_x \bullet N_y / 4$ from $N_x \bullet N_y$.

6.2.2. Boundary Conditions

When a symmetrical or anti-symmetrical plane is adopted in plate modeling, it is necessary to apply boundary conditions on these planes for obtaining a modified matrix equation. As shown in Fig. 6.7, in both case A and case B, the x-z plane and y-z plane are the planes of symmetry. There exists eddy current across the x-z and y-z symmetrical planes in case A, but does not go through the y-z symmetrical plane in case B. This means that, the eddy current across both the x-z plane and y-z plane should be taken into account in case A, and the latter is not necessary to consider in case *B*.

Fig. 6.7 shows two different scenarios of the boundary; (i) current cells do not cross over the plane (La), and (ii) current cells cross over the plane (Lb). In Case (i), no current loop crosses over the boundary. In Case (ii), no current loop exists over the boundary if one of the current components is symmetrical to the plane (e.g., L1 in Case B). The matrix equation remains unchanged in these two cases. If both J_x and J_y are anti-symmetrical as shown in Case (ii), the potential on both sides is anti-symmetrical. A current loop does exist over the boundary, as shown in Fig. 6.7. The loop equation is revised by using the branch equations in Part only, as follows:

$$-\Delta V_{x,i} + \Delta V_{x,j} + 2\Delta V_{y,p} = 0 \tag{6.16}$$

With (6.16) the matrix equation in (6.15) is further updated by using the same technique presented early.

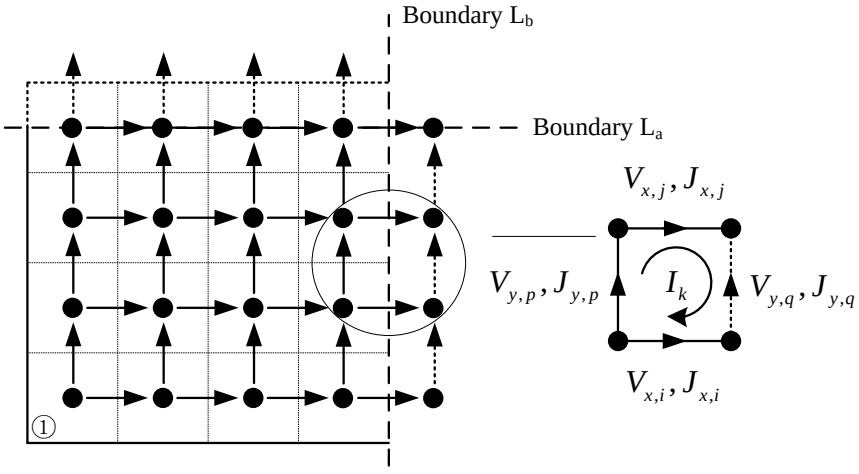

Figure 6.7 Different boundary approaches for the two cases.

6.2.3. Modeling for Magnetization

In a magnetic plate excited by an external magnetic field, the atomic currents are aligned so that the magnetic field is opposite to the source field outside the

plate. Inside the plate, it has a similar pattern as the source field for field enhancement [11]. Using the modeling technique for symmetrical induced current, only one part of the part needs to be considered for modeling the magnetization distributed on the full plate.

For two source orientations shown in Fig. 6.4, the distribution patterns of magnetization density are given in Fig. 6.8. Four symmetrical or anti-symmetrical parts are identified with two orthogonal planes L1 and L2 perpendicular to the plate surface. For case A, the wire frame is parallel to the plate, the magnetic lines pass through the metal plate perpendicularly, the orthogonal magnetization components on different parts are described in Fig. 6.8, and the relationship is given, as follows:

$$\begin{aligned} M_x^1 &= -M_x^2 = M_x^3 = -M_x^4 \\ M_y^1 &= M_y^2 = -M_y^3 = -M_y^4 \\ M_z^1 &= M_z^2 = M_z^3 = M_z^4 \end{aligned} \tag{6.17}$$

For case B, the relationship among these orthogonal components is given by

$$\begin{aligned} M_x^1 &= M_x^2 = M_x^3 = M_x^4 \\ M_y^1 &= -M_y^2 = -M_y^3 = M_y^4 \\ M_z^1 &= -M_z^2 = M_z^3 = -M_z^4 \end{aligned} \tag{6.18}$$

The symmetrical properties of three components M_x, M_y and M_z in these four parts are summarized in Table 6.1.

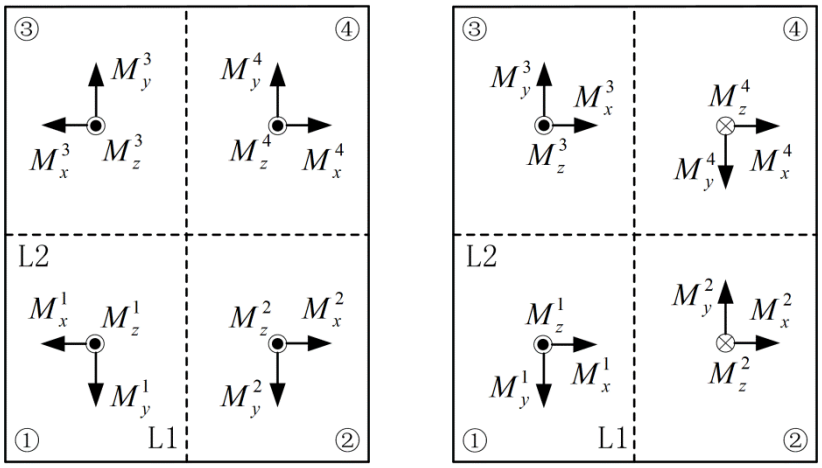

(a) Case A. (b) Case B.

Figure 6.8 Relationship of magnetization distributed on different parts.

After applying the same approach adopted for modeling the induced current, the constitutive equation at each node is modified by merging matrix entries for common M_x, M_y and M_z in four parts. Repeating the merging process for all nodes yields a further-reduced matrix equation, as follows:

$$\begin{bmatrix} \mathbf{L}_{\text{loop}}^{11} & \mathbf{Q}_{\text{loop}}^{11} \\ \mathbf{B}_{\text{loop}}^{11} & \mathbf{P}^{11} \end{bmatrix} \begin{bmatrix} \mathbf{I}_{\text{loop}}^{1} \\ \mathbf{M}^{1} \end{bmatrix} = \begin{bmatrix} \mathbf{U}_{\text{s,loop}}^{1} \\ \mathbf{B}_{\text{s}}^{1} \end{bmatrix} \tag{6.19}$$

Similarly, the number of each magnetization density component (M_x, M_y or M_z) is reduced to $N_x \bullet N_y / 4$, and the total number for three components of $\boldsymbol{M}$ is equal to $3N_x \bullet N_y / 4$. By using the techniques given in Section 6.1.2, and 6.2.1, the total number of unknowns in matrix (6.19) is equal to $N_x \bullet N_y$, compared with $6N_xN_y - N_x - N_y - 1$ in the original equation (6.1).

6.3. Numerical Test and Result Comparison

For validating the reliability and efficiency of the proposed modeling techniques, the wire-plate structures with magnetic material for both case A and

case B have been selected. First of all, shielding results are computed on the MATLAB codes developed using the proposed algorithm. The model of Eq. (6.1) is as set of original equations which takes the whole plate into consideration, and is named OM. The model in Eq. (6.19) is improved one using the proposed modeling techniques of loop analysis and symmetry, and is named PM. The simulation results are then compared with those obtained from the commercial software based on Finite Element Method (FEM).

The configuration for testing is as shown in Fig. 6.4. The plate is made from linear magnetic material with the conductivity of σ=6x10^6 S/m and the relative permeability of μ_r=170. It has the dimensions of 80x80x2 mm^3. The source of loop wire is 20 mm wide and 20 mm long, and carries a current of 1 A at 50 Hz. It is located in the center with a distance of 20 mm to the plate.

The information of the computer used for the simulation is given, as follows:

- CPU: Intel(R) Core i7-2600, 3.4GHz
- Memory: 16.00GB of RAM

A uniform mesh of 40 x 40 ($N_x = 40$, $N_y = 40$) is adopted in both case A and case B for OM and PM. Table 6.2 shows a summary of element number on the plate and computation time required. It is clearly that the number of total elements in FEM is much more than in both OM and PM, it is because all the regions including the free space in FEM need to be modeled and the discretization over the cross section of the plate. On the other hand, the number of unknowns of PM is reduced by 33% from OM when the loop technique is

applied, and is further reduced to just one sixth when the symmetrical modeling technique is implemented. As a result, PM reduces the computation time significantly (e.g., from 11 min. and 33 sec. to 1 min. and 16 sec. in Case A). Note that no particular optimization procedure was taken in the Matlab codes developed from the proposed method.

TABLE 6.2 Time and elements required by different methods.

Source	**Case A**			**Case B**		
Method	**PM**	**OM**	**FEM**	**PM**	**OM**	**FEM**
Total elements	3200	19038	2308235	3200	19038	2311046
Computing time	00:01:16	00:11:33	11:26:33	00:01:14	00:11:47	14:10:59

The computed resultant magnetic fields on line L are plotted in Fig. 6.9. As the same formulation is adopted, the same results can be obtained by both OM and the improved model (PM). And the results computed by the FEM and PM match well, with an average difference of 1.4% for two source orientations. In case A, the deviation between PM and FEM in most area is below 1%, the obvious deviation exists in the edge area and does not exceed 2%. In case B, the deviation is below 3% in most area. Due to the placement of source wire in case B, the fluctuations are relatively large in the central area. Both case A and case B validate that the proposed techniques are reliability and high efficiency.

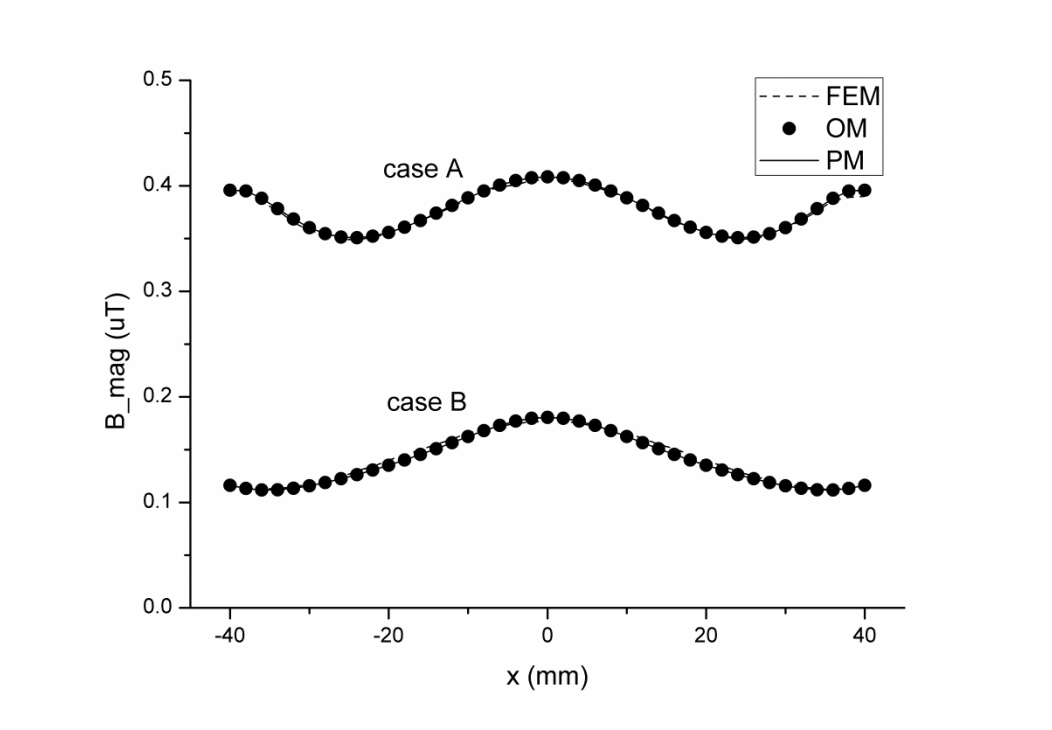

Figure 6.9 Magnetic fields on line L computed by the three methods.

6.4. Conclusion

This chapter presented the techniques for reduction of unknowns in PEEC model. The loop technique is given to combine the electric field integral equations set up for the branches along different orthogonal directions. The approach is presented for modeling symmetry and anti-symmetry properties of a wire-plate structure used in magnetic shielding applications. The PEEC model for such a structure was presented. The matrix equation obtained was reduced to one sixth approximately in size if these properties are fully taken into account. The proposed techniques have been tested numerically, and validated with the commercial EFM code. It found that shielding problems can be solved at the reduced cost without loss of accuracy. The proposed techniques are particularly useful in solving a large plate shielding problem with a high degree of symmetry

and/or anti-symmetry.

7. Application and Experimental Verification

To study protection concept and mitigate electromagnetic hazards effectively, it is proposed in this thesis to obtain an effective approach for evaluating low frequency magnetic fields in the presence of the large plate structures used in modern buildings. Different modeling methods based on PEEC method have been presented in former chapters.

In this chapter, for the application to large plate structures, a comparison of these modeling methods will be done. The suitable method with the optimization techniques will be applied to evaluate the magnetic shielding arose from the plate structures used in buildings. The experimental verification for the proposed procedure is implemented finally.

7.1. Discussion of Different PEEC Models

Different models based on the PEEC formulation have been proposed and discussed in above chapters. The advantages and disadvantages of these methods are also discussed. Any a method is based on an assumption of distribution of electromagnetic components and is suitable for special cases. Here, a simple plate is presented to investigate the computation abilities of these methods.

As shown in Fig. 7.1, the different meshing schemes for the presented modeling methods for a symmetrical plate are given. Just one fourth of the plate needs to be modeled. For M0, the plate needs to be discretized along all the directions (x, y, z) and a number of volume cells are formed. Due to the huge

number of unknowns, M0 is not capable for practical application. For M1, the meshing is done based on volume cells, and the unknowns are defined on the bottom and top surfaces (⑤ and ⑥) of the plate. All the electromagnetic components have the uniform grid. The refinement on the edge area is also done and the number of segmentation (*Nrx, Nry*) is included in *Nx* and *Ny*. The improved model is named as M1_R.

For M2, besides the volumes cells for current, the surface elements for magnetization on the outer of the plate (①, ③, ⑤ and ⑥) need to be added. Similarly, the refinement on the edge area is implemented and the model is named as M2_R.

For M3, meshing for the electromagnetic components which are in the plane of the plate is as same as in M1. But the segmentation on the edge area is also done, which is for *Mz* using the meshing scheme of M0, as seen the corner in Fig. 7.1.

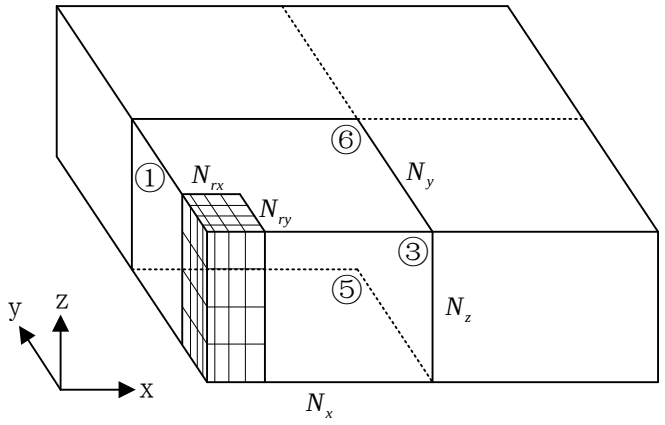

Figure 7.1 Meshing of different methods for a symmetrical plate.

A detail data sheet of the number of unknowns is given in Table 7.1 for comparison of different methods. It can be seen that the most complex data

constitution exists in M3, and the simplest one is in M1. It reflects the complexity of modeling. The number of unknowns in M3 is obviously more than in M1. When the plate is thin and *Nz* is small, the number of unknowns in M2 is less than in M1.

TABLE 7.1 Number of unknowns in different methods.

	I_{loop}	*Mx*	*My*	*Mz*	Total
M1_R	2*NxNy*	2*NxNy*	2*NxNy*	2*NxNy*	8*NxNy*
M2_R	2*NxNy*	2*NxNy*+ *NxNz*	2*NxNy*+ *NyNz*	*NxNz*+*NyNz*	6*NxNy*+ 2*Nz*(*Nx*+*Ny*)
M3	2*NxNy*	2*NxNy*	2*NxNy*	2(*Nx*-*Nrx*)(*Ny*-*Nry*)+ *Nz*(*NxNry*+*NrxNy*-*NrxNry*)	6*NxNy*+2(*Nx*-*Nrx*)(*Ny*-*Nry*)+ *Nz*(*NxNry*+*NrxNy*-*NrxNry*)

The configuration showed in Fig. 3.8 is employed for testing these different methods. The resultant magnetic field on a line in the space is calculated. The results from different methods are plotted in Fig. 7.2. It can be seen that the results are matched very well. Compared with the result from IES-FARADAY, the average errors are 0.8% in M1_R, 0.6% in M2_R and 1.1% in M3, respectively. All the results are at high accuracy and can be accepted. The factor for the application of these methods needs to be taken into account is the requirement for computation resource.

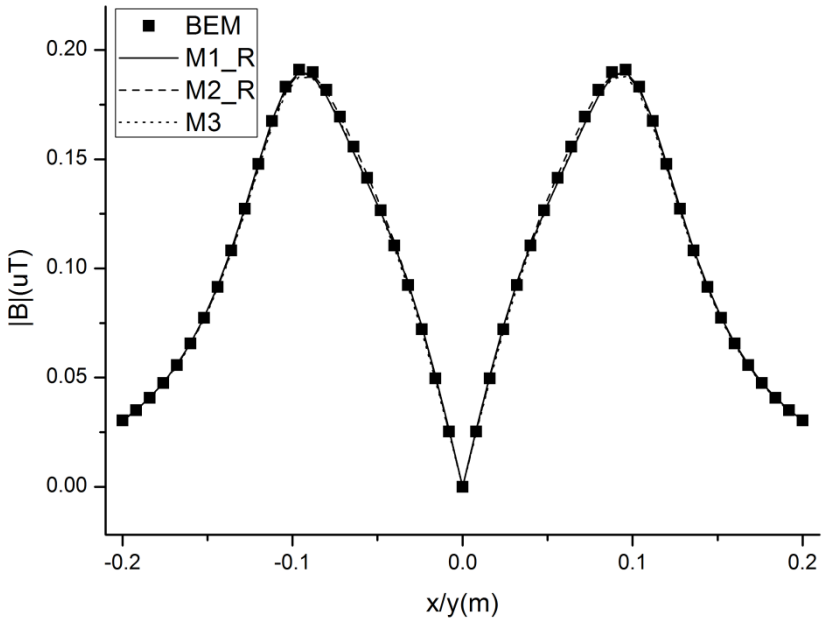

Figure 7.2 Resultant magnetic field from different numerical methods.

Considering the practical shielding structures are complex rather than the single simple plate, the method should be easy to model. M0 is not capable for practical application because of its huge number of unknowns after discretization. M2 needs to mesh on the surface of the object. When the geometry is complex and meshing is hardly to implement. As illustrated in Chapter 4, M3 can improve the accuracy of electromagnetic components distributed on the plate but a considerable effort is paid. The M1 method is convenient for modeling and easy to understand. The meshing scheme of this method is simple and uniform for all the electromagnetic components. It is suitable for practical engineering problems.

Therefore, this method is applied to model the practical shielding structures which involve the metal plates. To solve the problem efficiently use the

proposed methods, the techniques for reduction the number of unknowns, such as loop method and the symmetrical modeling technique have been proposed. The non-uniform meshing has also been applied.

7.2. Application

7.2.1. Application for Plates

The 3D simulation package based on the proposed method (PM) is developed, which runs on the platform of MATLAB. It is applied for a shielding structure involved a large magnetic plate. The result is compared with the commercial software based on Finite Element Method (FEM).

Due to the FEM requires that all regions including the free space be modeled, a large number of grid will be produced after discretization. Especially when the model is three-dimensional, the massive grid will lead the computer cannot afford. A relatively large size structure is beyond the capability of 3D module of FEM. Therefore, the structures with different sizes will employ different modules in FEM. The small size case can be simulated with 3D models, and the large size case need be modeled with the 2D model in FEM. Here, a small size structure, which is within the computation capacity of the 3D module of FEM, will be calculated for reference.

The large structure under investigation is as seen in Fig. 3.8. Considering the geometrical features of the structure, the plate has a long length and finite width. The concerned domain is the plane which involves the cross section of the plate. And it is perpendicular to the direction of length. Thus, the geometry can be

simplified as a two-dimensional model. The 2D module of FEM is available for validation.

The simple wire-plate structures shown in Fig.3.8 will be computed. The plate is made from linear magnetic materials with the conductivity of $\sigma = 6 \times 10^6 S/m$ and the relative permeability of $\mu_r = 170$. The external source is a filamentary conductive wire loop frame with the length l and width w running in parallel with the plate. It is located in the center with the separation distance of h from the plate. The source loop carries an a.c. current of $I = 1A$ at the frequency of $f = 50Hz$. The sizes of the structures are listed in Table 7.2.

TABLE 7.2 The sizes of the two testing structures. (M)

	w	**l**	**d**	**w_s**	**l_s**	**h**
small	0.08	0.08	0.002	0.02	0.02	0.02
large	1	4	0.002	0.2	4	0.1

The information of the computer used for the simulation is given, as follows:

- CPU: Intel(R) Core i7-2600, 3.4GHz
- Memory: 16.00GB of RAM

The computation information is given in Table 7.3. It is clearly that the computation time for the proposed method is much less than the software. For FEM 3D module, a minimum of grid is adopted to ensure a reasonable result and it does not run out of memory on this computer.

TABLE 7.3 Compare of computation information.

	small		**large**	
	FEM 3D	**PM 3D**	**FEM 2D**	**PM 3D**
Total elements	2308235	3200	61529	12800
Compute time	11:26:33	00:01:16	00:02:06	00:20:31

The resultant magnetic field was calculated by both methods on a line above the plate. It runs in parallel with the x axis above the plate at the height of p.

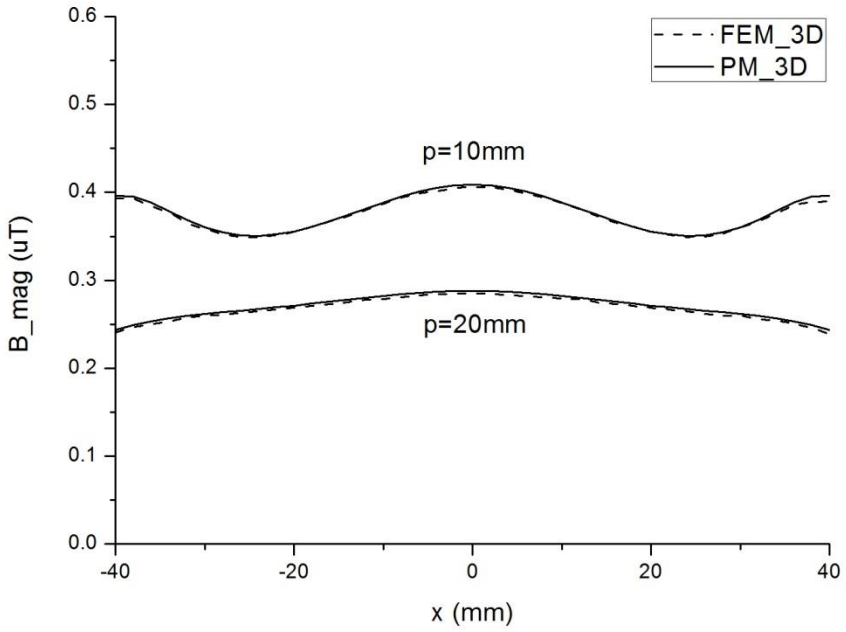

(a) Both 3D models in FEM and PM.

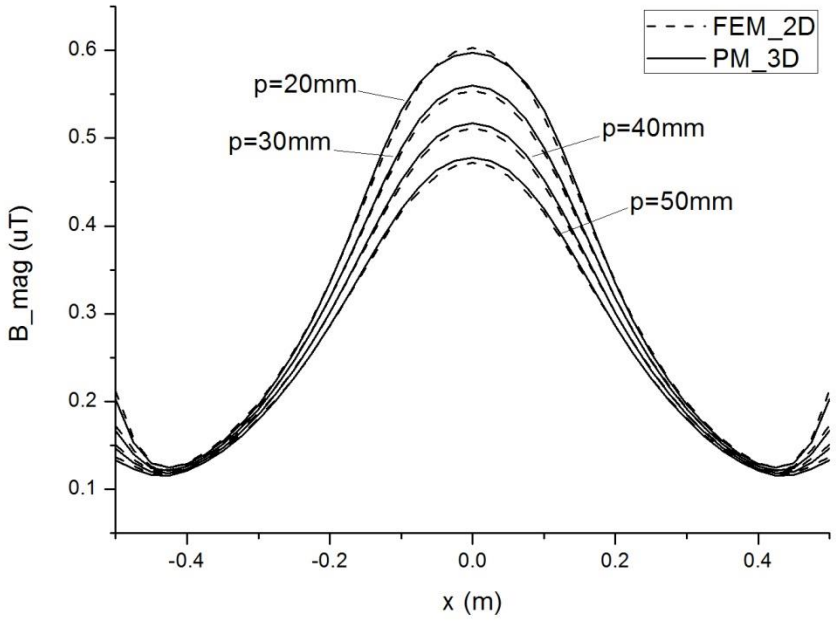

(b) 2D model in FEM and 3D model in PM.

Figure 7.3 Compare the resultant magnetic field from FEM and PM.

Fig. 7.3 shows the resultant magnetic fields calculated by FEM and the proposed method (PM). For case 1, the smaller structure can be calculated with 3D models in both methods. The results compared in Fig. 7.3(a), the relative errors at different positions are well-distributed. The farther away from the plate, the greater the error, the relative error is below 0.5% at $p = 10mm$ and is around 2% at the space ($p = 30mm$). The number of elements of the plate and the computation time of FEM are far more than the PM.

For the larger plate in case 2, it is beyond the capability of FEM 3D module, and an approximate 2D model is calculated to compare with the 3D model in PM. The resultant magnetic fields in different positions match very well. During the most area, the relative error is below 1%. Even at the very narrow edge area

where the distribution closed to singular, the relative error is below 3%. At the nearest position ($p = 20mm$), the relative error has obvious fluctuations, the largest error is 1.73% which is on the position of wires. At the other observation positions ($p = 30, 40, 50mm$), the relative errors are smooth, they are all located at the center point where the magnetic field is the strongest, and the largest error is 1.4% ($p = 50mm$).

7.2.2. Application for U-shape Shielding Structure

As an exploration of application for complex large shielding structures by using the proposed PEEC modeling method, a U-shape metal structure is employed for investigated. The U-shape structure is commonly used as a semi-enclosure metallic trunking to isolate the wires from the outside world.

Fig. 7.4 shows the configuration of the U-shape shielding structure with the power lines. The power lines are surrounded by the U-shape structure. The power lines is considered as the long straight wires, thus, the U-shape shield has a long length l.

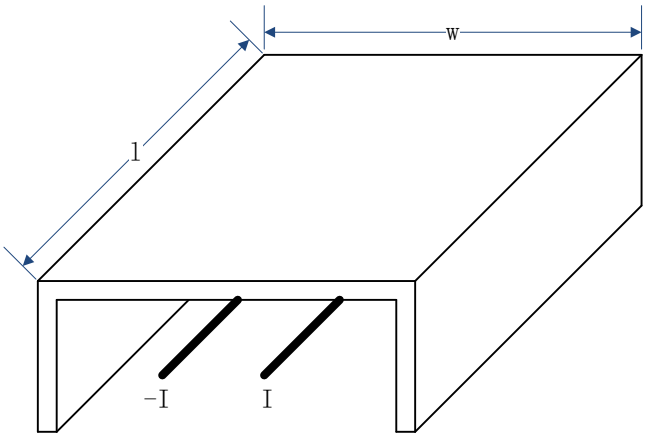

Figure 7.4 The configuration of a U-shape shielding structure for power lines.

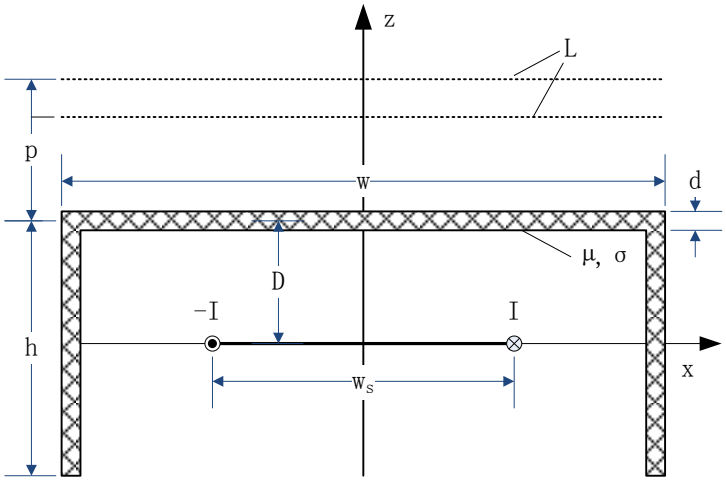

Figure 7.5 The section of the configuration of a U-shape shielding system.

The section view of the shielding structure is as shown in Fig. 7.5. The U-shape shield is made from linear magnetic materials with the conductivity of $\sigma = 7.5\times10^{6} S/m$ and the relative permeability of $\mu_r = 200$. The external source is a pair of power lines which carry the a.c. current of $I = 100A$ at the frequency of $f = 50Hz$. It is located in the center with the separation distance of D from the plate. The sizes of the structures are listed in Table 7.4.

TABLE 7.4 The sizes of the U-shape shielding structures. (M)

	w	**l**	**h**	**d**	**w_s**	**D**	**p**	
size	0.4	1.6	0.2	0.002	0.2	0.1	0.15	0.2

The computation resource is as same as in section 7.2.1. The resultant magnetic fields on the lines above the plate are calculated by the proposed PEEC procedure M1_R which is a 3D solver. The lines run in parallel with the x axis above the plate at the height of p. The geometry is simplified as a two-dimensional model in the 2D module of FEM for validation. And the magnetic fields arose from the power lines without shields are calculated for

evaluating the shielding effectiveness by the U-shape structure.

Fig. 7.6 shows the resultant magnetic fields calculated by FEM and the proposed method (M1_R). In the center area, the shielding effectiveness at the two positions are around 35% ($p = 0.15m$) and 38% ($p = 0.2m$), respectively. In the other area, the shielding effectiveness reduces slowly up to 50%.

At both the two observation positions, the results from M1_R and FEM are matched well. At $p = 0.15m$, the average deviation between FEM and M1_R is 1.2% and the largest value is 1.8%. At $p = 0.2m$, the average deviation is just 0.9% and the largest value is 1.5%. The comparison proves that the proposed PEEC modeling method is effective and efficient.

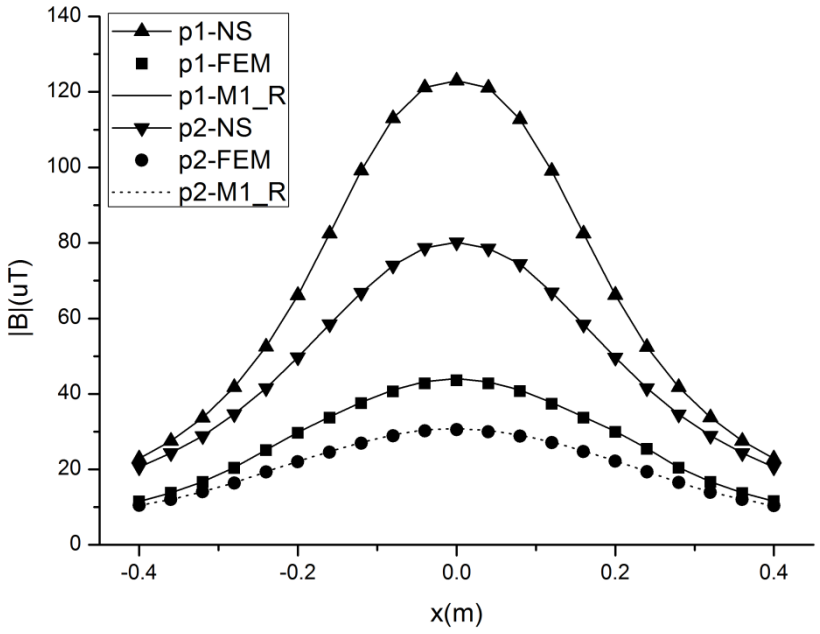

Figure 7.6 Evaluating the shielding effective of U-shape structure.

There are several new modeling techniques have been developed for U-shape structure, such as the meshing technique for the corner, the symmetrical

modeling technique for non-plane geometry. These methods and techniques are capable to be employed widely. The implementation on U-shape shielding structure in this section is a start of the application for complex large shielding structures.

7.3. Experimental Verification

As mentioned in Chapter 4 that it is difficult to solve a large-plate shielding problem using the existing commercial packages if the computing resource is limited. Therefore, for validating the application of the proposed PEEC method on the larger structures, the experimental verification is useful.

For the experiments, many factors may lead the measurement errors: 1) size error and deformation of the structures; 2) the deviation of measurement positions; 3) the error of parameters of the material; 4) current fluctuations; 5) the error of the measuring instrument; 6) a “clear” electromagnetic environment is very hard to be framed. In order to reduce the measurement error as much as possible, according to the directions of polarization of the magnetic field, only the effective components of magnetic field have been considered and measured separately.

A laboratory experiment was planned for validating the proposed method with a large plate structure. The wire-plate structure was selected for validating the proposed method, as illustrated in Fig. 3.8. The validation was made by comparing the magnetic fields computed from the proposed method and the results from the experiments. The magnetic fields around the shield plates which

blocking or covering the power cables will be measured. The magnetic source investigated here is the stationary current at power frequency.

The magnetic plate under test was 1.22m wide and 2.44m long. Its conductivity is about $\sigma = 6 \times 10^6 S/m$, and the relative permeability is about $\mu_r = 170$. A source loop as shown in Fig. 7.4 is placed under the plate. There are three different configurations: (a) horizontally-arranged loop, (b) vertically-arranged loop, and (c) L-shape loop. The detailed dimensions of both the plate and source loop are given in Table 7.4.

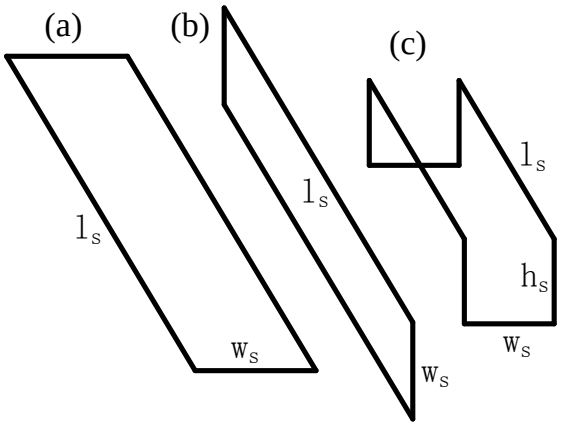

Figure 7.7 Source wire configurations for testing.

TABLE 7.4 The Sizes of The Three Testing Structures. (m)

	w	**l**	**d**	**w_s**	**l_s**	**h_s**	**h**	**p**
Case a	1.22	2.44	0.002	0.1	2.2	-	0.136	0.147
Case b				0.1	2.2	-	0.086	0.147
Case c				0.1	1	0.5	0.136	0.147

The magnetic field meter used here to record the magnetic field components is ‘Field Star 1000’, which is a three-axis field meter is convenient to use for obtaining the resultant value of a magnetic field.

In the experiment the loop was connected to a current injection source, which

provides a constant current of $I = 100A$ at the frequency of $f = 50Hz$. Magnetic field density along line *L*, which is the middle line along x axis above the plate, was measured for comparison, as plotted in Fig. 3.8(a). According to the layout of the wire frames, the effective components of magnetic field on the line *L* are $\boldsymbol{B}_x$ and $\boldsymbol{B}_z$, and they have been calculated and measured.

The resultant magnetic field at selected points is presented in Fig. 7.5. The matlab code developed for the proposed method was employed to compute the magnetic field on the same measurement line as well. In the computation the plate was divided into 40x80 potential cells.

Fig. 7.5 shows the comparison of the resultant magnetic fields obtained from both the proposed computation method (PM) and the laboratory experiment for the three different source configurations. It is found that both measured and calculated magnetic fields match well under these source configurations. Get rid of the tiny values which will lead abnormal relative errors. In case a, for both $\boldsymbol{B}_x$ and $\boldsymbol{B}_z$, the relative errors are relatively small. The average error of $\boldsymbol{B}_x$ is 4.9% and the maximum is below 10%, the average error of $\boldsymbol{B}_z$ is 2.9%. The deviation in case b is larger than in case a, there are two reasons: 1) the deformation of the wire frame is more significant than in cases 1 due to it is laid vertically; 2) it is closer to the plate. Even so, the error of $\boldsymbol{B}_x$ and $\boldsymbol{B}_z$ at most area are below 10% and the average value is 4.9%. In case c, the law of error is similar to that in case a, but there is an obvious larger deviation at the two sides, it is caused by the more complexity of the wire frame. The average error of $\boldsymbol{B}_x$

is 5%, and for $\boldsymbol{B}_z$ is 6.5%. The diffidence of the measured and calculated magnetic field is considered reasonable for the purpose of experiment validation.

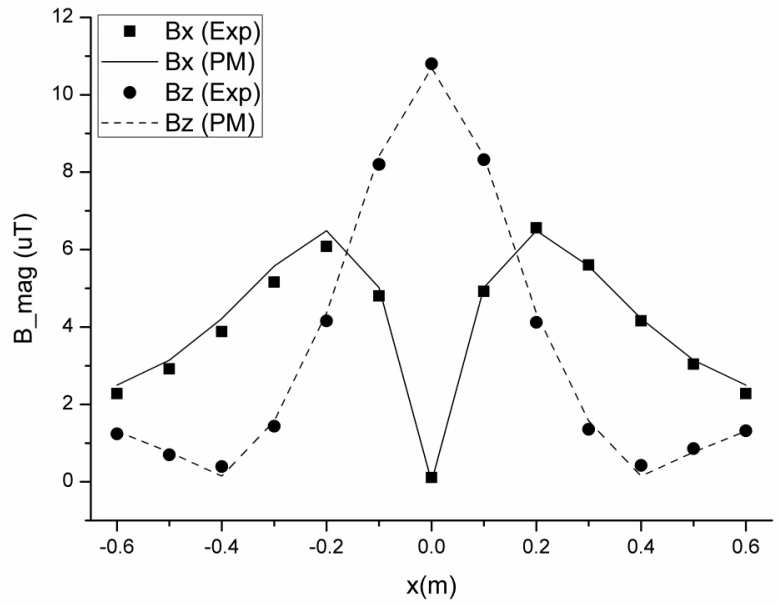

(a) Case a

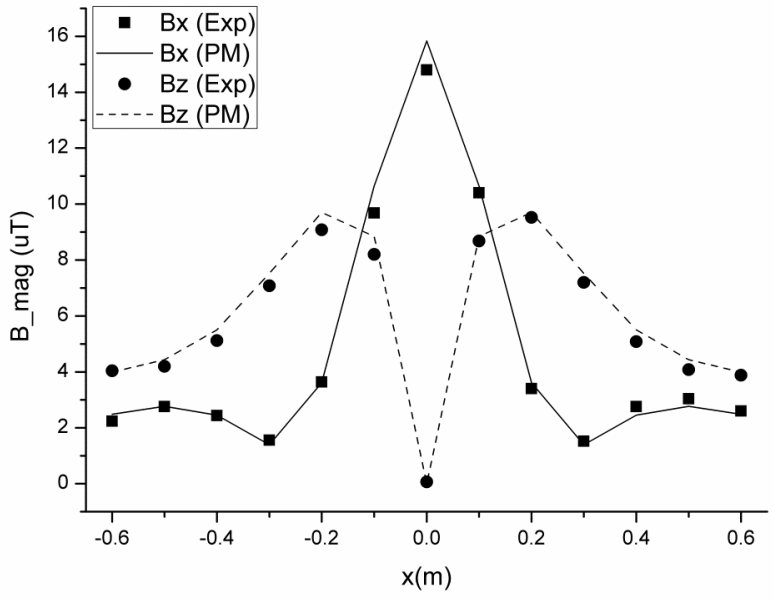

(b) Case b

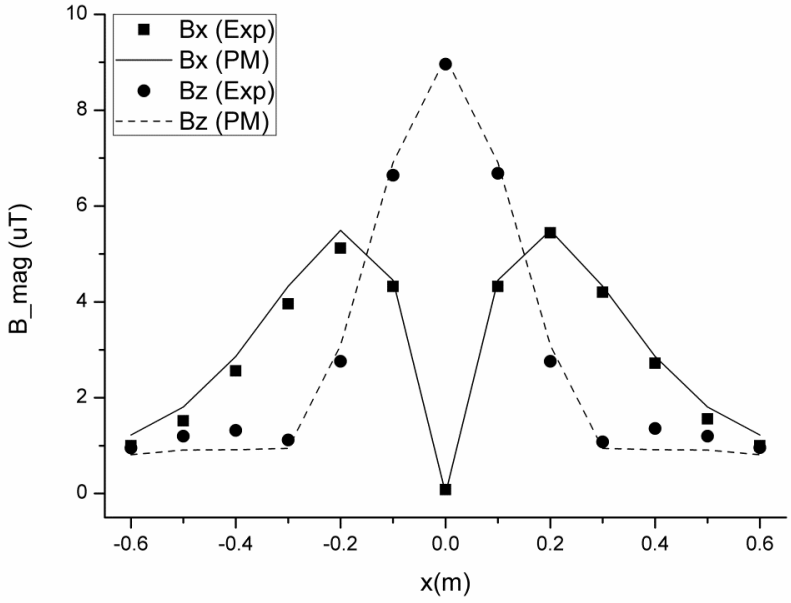

(c) Case c

Figure 7.8 Comparison of PM and experimental results for a large plate.

7.4. Conclusion

The proposed 3D electromagnetic modeling method and techniques have been applied for a large ferromagnetic plate and U-shape structure used for magnetic shielding. The solutions are validated by numerical method and experiment. The result demonstrates that it is reliable and efficient. This proposed method reduces the number of unknowns significantly. The total procedure cut down the requirement of computation resources greatly and the results prove that the accuracy is retained. The evaluation for power frequency magnetic field shielded by larger and complex geometry plates becomes possible.

8. Conclusions and Future Work

In this thesis, different modeling methods (M0, M1, M2 and M3) based on PEEC method have been presented and discussed. The corresponding solution packages have been developed. Due to the different assumptions, they have different advantages and disadvantages and are applicable for corresponding cases. Every solver based on the method (M0, M1, M2 and M3) includes 2D and 3D modules.

For the methods M0, M1, M3, the geometry is discretized into volume cells. In M0, EM components in each cell are constant. The meshing scheme is simple and easy to implement. When the distribution of EM components on the plate fluctuates greatly, a high density grid is needed. This limits the application of M0. M0 is capable to simulate small shielding structures and validate other numerical models.

The analytical expression of double exponential function is applied to the PEEC model in M1. Both induced current and magnetization densities in the plates are approximated by this analytical function across plate thickness. The proposed method eliminates the need of plate meshing along its thickness, and reduces the number of unknowns significantly in 3D shielding problems. M1 is easy to implement and understand. This procedure is suitable for practical engineering problems with complex structures.

When the plate is made of magnetic material, the EM components distributed on the plate vary greatly in some special areas which are related to the location of

external source. In order to simulate this variation, the non-uniform meshing technique is proposed. For the edge region and the region where is closer to the external source, the mesh refinement is carried out. And for most area where the EM components vary smoothly, the coarse uniform mesh is assigned. This non-uniform mesh scheme significantly improves the accuracy of results and maintains a limited number of unknowns.

Both in M0 and M1, the sets of grid for different EM components (current density and/or magnetization) are consistent. Thus, M0 and M1 can be used to model both non-magnetic and magnetic structures, and the discretization is easy to operate.

Due to different EM components have different variations on the plate, when there is a considerable difference between these variations, different sets of grid may be needed to be considered. In view of the component which is perpendicular to the plate (for example $\boldsymbol{Mz}$ in this thesis), a special mesh refinement is implemented in the edge region for it and unlike other sets of grid for other EM components. This is the modeling method M3.

To specifically address the magnetization, the new modeling method M2 is presented. The volume current and surface current of magnetic polarization are separated, and the former item is combined with the induced current. Then, the unknowns are composed of the induced current density defined on the volume cells and the magnetization defined on the surface cells.

M2 and M3 are particular for magnetic material. M2 deals with the magnetization on the outer surface and is meaningful when the thickness is comparable to the other characteristic dimensions of the plate. M3 is a hybrid method and has more accuracy compared to other methods although there is a considerable amount of unknowns. It is suitable for investigation the characteristics of distribution of induced current and magnetization on the plate.

For reducing the number of unknowns in PEEC model, the techniques, such as loop method and the symmetrical modeling technique have been proposed as well.

For solving the practical problems in shielding system, the modeling method M1 is selected. By integrating M1 with the non-uniform meshing technique and reduction technique, a numerical solver has been developed. It has a powerful computing capability, and the reasonable results can be obtained.

There are some meaningful works can be further performed:

1. The proper analytical function needs to be found to express the distributions of electromagnetic components located in the edge area of the magnetic plate. This can correct the deviation of double exponential expression.

   In fact, for a point r inside the plate, a relationship function can be constructed naturally as:

$$H(r) = \sum_{i=1}^{6} f_i(r - r_i') \bullet H_i(r') \tag{8.1}$$

   Where $H(r)$ is the electromagnetic field value at r, $H_i(r')$ is the

value located on the surface i of the plate, and f is the functional relationship between $H(r)$ and $H(r')$. When $H(r)$ is located in the inner plate, due to the skin effect, i.e. $r - r_i' \gg \delta$, δ is the skin depth. The weight of f_i is wake and the effect arose from $H_i(r')$ can be neglected. For $H(r)$ in the center area of the plate, the effective weight functions are just came from the bottom and top surface. That is why the distribution in center area can be defined by the values on both the bottom and top surface according to the double exponential function but it is not accurate on the edge area.

2. Sparse inductance matrix for the PEEC models. There are two steps:

   Firstly, sparsity of the inductance matrix will be done. Using the locality of the inverse matrix of inductance matrix, to sparsify the inverse matrix and then invert it to return to inductance matrix. This can sparsify the dense matrix formed by extracted partial element and mitigate the effort of computation.

   Secondly, considering the mutual coupling between two cells which are with a quite distance is very small, the equivalent mutual inductance can be neglected. A radius r_0 will be defined to form an enclosure, the mutual inductance between the center point and the cells inside the enclosure will be considered, and the effect from the cells outside the enclosure will be omitted.

3. Sparsity of other coefficient matrixes.

As similar as the inductance matrix, other coefficient matrixes are also full denseness matrixes and need to be optimized. Maybe the characteristics of these matrixes are different from inductance matrix and different to each other, they need to be considered separately.

4. Optimization steps for solving the matrix equations.

   Due to the metal plate employed for investigated in this thesis is very thin, the extraction of partial elements on the bottom and the top surfaces are very closer. This causes the condition number of the matrix is very large. The condition number of a matrix measures the sensitivity of the solution of a system of linear equations to errors in the data. It gives an indication of the accuracy of the results from matrix inversion and the linear equation solution. As a result, the matrix is with low stability and susceptible to disturbance.

   The general iterative solution steps are hardly to handle the full dense matrixes in this thesis. It is significant to catch a proper solution steps for the matrixes.

5. Application of the PEEC models and the optimization techniques for reduction and speeding to the large complex shielding structures in buildings.

   In view of the above techniques, the PEEC models can be applied to some degree of size of large geometry. For the shielding structures applied in buildings, due to the large size of them, they are hardly to be solved in a

closed space with a boundary. The open boundary field solution is an available approach.

The proposed method has been applied and implementing for some complex structures, such as the shields for transformer.

Reference

[1] (2000). ANSI/AAMI PC69. American active implantable medical devices – Electromagnetic compatibility – EMC test protocols for implantable cardiac pacemaker and implantable cardioverter defibrillators. Washington, DC: National Standard Institute / Association for the Advancement of Medical Instrumentation; 2000.

[2] (1997). CEN/CLC/JWG AIMD EN 45502-1. Active implantable medical devices. Part 1: General requirements for safety, marking and information to be provided by the manufacturer. Bruxelles: Comité Européen de Normalisation Electrotechnique; 1997.

[3] (2003). CEN/CLC/JWG AIMD EN 45502-2-1. Active implantable medical devices. Part 2-1: Particular requirements for active implantable medical devices intended to treat bradyarrhythmia (cardiac pacemakers). Bruxelles: Comité Européen de Normalisation Electrotechnique; 2003.

[4] (2006). CEN/CLC/JWG AIMD prEN 45502-2-2. Active implantable medical devices. Part 2-2: Particular requirements for active implantable medical devices intended to treat tachyarrhythmia (includes implantable defibrillators). Bruxelles: Comité Européen de Normalisation Electrotechnique; 2006.

[5] (2006). CEN/CLC/JWG AIMD prEN 45502-2-3. Active implantable medical devices. Part 2-3: Particular requirements for cochlear implant systems. Bruxelles: Comité Européen de Normalisation Electrotechnique; 2006.

[6] (2006). International Electrotechnical Commission. IEC EN 60601-1. Medical electrical equipment. Part 1: General requirements for basic safety and essential performance. Geneva: IEC; 2006.

[7] (2003). International Electrotechnical Commission. IEC EN 60601-1-2. Medical electrical equipment. Part 1: General requirements for safety. 2. Collateral standard: electromagnetic compatibility. Requirements and tests. Geneva: IEC; 2003.

[8] (1999). Standard C63.18. Recommended practice for an on-site, ad hoc test method for

estimating radiated electromagnetic immunity of medical devices to specific radiofrequency transmitters. Washington, DC: American National Standard Institute; 1999.

[9] (2001). The International Agency for Research on Cancer (IARC), 'Evaluation of carcinogenic risks to humans: static and extremely low frequency electric and magnetic fields', IARC Monographs, June 2001, 80, pp. 1–429

[10] (2011). "IARC classifies radiofrequency electromagnetic fields as possibly carcinogenic to humans" (Press release). 2011-05-31.

[11] A. Abakar et al., "3D modeling of thin wire and thin plate using finite element method and electrical circuit equation," IEEE Trans. on Magnetics, Vol. 37, Issue 5, Part 1, Sept. 2001 , pp. 3238-3241.

[12] A. Canova, A. Manzin, and M. Tartaglia, "Evaluation of different analytical and semi-analytical methods for the design of ELF magnetic field shields," *IEEE Trans. Ind. Appl.*, vol. 38, no. 3, pp. 788–796, May/Jun. 2002.

[13] A. Canova, G. Gruosso, and M. Repetto, "Integral methods for analysis and design of low-frequency conductive shields," *IEEE Trans. Magn.*, vol. 39, no. 4, pp. 2009–2017, Jul. 2003.

[14] Antonini, G., "SPICE equivalent circuits of frequency-domain responses," *Electromagnetic Compatibility, IEEE Transactions on*, vol.45, no.3, pp.502,512, Aug. 2003.

[15] Antonini, G., M. Sabatinni and G. Miscione, "PEEC modeling of linear magnetic materials," Proc. of IEEE 2006 International Symposium on EMC, Aug. 2006, Vol. 1, pp. 93-98.

[16] Antonini, G., J. Delsing, J. Ekman, A. Orlandi, A. Ruehli, "PEEC development road map 2007".

[17] A. Kost and H. Igarashi, "Different numerical methods for electromagnetic field computation with thin shielding sheets," in *Proc. IEEE Int. Symp. Electromagnetic*

Compatibility, Austin, TX, 1997, pp. 248–253.

[18] A. Muhlbauer, et al., “The calculation of 3D high-frequency electromagnetic fields during induction heating using the BEM ,” IEEE Trans. on Magnetics, Vol. 29, Issue 2, Mar. 1993, pp. 1566-1569.

[19] Baan R, Grosse Y, Lauby-Secretan B, El Ghissassi F, Bouvard V, Benbrahim-Tallaa L, Guha N, Islami F, Galichet L, Straif K, on behalf of the WHO International Agency for Research on Cancer Monograph Working Group (1 July 2011). "Carcinogenicity of radiofrequency electromagnetic fields". *The Lancet Oncology* **12** (7): 624–6.

[20] B. Archambeault, O. M. Ramahi, and C. Brench, *EMI, EMC Computational Modeling Handbook*. Norwell, MA: Kluwer, 1998.

[21] B. Krauter and L. T. Pileggi, “Generating sparse partial inductance matrices with guaranteed stability,” Proc. of IEEE/ACM Int. conf. comput. –aided design, Nov. 1995, pp. 45-52.

[22] C. A. Balanis. *Advanced Engineering Electromagnetics*. Wiley. 1989.

[23] Cardelli, E.; Faba, A.; Pirani, A., "Nonferromagnetic Open Shields at Industrial Frequency Rate," *Magnetics, IEEE Transactions on* , vol.46, no.3, pp.889,898, March 2010

[24] Chung-Wen Ho; Ruehli, Albert E.; Brennan, Pierce A., "The modified nodal approach to network analysis," *Circuits and Systems, IEEE Transactions on* , vol.22, no.6, pp.504,509, Jun 1975.

[25] Coperich, K. M., Ruehli, A. E. and Cangellaris, A. ‘Enhanced skin effect for partial element equivalent circuit (PEEC) models’. *IEEE Trans. Microwave Theory and Technique*, **48**, 2000, 1435–1442.

[26] Cristopoulos, C. The Transmission-Line Modeling Method TLM, IEEE Press, New York, USA, 1995.

[27] C.V. Dodd and W.E. Deeds, “Analytical solutions to eddy current probe-coil problems,”

J. Appl. Phys. 1968, 39, (3), pp 2829-2838.

[28] E. Chiprout, M. Nakhla. .*Asymptotic Waveform Evaluation and Moment* Matching *for Interconnect Analysis.* Boston: Kluwer Academic Publishers. 1993.

[29] Focke F, Schuermann D, Kuster N, Schär P (November 2009). "DNA fragmentation in human fibroblasts under extremely low frequency electromagnetic field exposure". *Mutation Research* **683** (1–2): 74–83.

[30] F. H. Branin. A unifying approach to the classical methods of formulating network equations. In *Proc. of the IEEE Int. Symp. on Circuits* and *Systems,* pages 750-754. San Francisco, CA, April 1974.

[31] G. Coen. D. De Zutter. Reduction of circuit complexity using tensor analysis of networks. In *Proc. of the IEEE Int. Symp. on Electromagnetic Compatibility.* volume 11. Zurich, Switzerland, February 1997.

[32] Garrett, J. E.; Ruehli, A. E. "PEEC-EFIE for Modeling 3D Geometries with Lossy Inhomogeneous Dielectrics and Incident Fields", *IBM Research Report RC 19245,* IBM T. J. Watson Research Center, Yorktown Heights, October 1993.

[33] Garrett, J. E., Ruehli, A. E. and Paul, C. 'Efficient frequency domain solutions for sPEEC EFIE for modeling 3D geometries'. Proceedings of the International Symposium on EMC, Zurich, Switzerland, March 1995, pp. 179–184.

[34] Garrett, J., Ruehli, A. E. and Paul, C. 'Accuracy and Stability Advancements of the Partial Element Equivalent Circuit Model', Proceedings of the International Symposium on EMC, Zurich, Switzerland, March 1997, 529–534.

[35] Garrett, J., Ruehli, A. E. and Paul, C. 'Stability Improvements of Integral Equation Models'. *IBM Research Report RC 20701,* IBM T. J. Watson Research Division, January 1997.

[36] Giwoo Jeung; Chang-Seob Yang; Hyun-Ju Chung; Se-Hee Lee; Kim, Dong-Hun, "Magnetic Dipole Modeling Combined With Material Sensitivity Analysis for Solving an Inverse Problem of Thin Ferromagnetic Sheet," *Magnetics, IEEE Transactions on ,*

vol.45, no.10, pp.4169,4172, Oct. 2009

[37] Goerisch, A. ‘Netzwerkorientierte Modellierung und Simulation elektrischer Verbindungsstrukturen mit der Methode der partiellen Elemente’. Otto-von-Guericke-Universit ̈at Magdeburg, Germany, Dissertation, May 2002.

[38] Guarnieri, M.; Moro, F.; Turri, R., "An integral method for extremely low frequency magnetic shielding," *Magnetics, IEEE Transactions on* , vol.41, no.5, pp.1376,1379, May 2005

[39] Harrington, R.F. Field Computation by Moment Method, IEEE Press, New York, USA, 1993.

[40] Heeb, H.; Ruehli, A., "Approximate time-domain models of three-dimensional interconnects," *Computer Design: VLSI in Computers and Processors, 1990. ICCD '90. Proceedings, 1990 IEEE International Conference on* , vol., no., pp.201,205, 17-19 Sep 1990.

[41] H. Hu and S. Sapatnekar, “Eficient inductance extraction using circuit-aware techniques,” IEEE Trans on VLSI Systems, Vol. 10(6), Dec. 2002 , pp. 746-760.

[42] H. R. Heeb. EMI simulation using retarded partial element equivalent circuits and asymptotic waveform evaluation. In *Proc. of the IEEE Int. Symp. on Electromagnetic Compatibility*, volume 10, pages 191-195, Zurich, Switzerland, March 1995.

[43] H. T. Yu, S. L. Ho, M. Q. Hu, H. C. Wong, “Edge-based FEM-BEM for wide-band electromagnetic computation,” IEEE Trans. on Magnetics, Vol. 42, Issue 4, April. 2006, pp. 771-774.

[44] Hoer, C. and Love, C. ‘Exact Inductance Equations for Rectangular Conductors with Applications to More Complicated Geometries’. J. Res. Natl. Bur. Stand., **69C**, 1965, 127–137.

[45] HUGO, Human Model dataset 3.0, Computer Simulation Technology, Germany 2003.

[46] J. Ekman et al., “The Impact of Partial Element Accuracy on PEEC Model Stability”,

IEEE Transactions on Electromagnetic Compatibility, vol. 48, no. 1, pp.19-32, Feb., 2006.

[47] J. Garrett, A. E. Ruehli, and C. R. Paul, “Accuracy and Stability Improvements of Integral Equation Models using the partial element equivalent circuit PEEC approach”, IEEE Trans. on Antennas and Propagation, 46(12):1824-1831, Dec. 1998.

[48] J. Jin, The Finite Element Method in Electromagnetics. John Wiley & Sons, New York, USA, 1993.

[49] J. P. Berenger, “A perfectly matched layer for the absorption of electromagnetic waves,” J. Comput. Phys., vol. 114, no. 2, pp. 185–200, Oct. 1994.

[50] K. J. Binns and P. J. Lawrenson, Analysis and computation of electric and magnetic field problems, Pergamon Press Ltd, New York, 1977.

[51] K. L. Kaiser, Electromagnetic Compatibility Handbook, CRC Press, New York, 2005.

[52] Kamon, M.; Tsuk, M.J.; White, J., "FastHenry: A Multipole-Accelerated 3-D Inductance Extraction Program," *Design Automation, 1993. 30th Conference on* , vol., no., pp.678,683, 14-18 June 1993.

[53] Kamon, M., Marques, L., Silveira, L. M. and White, J. ‘Generating Reduced Order Models via PEEC for Capturing Skin and Proximity Effects’. Proceedings of the Electrical Performance of Electronic Packaging Conference, West Point, NY, USA October 1998, pp. 259–262.

[54] Koroglu, S.; Umurkan, N.; Kilic, O., "Experimental performance investigation of double-layer shields at power frequency magnetic shielding," *Power Quality and Supply Reliability Conference, 2008. PQ 2008* , vol., no., pp.207,210, 27-29 Aug. 2008

[55] Kost, A. Numerische Methoden in der Berechnung elektromagnetischer Felder, Springer Verlag, Berlin–Heidelberg, Germany, 1994.

[56] K. S. Yee, “Numerical solution of initial boundary value problems involving Maxwell’s equations in isotropic media,” *IEEE Trans. Antennas Propag.*, vol. AP-14, no. 5, pp.

302–307, May 1966.

[57] Losito, O.; Dimiccoli, V.; Barletta, D., "Low frequency shielding improvement by multilayer design," *EMC Europe 2011 York* , vol., no., pp.640,643, 26-30 Sept. 2011

[58] L. Sandrolini, A. Massarini, U. Reggiani, “Transform method for calculating low-frequency shielding effectiveness of planar linear multilayered shields,” IEEE Trans on EMC, Vol. 36, No. 6, Nov. 2000 , pp. 3910-3919.

[59] M. Istenic, R. G. Olsen, “A simple hybrid method for ELF shielding by imperfect finite planar shields,” IEEE Trans on EMC, Vol. 46, No. 2, May. 2004 , pp. 199-207.

[60] M. N. O. Sadiku, “A simple introduction to finite element analysis of electromagnetic problems,” *IEEE Trans. Educ.*, vol. 32, no. 2, pp. 85–93, May 1989.

[61] Miller, E.K., Medgyesi-Mitschang, L.N. and Newman, E.H. Computational Electromagnetics, IEEE Press, New York, USA, 1992.

[62] Milsom, R.F.; Scott, K.J.; Clark, G.; Mcentegart, J. C.; Ahmed, S.; Soper, F. N., "FACET - A CAE System for RF Analogue Simulation Including Layout," *Design Automation, 1989. 26th Conference on* , vol., no., pp.622,625, 25-29 June 1989.

[63] Mittra, R. Numerical and Asymptotic Techniques in Electromagnetics, Springer Verlag, Germany, 1975.

[64] Mittra, R. (ed.) Computer Techniques for Electromagnetics, Springer Verlag, Germany, 1987.

[65] Mohammed, O. A.; Uler, F. G, “3D finite element grid generation in electromagnetics,” Proc. of IEEE Southeastcon, Vol. 2,1-4, April 1990 pp. 684-688.

[66] M. Trlep, A. Hamler, M. Jesenik, B. Stumberger, “The FEM-BEM analysis of complex grounding systems,” IEEE Trans. on Magnetics, Vol. 39, Issue 3, May. 2003, pp. 1155-1158.

[67] Nagel, L. W. 'SPICE: a computer program to simulate semiconductor circuits', *Electr. Research Lab. Report ERL M520*, University of California, Berkeley, USA, March 1975.

[68] N. Ida, Numerical modeling for electromagnetic non-destructive evaluation, Chapman & Hall, New York, 1995

[69] Nitsch J, Gronwald F, Wollenberg G (2009) Radiating nonuniform transmission-line systems and the partial element equivalent circuit method. Wiley, Chichester.

[70] P. B. Johns, "A symmetrical condensed node for the TLM method," IEEE Trans.Microw. Theory Tech., vol.MTT-35, no. 4, pp. 370–377, Apr. 1987.

[71] P. Silvester, "Finite element solution of homogeneous waveguide problems," *Alta Frequenza*, pp. 313–317, 1969.

[72] P. P. Silvester and R. L. Ferrari, *Finite Elements for Electrical Engineers*. Cambridge, U.K.: Cambridge Univ. Press, 1996.

[73] Pinello, W.; Ruehli, A., "Time domain solutions for coupled problems using PEEC models with waveform relaxation," *Antennas and Propagation Society International Symposium, 1996. AP-S. Digest*, vol.3, no., pp.2118,2121 vol.3, 21-26 July 1996.

[74] Pinello,W., Ruehli, A. E. and Cangellaris, A. 'Stabilization of Time Domain Solutions of EFIE based on Partial Element Equivalent Circuit Models'. *IBM Research Report RC 20700*, IBM T. J. Watson Research Division, January 1997.

[75] R. Courant, "Variational methods for a solution of problems of equilibrium and vibrations," *Bull. Amer. Math. Soc.*, pp. 1–23, 1943.

[76] R. du Cloux, W. J. de Graaf, G.P.J.F.M. Maas, R. W. van der Veeken. EMC simulations and measurements. In *Proc. of the IEEE Int. Symp. on Electromagnetic Compatibility*, volume 10, pages 185-190, Zurich, Switzerland. March 1995.

[77] Rosa, E. B. and Grover, F. W. 'Formulas and Tables for the Calculation of Mutual and Self-Induction'. *Bull.Bur. Stand.*, **8**, No. 1, 1911.

[78] R. F. Harrington, *Field Computation by Moment Methods*. NewYork: Macmillan, 1968.

[79] Ruehli, A. E., *An Integral Equation Equivalent Circuit Solution to a large class of interconnect systems.* Ph.D. Dissertation, The University of Vermont. 1972.

[80] Ruehli, A. E., "Inductance Calculations in a Complex Integrated Circuit Environment," *IBM Journal of Research and Development* , vol.16, no.5, pp.470,481, Sept. 1972.

[81] Ruehli, Albert E.; Brennan, Pierce A., "Efficient Capacitance Calculations for Three-Dimensional Multiconductor Systems," *Microwave Theory and Techniques, IEEE Transactions on* , vol.21, no.2, pp.76,82, Feb 1973.

[82] Ruehli, Albert E., "Equivalent Circuit Models for Three-Dimensional Multiconductor Systems," *Microwave Theory and Techniques, IEEE Transactions on* , vol.22, no.3, pp.216,221, Mar 1974.

[83] Ruehli, A.E., N. B. Rabbat , H. Y. Hsieh. Macromodular latent solutions of digital networks including interconnects. In *Proc. of* the IEEE *Int. Symp.* on *Circuits and Systems*, pages 515-512, May 1978.

[84] Ruehli, A.E.; Heeb, H., "Circuit models for three-dimensional geometries including dielectrics," *Microwave Theory and Techniques, IEEE Transactions on* , vol.40, no.7, pp.1507,1516, Jul 1992.

[85] Ruehli, A. E., Garrett, J. E. and Paul, C. R. “Circuit Models for 3D Structures with Incident Fields”, Proceedings of the IEEE International Symposium on EMC, Dallas, Texas, USA, August 1993, pp. 28–32.

[86] Ruehli, A., Paul, C. and Garrett, J. ‘Inductance Calculations using Partial Inductances and Macromodels’. Proceedings of the IEEE International Symposium on EMC, Atlanta, GA, USA, August 1995, pp. 23–28.

[87] Ruehli, A.E.; Miekkala, U.; Heeb, H., "Stability of discretized partial element equivalent EFIE circuit models," *Antennas and Propagation, IEEE Transactions on* ,

vol.43, no.6, pp.553,559, Jun 1995.

[88] Sang-Beom Kim; Joon-Young Soh; Koo-yong Shin; Jin-Hye Jeong; Sung-Ho Myung, "Magnetic Shielding Performance of Thin Metal Sheets Near Power Cables," *Magnetics, IEEE Transactions on* , vol.46, no.2, pp.682,685, Feb. 2010

[89] Singer, H., Br ̈uns, H.-D., Mader, T. et al. CONCEPT Manual of the Program System, TU Hamburg-Harburg, Germany, 2000.

[90] S.V. Kochetov and G. Wollenberg, "Stability of full-wave PEEC models: reason for instabilities and approach for correction", IEEE Tran. on EMC, 47:738-748, 2006.

[91] Smith, W.T.; Das, S.K., "Application of asymptotic waveform evaluation for EMC analysis of electrical interconnects," *Electromagnetic Compatibility, 1995. Symposium Record., 1995 IEEE International Symposium on* , vol., no., pp.429,434, 14-18 Aug 195.

[92] Sue, M.K. "Radio frequency interference at the geostationary orbit". *NASA*. Jet Propulsion Laboratory. Retrieved 6 October 2011.

[93] T. A. Jerse. *A Hybrid Technique for Efficiently Estimating Common-mode Currents* in *Transmission-Line Structures.* Ph.D. Dissertation, The University of Kentucky. 1994.

[94] Tai, C. T. *Dyadic Green's Functions in Electromagnetic Theory*. USA, IEEE Press, Piscataway, NJ, 1997.

[95] Weeks, W. T., Jimenez, A. J., Mahoney, G. W. *et al*. 'Algorithms for ASTAP – a network analysis program'. *IEEE Trans. Circuit Theory*, **20**, 1973, 628–634.

[96] Wollenberg, G. and Kochetov, S. V. 'Modeling the Skin Effect inWire-Like 3D Interconnection Structures with Arbitrary Cross Section by a New Modification of the PEEC Method'. Proceedings of the 15th International Symposium on EMC, Zurich, Switzerland, February 2003, pp. 609–614.

[97] Y. Du, T. C. Cheng and A. S. Farag, "Principles of power-frequency magnetic field shielding with flat sheets in a source of long conductors," IEEE Trans on EMC, Vol. 38,

No. 3, Aug. 1996 , pp. 450-459.

[98] Y. Du and J. Burnett, “Magnetic shielding of double-layer shield at power frequency,” Proc. of IEEE 1997 International Symposium on EMC, Austin, TX, USA, pp. 191-207.

[99] Y. Du and J. Burnett, “ELF shielding performance of metallic enclosure for heavy-current conductors,” IEEE Proc. – Gener. Transm. Distrib. Vol. 146, No. 3, May 1999, pp. 223-228.

[100] Y. Du and W. Dai, “Partial reductance based circuit simulation is efficient and stable,” Proc. of the conf. on Asia south pacific design automation, 2005, pp. 483-488.

[101] Ziolkowski, M.; Gratkowski, S.R., "Genetic Algorithm and Bezier Curves-Based Shape Optimization of Conducting Shields for Low-Frequency Magnetic Fields," *Magnetics, IEEE Transactions on* , vol.44, no.6, pp.1086,1089, June 2008.